

See discussions, stats, and author profiles for this publication at: <https://www.researchgate.net/publication/281348631>

Boundary Layer Dynamic Soaring for Autonomous Aircraft: Design and Validation

Thesis · December 2011

DOI: 10.13140/RG.2.1.5081.0085

CITATIONS

29

READS

773

1 author:



Geoffrey C Bower
A³ by Airbus

13 PUBLICATIONS 222 CITATIONS

[SEE PROFILE](#)

Some of the authors of this publication are also working on these related projects:



Investigating egg attendance behavior in birds [View project](#)

BOUNDARY LAYER DYNAMIC SOARING FOR AUTONOMOUS
AIRCRAFT: DESIGN AND VALIDATION

A DISSERTATION
SUBMITTED TO THE DEPARTMENT OF AERONAUTICS AND
ASTRONAUTICS
AND THE COMMITTEE ON GRADUATE STUDIES
OF STANFORD UNIVERSITY
IN PARTIAL FULFILLMENT OF THE REQUIREMENTS
FOR THE DEGREE OF
DOCTOR OF PHILOSOPHY

Geoffrey Christien Bower
May 2012

Abstract

Dynamic soaring is a flight technique used by albatrosses and other large seabirds to extract energy from wind gradients in the atmospheric boundary layer over the ocean. This technique enables them to fly for extended periods without flapping their wings, in some documented cases circumnavigating the globe. This work examines the application of dynamic soaring to propulsion of small unmanned aerial vehicles (UAVs).

First, the equations of motion were derived and the energy transfer mechanisms were explained for a vehicle flying in a spatially and temporally varying wind field. Next, a robust and efficient dynamic soaring trajectory optimization method that forms the foundation for the remainder of the research was outlined. This method was used to solve for optimal periodic trajectories through a number of different wind fields. It was also used to investigate UAV designs that have the ability to extract electrical energy from their environment and store it on-board, allowing operations during lulls in the wind. Vehicle speed polars were generated that show the maximum cross-country speed achievable as a function of the wind speed and the cross-country flight direction. The method of isochrones was applied to the long-range routing of dynamic soaring vehicles across the ocean by combining vehicle speed polars with satellite based ocean wind measurements.

As part of this work, a small UAV, dubbed *Mariner*, was designed to demonstrate autonomous boundary layer dynamic soaring over water. The objective of the UAV design problem was to minimize the required reference wind speed. Constraints were imposed on vehicle size and weight, and careful attention was paid to stability and control requirements imposed by the optimal trajectories. Sensors and sub-systems

were specified to allow for accurate state estimation in close proximity to the water surface.

Experimentally, a small off-the-shelf airframe was flown to aid development of *Mariner*'s flight control hardware and software. An extended Kalman filter (EKF) was implemented for vehicle state and wind estimation and tuned through flight testing. In addition, a novel GPS tracking tag was designed and tested to improve our understanding of albatross dynamic soaring.

Acknowledgements

Successfully navigating a Ph.D. was a multi-year process that involved the support of many people and organizations.

First, I want to thank my thesis advisor, Prof. Ilan Kroo, for both the freedom to explore research topics that interested me throughout my tenure at Stanford and for providing guidance whenever my research required it. I also need to thank Prof. Juan Alonso, one of my reading committee members who was always able to provide a big picture perspective. I'd also like to thank my final reading committee member, Prof. Margot Gerritsen, who was able to provide an outside perspective on my research and to draw important parallels to work in other disciplines.

I'm also grateful for my thesis defense committee members. First, Prof. Scott Shaffer from San Jose State University for collaborating to design and deploy the albatross trackers, as well as providing a biologist's perspective on dynamic soaring. Prof. Michael Saunders was always generous with his time and I thank him for agreeing to chair my defense committee and for providing the SNOPT optimization software used throughout this research. Although he was unable to attend my defense, I also need to acknowledge Dr. Peter Lissaman for many discussions relating to fluid dynamics in general and dynamic soaring in particular.

My tenure at Stanford also would not have been possible without the support of the Aero/Astro department staff (especially Jay, Lynn, Robin, Ralph, Liza and Corinna) and the various sources of funding I've been fortunate enough to receive. These sources include the National Science Foundation Graduate Research Fellowship Program, the Stanford Aero/Astro Department, the NASA Subsonic fixed wing program, the Stanford UAV Center, and the Boeing Company. I'm also grateful I

had the opportunity to be a course assistant for both Prof. Alonso and Prof. Kroo, helping with the autonomous aircraft design class.

Working in the Aircraft Design Group hardly ever felt like work thanks to all the great people in the lab. I owe a debt of gratitude to all the past and present members who have helped me along the way including: Chinmay Patel, Hak Tae Lee, Dev Rajnarayan, Axel Strang, Emily Dallara, Andrew Ning, Jia Xu, Tristan Flanzer, Alex Haas, Mathias Wintzer, Sara Smoot, Alex Stoll, Zouhair Mahboubi, and Robbie Bunge.

I was also fortunate to have many close friends at Stanford who were always able to keep things in perspective and provide a proper work-life balance. In particular I want to thank Alex Naiman, Alex Forman, Samson Phan, Ken Yuan, Fraser Cameron, Marianne Karplus, Noel Bakhtian, Joel Weitzmann, Melody Wu, Nicolas Lee, Mara Jennings, Kin Fucharoen, and Ariana Peck. I also want to thank the rest of the ultimate frisbee crew and all of my Stanford Cycling teammates.

Finally, I need to thank my parents, Mary Lynn and Kenneth, for their unconditional love and support.

Contents

Abstract	iv
Acknowledgements	vi
1 Introduction	1
1.1 Motivation	1
1.2 Vision	5
1.3 Thesis Outline	5
1.4 Thesis Contributions	6
2 EOM and Trajectory Optimization	8
2.1 Equations of Motion	8
2.1.1 Sachs' EOM	11
2.1.2 Zhao's EOM	12
2.1.3 Discussion	13
2.1.4 Electrical Energy EOM	13
2.1.5 Solar Power Model	16
2.1.6 Wind Models	18
2.2 EOM Energy Analysis	25
2.2.1 Step Wind Profile Analysis	28
2.2.2 Wind Gradient for Constant Airspeed and Flight Path Angle Climb	32
2.3 Trajectory Optimization	37
2.3.1 Problem Formulation	37

2.3.2	Solution Methodologies	39
2.3.3	Validation	43
3	Trajectory Optimization Results	52
3.1	Linear Boundary Layer	53
3.2	Log Boundary Layer - Minimum Reference Wind Speed	59
3.3	Log Boundary Layer - Maximum Net Speed	61
3.4	Ocean Boundary Layer with Waves	63
3.4.1	Start and End on the Same Wave	65
3.4.2	Transfer One Wave Upstream	70
3.5	Electrical Energy System	75
3.5.1	Minimum Wind Speed Case	76
3.5.2	Maximum Net Speed	81
3.5.3	Battery Charging/Discharging	86
4	Trajectory Planning and Control	88
4.1	Low- and Mid-Level Trajectory Planning and Control	89
4.2	High-Level Trajectory Planning and Control	90
4.2.1	Problem Formulation	91
4.2.2	Receding Horizon Control with the Method of Isochrones . . .	94
4.2.3	Example Results	97
5	Aircraft Design for Dynamic Soaring	103
5.1	Basic Trade Studies	104
5.2	Aircraft Systems	107
5.3	Sizing	111
5.3.1	Problem Formulation	111
5.3.2	Analysis Methods	113
5.3.3	Sizing Results	115
5.4	Tail and Control Surface Sizing	119
5.5	Final Design	121

6 Experimental Validation	130
6.1 Albatross Tracker	131
6.1.1 Design	132
6.1.2 Calibration	137
6.1.3 Deployment	143
6.2 EKF	145
6.2.1 Process Model	146
6.2.2 Measurement Model	149
6.3 Flight Test Results	152
6.3.1 EKF Validation	153
7 Conclusions and Future Work	158
7.1 Summary of Findings	158
7.2 Suggestions for Future Work	161
A Trajectory Optimization Validation Results	163
Bibliography	165

List of Tables

2.1	Electrical power system component efficiencies	15
2.2	Step boundary layer analytic results	31
2.3	Model Wandering Albatross parameters	33
2.4	Trajectory optimization constraints	39
2.5	Comparison of solution methodologies	45
2.6	Convergence tolerance study	46
2.7	Number of collocation points study	47
3.1	Solar airplane parameters	76
4.1	Long range UAV parameters	98
4.2	Planning horizon trade study results	100
5.1	Trade study baseline design	104
5.2	Electronic components for <i>Mariner</i>	110
5.3	Sizing design variable bounds	112
5.4	Refined design variable bounds	117
5.5	Grid search bounds	117
5.6	Final control surface sizes	121
5.7	Final mass breakdown	126
6.1	Albatross tracker state machine parameters	135
A.1	Trajectory optimization validation: state and control values	164

List of Figures

1.1	Illustration of dynamic soaring trajectory	3
1.2	Shear layer formation over a ridge	4
2.1	NED coordinate frame	9
2.2	Block diagram of electrical power system	14
2.3	Solar panel orientation	18
2.4	Log boundary layer profile	20
2.5	Boundary layer over wave surface	25
2.6	Step wind profile	28
2.7	Required wind gradient for model Wandering Albatross	34
2.8	Optimum climb angle and lift coefficient	35
2.9	Minimum wind gradient for model Wandering Albatross	35
2.10	Required wind gradient sensitivity plot	36
2.11	Differential flatness thrust constraint	46
2.12	Minimum wind speed trajectory for log boundary layer	48
2.13	Speed, flight path angle and heading angle for minimum wind speed trajectory	49
2.14	C_L and ϕ for minimum wind speed trajectory	49
2.15	Load factor for minimum wind speed trajectory	50
2.16	Energies for minimum wind speed trajectory	50
2.17	Power for minimum wind speed trajectory	51
3.1	Minimum wind speed trajectory for linear boundary layer	53

3.2	Speeds, flight path angle and heading angle for minimum wind gradient trajectory	54
3.3	C_L and ϕ for minimum wind gradient trajectory	54
3.4	Load factor for minimum wind gradient trajectory	55
3.5	Energies for minimum wind gradient trajectory	55
3.6	Power for minimum wind gradient trajectory	56
3.7	Minimum required wind gradient polar for linear boundary layer	57
3.8	Downwind trajectory with minimum required wind gradient	58
3.9	Cycle times for the minimum required wind gradient polar	58
3.10	Minimum required wind speed polar for log boundary layer	59
3.11	Selected optimal minimum required wind speed trajectories	60
3.12	Cycle times for the minimum required wind speed polar	60
3.13	Speed polar for the model Wandering Albatross	61
3.14	Cycle times for the speed polar	62
3.15	Selected maximum speed trajectories	63
3.16	Minimum u^* trajectory with $n = 0$	66
3.17	Speed, flight path angle and heading angle for minimum u^* trajectory with $n = 0$	67
3.18	C_L and ϕ for minimum u^* trajectory with $n = 0$	67
3.19	Load factor for minimum u^* trajectory with $n = 0$	68
3.20	Energies for minimum u^* trajectory with $n = 0$	68
3.21	Power for minimum u^* trajectory with $n = 0$	69
3.22	Wave phase and height for minimum u^* trajectory with $n = 0$	69
3.23	North and Down winds for minimum u^* trajectory with $n = 0$	70
3.24	Minimum u^* trajectory with $n = -1$	71
3.25	Speed, flight path angle and heading angle for minimum u^* trajectory with $n = -1$	72
3.26	C_L and ϕ for minimum u^* trajectory with $n = -1$	72
3.27	Load factor for minimum u^* trajectory with $n = -1$	73
3.28	Energies for minimum u^* trajectory with $n = -1$	73
3.29	Power for minimum u^* trajectory with $n = -1$	74

3.30	Wave phase and height for minimum u^* trajectory with $n = -1$	74
3.31	North and Down winds for minimum u^* trajectory with $n = -1$	75
3.32	Minimum wind speed solar augmented trajectory	77
3.33	Speed and flight path angle for the solar augmented trajectory	78
3.34	Controls for the solar augmented trajectory	78
3.35	Energy trajectory for the solar augmented trajectory	79
3.36	Power for the solar augmented trajectory	79
3.37	Sun angles and irradiance for the solar augmented trajectory	80
3.38	Minimum wind speed for all sun locations	80
3.39	Maximum speed solar augmented trajectory	82
3.40	Speed and flight path angle for the maximum speed solar augmented trajectory	83
3.41	Controls for the maximum speed solar augmented trajectory	83
3.42	Energy trajectory for the maximum speed solar augmented trajectory	84
3.43	Power for the maximum speed solar augmented trajectory	84
3.44	Sun angles and irradiance for the maximum speed solar augmented trajectory	85
3.45	Maximum speed for all sun locations	85
3.46	Maximum speed vs. battery charge/discharge rate	87
4.1	Method of isochones illustration	93
4.2	Illustration of the method to identify isochrone points	95
4.3	Isochrone island example	95
4.4	Long range UAV speed polar	99
4.5	Minimum time trajectory with perfect wind knowledge	99
4.6	Comparison of minimum time routes for different planning horizons .	100
4.7	Illustration of 24 hr planning horizon example	101
5.1	Baseline design sensitivity analysis	106
5.2	Wing airfoil drag polars	114
5.3	Tail airfoil drag polars	115
5.4	Stall speed vs. required reference wind speed	116

5.5	Objective vs. S and \mathcal{R} for the first iteration	118
5.6	Objective vs. S and \mathcal{R} for the second iteration	118
5.7	Root locus of longitudinal modes	120
5.8	Root locus of lateral modes	121
5.9	Required stability axis rates	122
5.10	Required control surface deflections	123
5.11	Elevator deflections for trim	123
5.12	Rendering of <i>Mariner</i>	125
5.13	<i>Mariner</i> Drag Polar	125
5.14	<i>Mariner</i> Velocity Hodograph	127
5.15	<i>Mariner</i> minimum reference wind speed trajectory	127
5.16	<i>Mariner</i> controls for the minimum reference wind speed trajectory . .	128
5.17	Energies for the minimum reference wind speed trajectory	129
5.18	Power for the minimum reference wind speed trajectory	129
6.1	Tracker state diagram	135
6.2	Illustration of GETGPS state logic	136
6.3	Tracker CAD model	138
6.4	Tracker PCB schematic	138
6.5	Tracker PCB board layout	139
6.6	Picture of assembled tracker	139
6.7	Picture of open tracker	140
6.8	Magnetometer measurement ellipsoid	142
6.9	Calibrated magnetometer measurements	142
6.10	Magnetometer error histogram	143
6.11	Hardware/software development UAV	153
6.12	Horizon detection algorithm example	156
6.13	Verification of filtered bank and pitch angle estimates	157

Chapter 1

Introduction

1.1 Motivation

The effectiveness of small unmanned aerial vehicles (SUAVs) is severely limited by the energy requirements of their propulsion and payload systems. Here a SUAV is defined to be one that is launched by hand, typically having a mass of less than 5 *kg*. Battery powered SUAVs have limited ranges and maximum endurances around two hours. Hydrocarbon or fuel cell powered vehicles have been demonstrated to have endurances on the order of 10 hours and correspondingly longer ranges. For many potential civilian and military SUAV missions, the onboard sensor power requirements reduce the range and endurance, diminishing their utility to operators. As a consequence SUAVs are primarily limited to short range “over the next hill” military observation missions.

In many of the environments that small UAVs fly in, there is energy available in the atmosphere that can be used to increase range and endurance. Extracting energy from the atmosphere is generally referred to as soaring. If an aircraft obtains kinetic or potential energy from soaring flight, then the consumable energy carried on board in the form of batteries or fuel will last considerably longer, thereby extending the range or endurance. Soaring flight is typically categorized by the type of atmospheric energy available and how it is extracted.

The most common and well known category is thermal soaring. Thermals are

pockets of warm air that rises through the atmosphere. They are typically formed due to uneven heating of the Earth's surface by solar radiation throughout the day. Birds and human glider pilots make extensive use the energy available in the vertically rising air that offsets the sink rate of the aircraft relative to the air. Raptors extensively use thermal soaring over land [1]. Pelicans, sea gulls, and frigatebirds are known to utilize thermal soaring near the shore or over water [2]. Human pilots of both full size gliders and remote control gliders also make extensive use of thermals for sport. The spatial extent of thermals are relatively small and require circling flight to stay within them. There have been a number of recent studies that have looked at autonomous thermal soaring to increase UAV endurance and range [3, 4, 5, 6, 7, 8].

Another type of soaring that takes advantage of vertically rising air is slope soaring. As the wind blows up a slope there is a vertical component of the wind that offsets the sink rate of the bird or aircraft. Many bird species are observed slope soaring in proximity to ridges and cliffs [9]. Slope soaring is also popular among RC pilots. In regions where the local terrain is suitable over long distances, slope soaring is used by full sized gliders, for example, along the ridges in central Pennsylvania [10]. Collectively, thermal soaring and slope soaring are often referred to as static soaring, as a majority of energy is obtained through a steady vertical component of the wind.

Gust soaring extracts energy from high frequency turbulence in the atmosphere [11]. It is believed that birds make use of gust soaring when flying in turbulent conditions as they often outperform RC models that otherwise have similar performance. Energy is extracted from gusts by increasing lift in regions of updrafts and decreasing it in regions of downdrafts, while maintaining average lift equal to the vehicle weight. Unless high levels of turbulence are present it is difficult to extract enough power from gusts to maintain constant total energy without propulsion, however, the propulsive energy requirements can be reduced.

The final soaring technique is the topic covered in this thesis and is referred to as dynamic soaring. Dynamic soaring involves extracting energy by flying periodic maneuvers through wind gradients. In the lower atmospheric boundary layer over the ocean, the wind speed near the surface approaches zero due to the no slip condition. The wind speed quickly increases with altitude, establishing a significant wind

gradient. This wind gradient is used by many seabird species to fly throughout the world's oceans. The most well known type of seabird that uses dynamic soaring is the Wandering Albatross, which is able to travel throughout the Southern Ocean with minimal propulsive energy expenditure. There are documented cases of Gray-headed Albatrosses circumnavigating the globe in the Southern Ocean in as little as 46 days [12].

An illustration of a typical dynamic soaring trajectory is shown in Fig. 1.1. Energy is extracted from the atmosphere when a component of the aerodynamic force on the vehicle is aligned with the local wind vector. Along the section of the trajectory marked '1', the lift vector has a component along the wind speed vector, which is also of large magnitude, indicating significant energy is gained. Along section '2', the lift vector is pointing nearly opposite the wind vector, indicating a loss of total energy due to the winds, however, it is a smaller amount than that gained at altitude since the wind speed is much lower in this region. If the integrated energy gained from the wind along the trajectory offsets the energy lost due to drag, then a neutral energy cycle is feasible and the bird or aircraft can continuously fly without expending energy for propulsion.

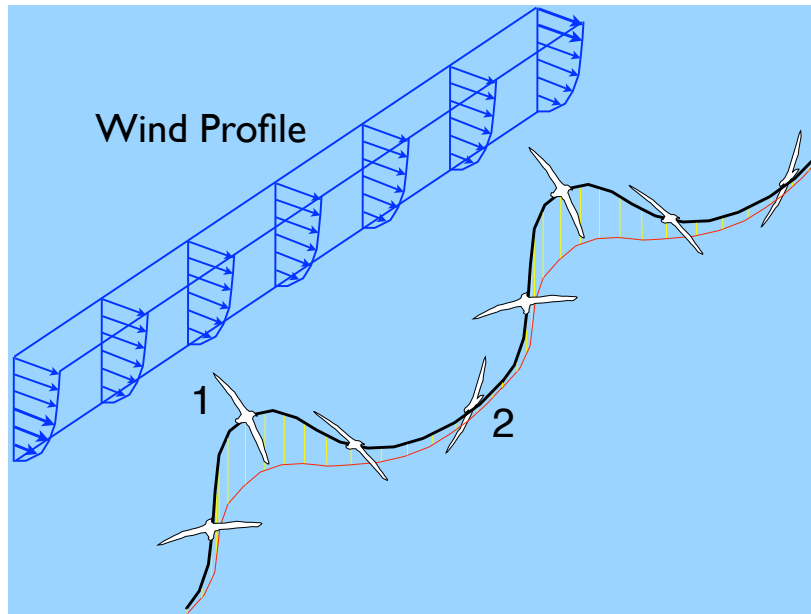


Figure 1.1: An illustration of a dynamic soaring trajectory.

A common aspect of almost all dynamic soaring trajectories is that it is not always possible to extract energy from the winds at all points along the trajectory, instead a loss of energy at one point must be accepted to enable a greater gain in energy at a later point. This aspect of trading energy now for the potential of extracting more energy later is an important consideration in the formulation of dynamic soaring control algorithms.

It should also be noted that dynamic soaring is used by remote control model airplane pilots who fly through the shear layers that are formed when a strong winds blow up a slope and separate over a sharp ridge at the top as shown in Fig. 1.2. By flying orbits between the quiescent air below the shear layer and the fast moving air above, the aircraft are able to extract significant energy from the winds [14]. In fact, dynamic soaring gliders are the fastest model airplanes, with the world record as of February 2011 standing at 468 mph! While impressive, such flights are for recreation, and not of much use in performing useful scientific or surveillance missions.

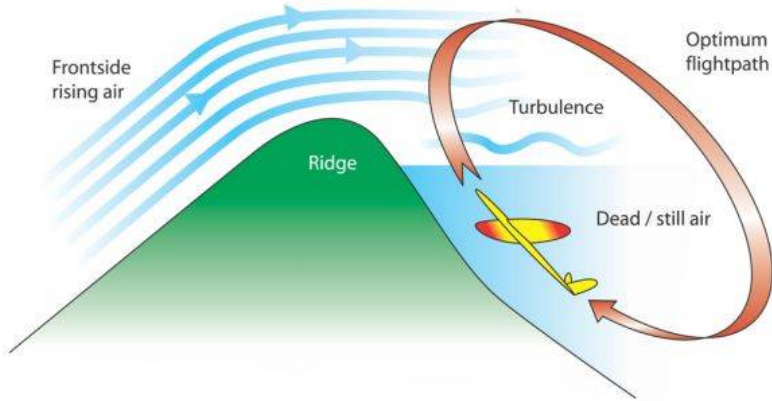


Figure 1.2: An illustration of the shear layer formed over the edge of a sharp ridge and exploited by remote control pilots (Ref. [15] - <http://www.tmfcc.org.uk/ds/darkside.html>).

1.2 Vision

With recent advances in lightweight Microelectromechanical (MEMS) sensors, low-power system-on-chip computers, and low-power global satellite communications systems, the design of an extremely long endurance SUAV that uses dynamic soaring for propulsion is within the realm of possibility. Electrical energy for onboard sensors and control systems could be obtained solely from the environment via solar panels or a wind powered generator. Such a vehicle should be capable of nearly continuous operation over the world's oceans while performing any number of interesting tasks.

There are a few missions that a dynamic soaring UAV would be well suited to performing. The first would be as a science platform to collect data on the interactions between the ocean and lower atmosphere, which is of interest to climate scientists as significant momentum and energy are transferred across this interface [16, 17]. A dynamic soaring UAV would also provide a reasonable observation platform to monitor shipping lanes and to police fisheries across the world's oceans. Militarily, it could also provide a platform to track ships or to distribute a dynamic sensor array such as microphones for submarine detection [18].

An interesting demonstration of the integration of the various technologies would be to design a SUAV to autonomously circumnavigate the Earth. Before such an ambitious project is undertaken it is necessary to demonstrate autonomous boundary layer dynamic soaring over shorter distances. The primary focuses of this thesis will be on understanding the basics of dynamic soaring and designing a demonstration vehicle for autonomous boundary layer dynamic soaring.

1.3 Thesis Outline

The equations of motion for a point mass aircraft model flying in a spatially and temporally varying wind field are derived in Chapter 2. An energy analysis is performed on the equations to identify the mechanism for energy transfer from the winds to the flight vehicle. An additional equation of motion is derived to represent changes in the energy state of an onboard battery. Next, analytic trajectory optimization results are

derived for two simple wind fields. The general dynamic soaring trajectory optimization problem is formulated and used to solve a number of interesting problems, with results presented in Chapter 3.

A proposed three-level control strategy is outlined in Chapter 4. A brief overview of the low- and mid-level controllers under development by a colleague is presented [19]. The remainder of the chapter describes a high-level control law developed as part of this work for guiding a dynamic soaring UAV over the oceans using wind predictions provided by NOAA and the aircraft's dynamic soaring performance polar.

The design of a dynamic soaring UAV is described in Chapter 5. First, a number of trade studies are conducted about a baseline design to gain insight into the most important design parameters. Sensors and control electronics are specified and a SUAV is designed around them to minimize the reference wind speed required to dynamic soar in an ocean boundary layer. Careful attention is paid to the stability and control requirements imposed by flying dynamic soaring maneuvers.

Chapter 6 details experimental work carried out to extend our understanding of dynamic soaring and to take steps towards demonstrating autonomous dynamic soaring with a SUAV. The development of a novel albatross tracking tag is described in detail. The tracking tag includes GPS, MEMS inertial sensors, and pressure sensors to estimate the birds position, velocity, and orientation at a much higher rate than has previously been done. Flight test results are also presented in this chapter documenting the development of an extended Kalman filter for aircraft state estimation. Finally, Chapter 7 draws conclusions about the work and presents directions for further research.

1.4 Thesis Contributions

The primary contributions of this thesis include:

- Identification of important design parameters for a dynamic soaring aircraft
- Design of a small UAV specifically for boundary layer dynamic soaring

- Design of a tracking tag to take high resolution position, velocity, and orientation data on an albatross while it is dynamic soaring
- A thorough comparison of dynamic soaring trajectory optimization methods
- Development of a simple wind-wave boundary layer model
- Derivation of optimal trajectories through the wind-wave boundary layer and using them to explain observations of albatross dynamic soaring trajectories
- Development of a high-level controller to efficiently guide a dynamic soaring UAV across an ocean
- Addition of the onboard battery energy equation of motion to the dynamic soaring trajectory optimization problem

Chapter 2

EOM and Trajectory Optimization

Robust and efficient solutions to the dynamic soaring trajectory optimization problems are central to the design and control methodologies results presented in chapters 4 and 5. This chapter begins by deriving the point mass equations of motion for a vehicle flying in spatially and temporally varying winds. Next, methods for determining optimal cyclic dynamic soaring trajectories are discussed. Key trajectory optimization results are presented for a number of different boundary layer shapes in the next chapter.

2.1 Equations of Motion

In this section, the equations of motion (EOM) for a point mass model of an aircraft flying in a spatially and temporally varying wind field are derived. We begin by defining an inertial North, East, Down (NED) reference frame where the x , y , and z positions correspond to the North, East, and Down coordinates, respectively. The inertial wind speed (\vec{W}) components in the North, East, and Down directions are given by $W_x(x, y, z, t)$, $W_y(x, y, z, t)$, and $W_z(x, y, z, t)$, respectively. The dependence on t indicates the wind field may also be changing with time.

The orientation of the aerodynamic forces on the aircraft are defined by a set of three successive angular rotations. First, the air relative heading angle, ψ , is defined to be zero to the North and increases to the East (a clockwise rotation when viewed

from above). Next, the air relative flight path angle, γ , is defined positive nose up. The final rotation is the bank angle, ϕ , which is defined positive when rolling clockwise when viewed from behind the aircraft. Four aerodynamic forces are accounted for in this model: lift (L), drag (D), thrust (T) and generator drag (D_{gen}). The generator drag and thrust are not always present and will be used as control variables in some of the later analyses. The orientation of these forces and angles in the coordinate frame are depicted in Fig. 2.1.

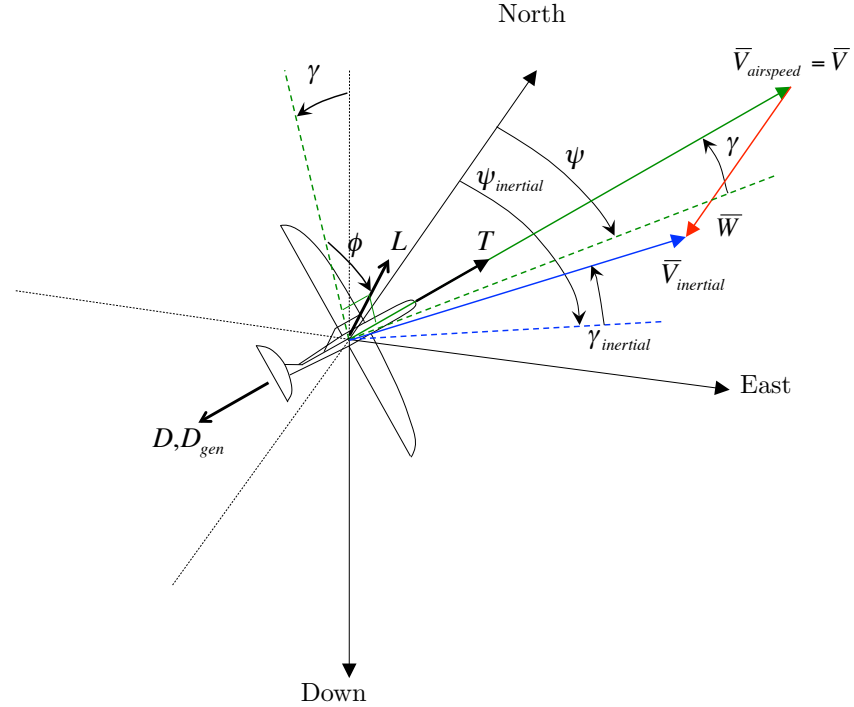


Figure 2.1: Diagram depicting the coordinate frame, important angles (ψ , γ , ϕ , $\psi_{inertial}$, and $\gamma_{inertial}$) and vectors (\vec{L} , \vec{T} , \vec{D} , \vec{D}_{gen} , \vec{V} , \vec{W} , and $\vec{V}_{inertial}$). The dashed lines are vector projections into the North-East plane.

The air relative heading and flight path angles specify the direction of the airspeed vector (\vec{V}) in inertial space. The bank angle then determines the orientation of the lift vector. The lift and drag forces are given by Eqs. 2.1 and 2.2, which depend on the magnitude of the airspeed (V), air density (ρ), wing reference area (S), and lift coefficient (C_L). In this work, the drag polar is defined by a fourth order polynomial

with coefficients C_{D_0} , C_{D_1} , C_{D_2} , C_{D_3} , and C_{D_4} :

$$L = \frac{1}{2}\rho V^2 S C_L, \quad (2.1)$$

$$D = \frac{1}{2}\rho V^2 S (C_{D_0} + C_{D_1} C_L + C_{D_2} C_L^2 + C_{D_3} C_L^3 + C_{D_4} C_L^4). \quad (2.2)$$

Two equivalent sets of EOM are derived that are used in the trajectory optimization problems described in Section 2.3 [13, 20]. In the first set of equations, the state variables are x , y , z , $u (= \dot{x})$, $v (= \dot{y})$, and $w (= \dot{z})$. In the second, the state variables are x , y , z , V , γ , and ψ . In both formulations the control variables are C_L , ϕ , T , and D_{gen} . A number of derived quantities, namely the inertial speed, ground speed, inertial heading angle and inertial flight path angle may also be of interest and are given in terms of the state variables in Eqs. 2.3.

$$V_{inertial} = \sqrt{u^2 + v^2 + w^2} \quad (2.3a)$$

$$V_{ground} = \sqrt{u^2 + v^2} \quad (2.3b)$$

$$\gamma_{inertial} = \arctan\left(\frac{-w}{V_{ground}}\right) \quad (2.3c)$$

$$\psi_{inertial} = \arctan\left(\frac{v}{u}\right) \quad (2.3d)$$

Applying Newton's 2nd law in the North, East, and Down directions results in Eqs. 2.4.

$$m\ddot{x} = m\dot{u} = (T - D - D_{gen}) \cos \gamma \cos \psi + L (-\sin \gamma \cos \psi \cos \phi - \sin \psi \sin \phi) \quad (2.4a)$$

$$m\ddot{y} = m\dot{v} = (T - D - D_{gen}) \cos \gamma \sin \psi + L (-\sin \gamma \sin \psi \cos \phi + \cos \psi \sin \phi) \quad (2.4b)$$

$$m\ddot{z} = m\dot{w} = -(T - D - D_{gen}) \sin \gamma + L (-\cos \gamma \cos \phi) + mg \quad (2.4c)$$

The kinematic equations are given by Eqs. 2.5. Note that W_x , W_y and W_z are functions of position and time, however, for clarity this dependence will be dropped from the notation in the remainder of this chapter.

$$\dot{x} = u = V \cos \gamma \cos \psi + W_x(x, y, z, t) \quad (2.5a)$$

$$\dot{y} = v = V \cos \gamma \sin \psi + W_y(x, y, z, t) \quad (2.5b)$$

$$\dot{z} = w = -V \sin \gamma + W_z(x, y, z, t) \quad (2.5c)$$

2.1.1 Sachs' EOM

To obtain the equations of motion derived by Sachs in Ref. [13], the air relative flight path angle and heading angle in Eqs. 2.4 are replaced with Eqs. 2.6 to obtain the final set of equations presented in Eqs. 2.7.

$$\gamma = \arctan \left(\frac{-w + W_z}{\sqrt{(u - W_x)^2 + (v - W_y)^2}} \right) \quad (2.6a)$$

$$\psi = \arctan \left(\frac{v - W_y}{u - W_x} \right) \quad (2.6b)$$

$$m\dot{u} = (T - D - D_{gen}) \frac{(u - W_x)}{V} + L \left(\frac{(w - W_z)(u - W_x)}{VV_h} \cos \phi - \frac{(v - W_y)}{V_h} \sin \phi \right) \quad (2.7a)$$

$$m\dot{v} = (T - D - D_{gen}) \frac{(v - W_y)}{V} + L \left(\frac{(w - W_z)(v - W_y)}{VV_h} \cos \phi + \frac{(u - W_x)}{V_h} \sin \phi \right) \quad (2.7b)$$

$$m\dot{w} = (T - D - D_{gen}) \frac{(w - W_z)}{V} - L \frac{V_h}{V} \cos \phi + mg \quad (2.7c)$$

$$\dot{x} = u \quad (2.7d)$$

$$\dot{y} = v \quad (2.7e)$$

$$\dot{z} = w \quad (2.7f)$$

$$(2.7g)$$

$$(2.7h)$$

In terms of the state variables, the airspeed may be calculated as $V = \sqrt{(u - W_x)^2 + (v - W_y)^2 + (w - W_z)^2}$. The horizontal component of the airspeed also appears in the equations and may be calculated as $V_h = \sqrt{(u - W_x)^2 + (v - W_y)^2}$.

2.1.2 Zhao's EOM

An equivalent set of EOM is derived by Jackson, et al. in Ref. [20] and are used by Zhao in Ref. [21] for analysis of dynamic soaring trajectories. First, the kinematic equations (Eqs. 2.5) are differentiated with respect to time to obtain Eqs. 2.8.

$$\ddot{x} = \dot{V} \cos \gamma \cos \psi - \dot{\gamma} V \sin \gamma \cos \psi - \dot{\psi} V \cos \gamma \sin \psi + \dot{W}_x \quad (2.8a)$$

$$\ddot{y} = \dot{V} \cos \gamma \sin \psi - \dot{\gamma} V \sin \gamma \sin \psi + \dot{\psi} V \cos \gamma \cos \psi + \dot{W}_y \quad (2.8b)$$

$$\ddot{z} = -\dot{V} \sin \gamma - \dot{\gamma} V \cos \gamma + \dot{W}_z \quad (2.8c)$$

The final EOM (Eqs. 2.9) are generated by plugging Eqs. 2.8 into Eqs. 2.4 and solving the resulting set of equations for \dot{V} , $\dot{\gamma}$, and $\dot{\psi}$.

$$\dot{x} = V \cos \gamma \cos \psi + W_x \quad (2.9a)$$

$$\dot{y} = V \cos \gamma \sin \psi + W_y \quad (2.9b)$$

$$\dot{z} = -V \sin \gamma + W_z \quad (2.9c)$$

$$\dot{V} = \frac{T - D - D_{gen} - mg \sin \gamma - m\dot{W}_x \cos \gamma \cos \psi - m\dot{W}_y \cos \gamma \sin \psi + m\dot{W}_z \sin \gamma}{m} \quad (2.9d)$$

$$\dot{\gamma} = \frac{L \cos \phi - mg \cos \gamma + m\dot{W}_x \sin \gamma \cos \psi + m\dot{W}_y \sin \gamma \sin \psi + m\dot{W}_z \cos \gamma}{mV} \quad (2.9e)$$

$$\dot{\psi} = \frac{L \sin \phi + m\dot{W}_x \sin \psi - m\dot{W}_y \cos \psi}{mV \cos \gamma} \quad (2.9f)$$

These equations contain terms that depend on the wind speed rates seen by the vehicle. These rates can be calculated in terms of the spatial and temporal derivatives of the wind field along with the inertial velocity of the vehicle using Eqs. 2.10.

$$\dot{W}_x = \frac{\partial W_x}{\partial t} + \frac{\partial W_x}{\partial x}\dot{x} + \frac{\partial W_x}{\partial y}\dot{y} + \frac{\partial W_x}{\partial z}\dot{z} \quad (2.10a)$$

$$\dot{W}_y = \frac{\partial W_y}{\partial t} + \frac{\partial W_y}{\partial x}\dot{x} + \frac{\partial W_y}{\partial y}\dot{y} + \frac{\partial W_y}{\partial z}\dot{z} \quad (2.10b)$$

$$\dot{W}_z = \frac{\partial W_z}{\partial t} + \frac{\partial W_z}{\partial x}\dot{x} + \frac{\partial W_z}{\partial y}\dot{y} + \frac{\partial W_z}{\partial z}\dot{z} \quad (2.10c)$$

2.1.3 Discussion

The two sets of EOM just derived each have advantages and disadvantages when used for trajectory optimization. The advantages of Sachs' EOM (Eqs. 2.7) are that they contain fewer trigonometric terms and that they only require evaluating the wind velocities, and not the wind rates. The primary disadvantage appears when setting initial conditions for a trajectory optimization problem, where setting inertial speeds may be non-intuitive when the vehicle's airspeed is the same order of magnitude as the wind speed at certain points in the trajectory. In contrast, Zhao's EOM appear more complicated and involve evaluating the wind rates in addition to the wind speeds. Their advantage lies in the intuitiveness of using airspeed, flight path angle, and heading angle as state variables. Zhao's EOM will be used throughout the remainder of this thesis. It should be emphasized that the two sets of equations are equivalent and a trajectory that satisfies one set will satisfy the other.

It should also be noted that non-dimensional forms of these equations have been derived by previous researchers [22, 21]. Some additional insights might be gained by doing so, however, the primary insight will be evident from the simple step boundary layer analysis shown in Section 2.2.1.

2.1.4 Electrical Energy EOM

For a realistic UAV the management of onboard electrical energy to power sensors, communications, and actuators becomes critical to achieving long duration flight. An equation of motion for the state of the onboard electrical energy is derived here, which may also be used in trajectory optimization studies. The electrical system is assumed

to consist of at least a subset of the following components:

- Battery
- Electric motor
- Electric generator (could be the same as the motor)
- Solar panel
- Electrical load (sensors, communications, actuators)
- Power electronics (maximum power point tracker, charger, motor speed control)

A diagram of the electrical power system is shown in Fig. 2.2. For the trajectory optimization results presented later each component is assumed to have a fixed efficiency. Reasonable values of the component and sub-system efficiencies are summarized in Table 2.1. The exact values used in each specific trajectory optimization will be indicated in the appropriate results section.

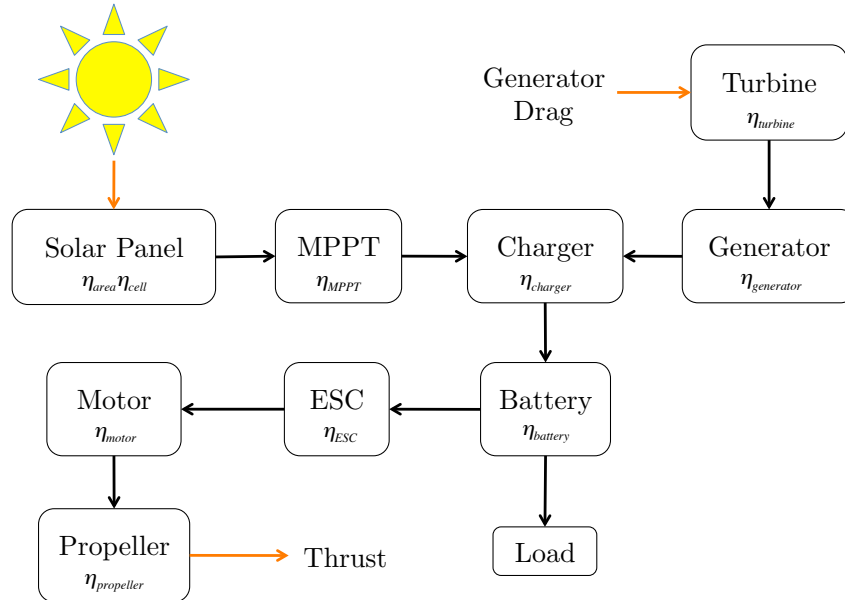


Figure 2.2: Block diagram of electrical power system.

Table 2.1: Ranges of electric power system component efficiencies. Sub-system efficiencies given as product of component efficiencies at the bottom of the table.

Component	Symbol	Value	Comment
Solar panel area	η_{area}	0.5 – 0.95	Solar panel area / S
Solar cell	η_{cell}	0.04 – 0.25	
MPPT	η_{MPPT}	0.9 – 0.99	Maximum power point tracker
Charger	$\eta_{charger}$	0.9 – 0.98	
Turbine	$\eta_{turbine}$	0.5 – 0.9	
Generator	$\eta_{generator}$	0.6 – 0.9	
Propeller	$\eta_{propeller}$	0.5 – 0.9	
Motor	η_{motor}	0.6 – 0.9	
ESC	η_{ESC}	0.95 – 0.99	
Battery discharge	$\eta_{battery}$	0.99 – 0.998	Lithium polymer
Solar Power System	η_{sun}	0.02 – 0.23	$\eta_{area} \cdot \eta_{cell} \cdot \eta_{MPPT} \cdot \eta_{charger}$
Generator System	η_{gen}	0.26 – 0.79	$\eta_{turbine} \cdot \eta_{generator} \cdot \eta_{ESC} \cdot \eta_{charger}$
Propulsion System	η_{prop}	0.28 – 0.8	$\eta_{propeller} \cdot \eta_{motor} \cdot \eta_{ESC} \cdot \eta_{battery}$

The equation of motion for the energy stored in the battery is given by Eq. 2.11.

$$\dot{E} = \eta_{sun} \left(G_{beam} f(\theta) + G_{diff} \frac{1 + \cos \beta}{2} + G_{gnd} \frac{1 - \cos \beta}{2} \right) + \eta_{gen} D_{gen} V - \frac{TV}{\eta_{prop}} - P_{load} \quad (2.11)$$

The first term corresponds to the power available from the solar panel, a model of which is described in the next section. The efficiency, η_{sun} includes the area efficiency of the solar panel (solar panel area divided by reference wing area), the solar cell efficiency, the maximum power point tracker efficiency and the battery charging circuit efficiency. The second term represents the power available from the generator where the efficiency, η_{gen} , represents the proportion of the power lost due to the generator drag that is converted into chemical energy in the battery. It includes the turbine efficiency, the generator efficiency, and battery charging circuit efficiency. The next term represents the power out of the battery that goes to the propulsion system. The efficiency, η_{prop} includes the propeller efficiency, motor efficiency, electronic speed control efficiency, and the battery discharge efficiency. The final term represents the electrical load from sensors, actuators, payloads, and communications.

2.1.5 Solar Power Model

Next, a simple model of the energy available to the solar panels as a function of sun position, local conditions and aircraft orientation is presented [23]. The energy incident on a panel is assumed to come from three primary sources: direct beam irradiance, diffuse isotropic irradiance from scattering in the atmosphere, and diffuse isotropic irradiance reflected from the ground. For a given extraterrestrial solar irradiance (G_{sun}), sun elevation angle (γ_{sun}), clearness index (k_t), and ground reflectance (ρ_g), the three irradiance components (G_{beam} , G_{diff} , and G_{gnd}) can be determined using Eqs. 2.12 to 2.17. The mean value for G_{sun} is approximately 1367 W/m². Over the deep ocean the diffuse reflectance, ρ_g , is approximately 0.05. The clearness index, k_t varies between 0 and 1, with typical values between 0.2 (overcast) and 0.8 (no clouds).

$$\tau_d = \begin{cases} 1 - 0.09k_t & \text{for } k_t \leq 0.22 \\ 0.9511 - 0.1604k_t + 4.388k_t^2 - 16.638k_t^3 + 12.338k_t^4 & \text{for } 0.22 < k_t \leq 0.8 \\ 0.165 & \text{for } k_t > 0.8 \end{cases} \quad (2.12)$$

$$\tau_b = 1 - \tau_d \quad (2.13)$$

$$G_0 = G_{sun}k_t \sin \gamma_{sun} \quad (2.14)$$

$$G_{beam} = \frac{G_0\tau_b}{\sin \gamma_{sun}} \quad (2.15)$$

$$G_{diff} = G_0\tau_d \quad (2.16)$$

$$G_{gnd} = G_0\rho_g \quad (2.17)$$

Next, the beam incidence angle on the solar array (θ) and the solar array slope angle (β) are determined. These angles depend on the orientation of the solar panel with respect to the sun and the vertical, respectively. The solar panel is assumed to be in the plane of the wing, therefore the aircraft orientation needs to be estimated from the state and control variables. In the case where there is no vertical wind component, the aircraft's pitch angle (θ_p) and heading angle (ψ_p) are computed using

Eqs. 2.18 and 2.19, where C_{L_α} is the aircraft's lift curve slope.

$$\theta_p = \gamma + \frac{C_L}{C_{L_\alpha}} \cos \phi \quad (2.18)$$

$$\psi_p = \psi + \frac{C_L}{C_{L_\alpha}} \sin \phi \quad (2.19)$$

The solar panel slope angle is given by Eq. 2.20 and the incident beam angle by Eq. 2.21. Here ψ_{sun} and γ_{sun} are the sun's azimuth and elevation angles, respectively. Figure 2.3 illustrates the relationship between the solar panel orientation and the sun position in the sky.

$$\beta = \arccos(\cos \theta_p \cos \phi) \quad (2.20)$$

$$\begin{aligned} \theta = & \arccos(-\sin \theta_p \cos \psi_p \cos \phi \cos \gamma_{sun} \cos \psi_{sun} - \sin \psi_p \sin \phi \cos \gamma_{sun} \cos \psi_{sun} \\ & - \sin \theta_p \sin \psi_p \cos \phi \cos \gamma_{sun} \sin \psi_{sun} + \cos \psi_p \sin \phi \cos \gamma_{sun} \sin \psi_{sun} \\ & + \cos \theta_p \cos \phi \sin \gamma_{sun}) \end{aligned} \quad (2.21)$$

The slope angle determines the proportions of diffuse irradiance that comes from the sky and from ground reflectance. The incident beam irradiance is a function of the incident light angle. For an incidence angle between 0 and 90 degrees the irradiance reaching the panel varies as the cosine of the angle. For angles greater than 90 degrees there is no incident radiation as the beam radiation is hitting the back of the panel. This function is not differentiable at 90 degrees, which will present a problem for the optimization methods used. Instead a smooth approximation is used, and is presented in Eq. 2.22. Here a , b , c , and d are cubic polynomial coefficients to smoothly transition between the cosine function and zero over a given angle range. A smooth transition between 89 and 91 degrees is used in this work.

$$f(\theta) = \begin{cases} \cos \theta & \text{for } \theta \leq 89^\circ \\ a\theta^3 + b\theta^2 + c\theta + d & \text{for } 89^\circ < \theta \leq 91^\circ \\ 0 & \text{for } \theta > 91^\circ \end{cases} \quad (2.22)$$

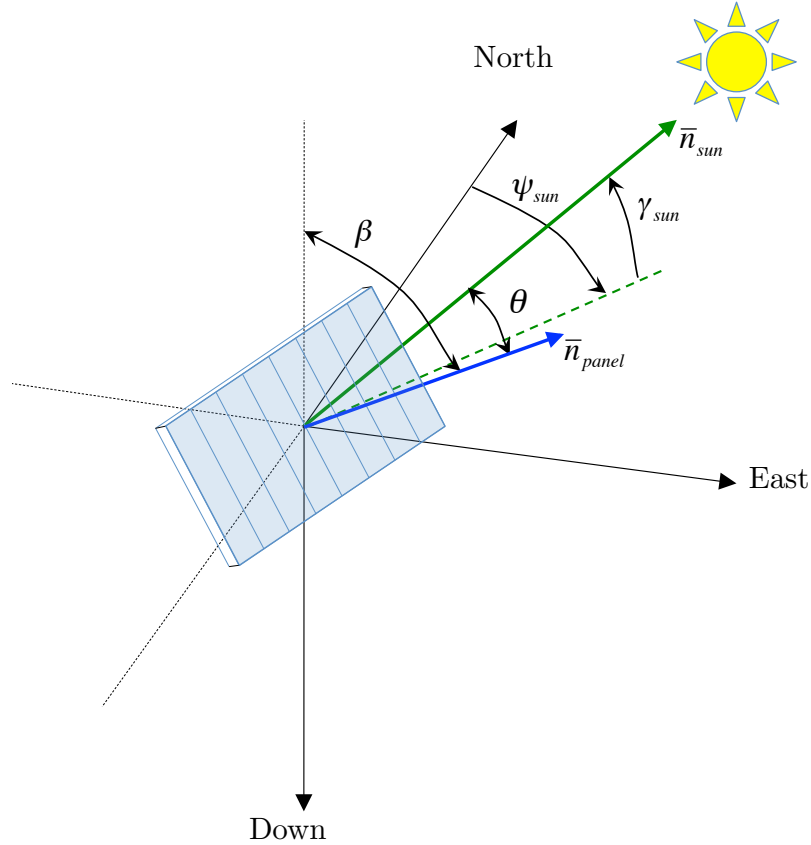


Figure 2.3: Diagram showing the solar panel orientation (\bar{n}_{panel}), sun location (γ_{sun} , ψ_{sun}), solar elevation angle (β), and incident beam angle (θ). The dashed line is a projection of the unit vector pointing at the sun into the North-East plane.

2.1.6 Wind Models

Trajectory optimization results in Section 2.3 will be presented for a number of different wind profiles. The first two wind profiles only vary in the z spatial direction. The final wind profile varies with both time as well as the x and z spatial directions due to its dependence on surface waves.

The first profile considered is a linear boundary layer where the wind speed increases linearly with altitude. The wind velocities and acceleration partial derivatives are given by Eqs. 2.23. The parameter ($\frac{V_{ref}}{h_{ref}}$), which has units of $1/s$, defines the wind gradient strength.

$$W_x = \frac{V_{ref}}{h_{ref}} z \quad (2.23a)$$

$$W_y = W_z = 0 \quad (2.23b)$$

$$\frac{\partial W_x}{\partial z} = \frac{V_{ref}}{h_{ref}} \quad (2.23c)$$

$$\frac{\partial W_x}{\partial t} = \frac{\partial W_x}{\partial x} = \frac{\partial W_x}{\partial y} = 0 \quad (2.23d)$$

$$\frac{\partial W_y}{\partial t} = \frac{\partial W_y}{\partial x} = \frac{\partial W_y}{\partial y} = \frac{\partial W_y}{\partial z} = 0 \quad (2.23e)$$

$$\frac{\partial W_z}{\partial t} = \frac{\partial W_z}{\partial x} = \frac{\partial W_z}{\partial y} = \frac{\partial W_z}{\partial z} = 0 \quad (2.23f)$$

The next profile more closely approximates the wind profile seen in the lower atmospheric boundary layer over the Earth's surface in a neutrally buoyant atmosphere. Under these conditions the boundary layer follows a log profile. The wind velocities and wind acceleration partial derivatives for this profile are given by Eqs 2.24.

$$W_x = -V_{ref} \frac{\log \frac{z}{h_0}}{\log \frac{h_{ref}}{h_0}} \quad (2.24a)$$

$$W_y = W_z = 0 \quad (2.24b)$$

$$\frac{\partial W_x}{\partial z} = \frac{-V_{ref}}{z \log \frac{h_{ref}}{h_0}} \quad (2.24c)$$

$$\frac{\partial W_x}{\partial t} = \frac{\partial W_x}{\partial x} = \frac{\partial W_x}{\partial y} = 0 \quad (2.24d)$$

$$\frac{\partial W_y}{\partial t} = \frac{\partial W_y}{\partial x} = \frac{\partial W_y}{\partial y} = \frac{\partial W_y}{\partial z} = 0 \quad (2.24e)$$

$$\frac{\partial W_z}{\partial t} = \frac{\partial W_z}{\partial x} = \frac{\partial W_z}{\partial y} = \frac{\partial W_z}{\partial z} = 0 \quad (2.24f)$$

There are three parameters that describe the shape of the log boundary layer profile: V_{ref} is the reference wind speed, h_{ref} is the height at which the reference wind speed is specified, and h_0 is the surface roughness length. The surface roughness length is not equal to the height of roughness features, but is related to them. Typical

values vary between about 10^{-4} m for calm water to 0.03 m for cut grass or a very rough sea to 1 m for the center of large town [24]. For most of the results presented in this thesis the log boundary layer shape will be used with $h_{ref} = 10$ m and $h_0 = 0.03$ m. A ten meter reference altitude is used since this is the height at which satellite based surface wind measurements are reported. A surface roughness length of 0.03 m was chosen to match values used by previous researchers and because it is a reasonable value for a rough sea [13].

Figure 2.4 illustrates this boundary layer profile with $V_{ref} = 10$ m/s, $h_{ref} = 10$ m, and $h_0 = 0.03$ m. Note that the wind speed predicted by a log boundary layer becomes non-physical for altitudes less than h_0 . In the trajectory optimization results presented later, the aircraft will be constrained from flying near or below this altitude.

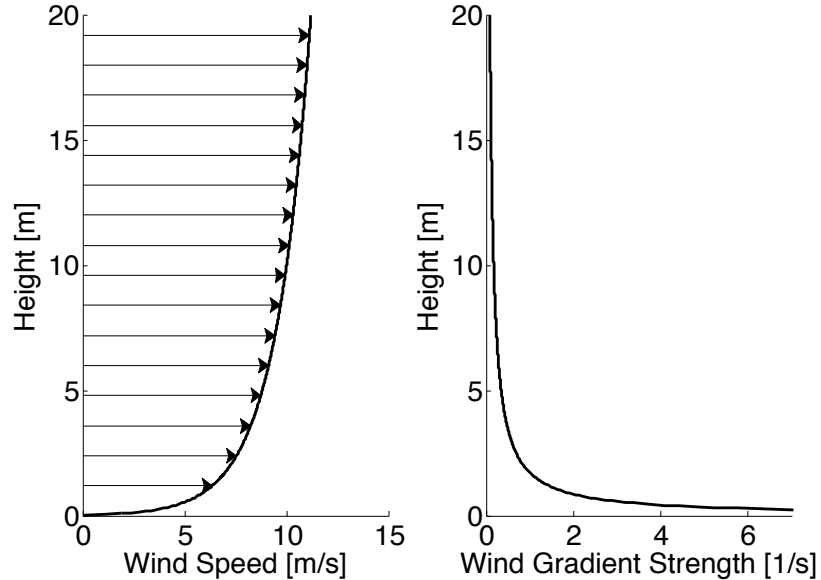


Figure 2.4: Log boundary layer wind profile shape and wind gradient strength as a function of altitude for $h_0 = 0.03$ m, $h_{ref} = 10$ m, and $V_{ref} = 10$ m/s.

The final boundary layer considered models the influence of waves on the wind field. The interactions between winds and waves is complex and the subject of extensive research by climate scientists seeking to model the exchanges of momentum and energy across the atmosphere-ocean interface [25, 26, 27, 28, 29, 30, 31, 32]. For

the dynamic soaring problem we are interested in how the wave surface impacts the wind field, not in the momentum and energy exchange. A simple parametric model was developed to capture the primary effects of waves on the wind field. It was derived based on experimental results and computer simulation results in the ocean and atmospheric interaction literature [26, 30, 31, 32].

In reality, ocean gravity waves are stochastic, and follow a predictable energy spectrum [26]. Correlations exist between the wind speed measured 10 meters above the surface and the wave spectrum. In fact, these correlations are used to predict the surface wind speed with satellite based radar backscatter measurements [33]. Due to spectral nature of surface gravity waves, there is no simple repeating wave pattern, making cyclic trajectory optimization impossible. Instead, our model reduces the parameter space by assuming that all of the energy is concentrated at the peak frequency in the energy spectrum. This will be justified by looking at the velocity perturbation equations that follow, where it is clear that the influence of higher frequency waves decrease more quickly with increasing altitude. In addition, higher frequency waves have less energy content and therefore smaller amplitudes to begin with. Ignoring waves at all but the peak frequency will still allow us to discern what effect, if any, the waves have on optimal trajectories. Another assumption implicit in this model is that the direction of wave motion is aligned with the wind, which is often the case for a fully developed sea.

The model is constructed as a superposition of a log boundary layer transformed to follow the contours of the waves [31] and perturbations generated by the movement of the surface waves to satisfy the no-slip condition at the interface [30]. The transformation of the log boundary layer leads to a speed up over the wave crests and a slow down in troughs as would be expected from a continuity analysis. The perturbations generated by the movement of the surface waves are sometimes referred to as “wave pumping”. This movement induces an upward velocity on the lee side of the wave, a downward velocity on the windward side and perturbations opposite those due to the transformed boundary layer at the crests and troughs. Both the coordinate transformation and the wave pumping velocities decay exponentially with altitude according to the wave number. The equations defining the simple wave model follow.

Equation 2.25 gives the log boundary layer equation assuming a rough surface where u^* is the friction velocity, $h_0 \approx 0.008 * u^{*2}$ and $\kappa \approx 0.4$ is the Von Karman constant.

$$U(z) = u^*/\kappa \log \frac{-z}{h_0} \quad (2.25)$$

Using the Pierson-Moskowitz Energy spectrum the peak frequency is given by Eq. 2.26 [26].

$$f_{peak} = \frac{0.8772g}{2\pi U(z = -19.5m)} \quad (2.26)$$

Placing all of the energy in the Pierson-Moskowitz spectrum at the peak frequency leads to Eq. 2.27 for the wave amplitude.

$$a_{peak} = 0.008719 * U(z = -10m)^2 \quad (2.27)$$

The corresponding angular frequency, wavenumber, and wavelength are given by Eqs. 2.28.

$$\omega_{peak} = 2\pi f_{peak} \quad (2.28a)$$

$$k_{peak} = \frac{\omega_{peak}^2}{g} \quad (2.28b)$$

$$\lambda_{peak} = \frac{2\pi}{k_{peak}} \quad (2.28c)$$

The wave surface height, η , defined positive downward, is given by Eq. 2.29.

$$\eta(x, t) = -a_{peak} \cos(k_{peak}x - \omega_{peak}t) \quad (2.29)$$

The x and z coordinates are transformed to ξ and ζ which follow the contour of the waves. The log boundary layer is defined in the ξ and ζ coordinate frame with z replaced by ζ in Eq. 2.25. The wind velocities are then mapped into x and z frame when calculating W_x and W_z . The coordinate transformation is given by Eqs. 2.30, where $\zeta = 0$ corresponds to the wave surface. It should be noted that the $\zeta = 0$ surface will not be exactly a sinusoid due to the exponential term, however, for long wavelengths and small amplitudes it is a good approximation.

$$\xi(x, z, t) = x + a_{peak} \exp(k_{peak}z) \sin(k_{peak}x - \omega_{peak}t) \quad (2.30a)$$

$$\zeta(x, z, t) = -z - a_{peak} \exp(k_{peak}z) \cos(k_{peak}x - \omega_{peak}t) \quad (2.30b)$$

The partial derivatives of ξ with respect to the x and z coordinates are required to map the wind velocities and are given by Eqs. 2.31.

$$\frac{\partial \xi(x, z, t)}{\partial x} = 1 + a_{peak}k_{peak} \exp(k_{peak}z) \cos(k_{peak}x - \omega_{peak}t) \quad (2.31a)$$

$$\frac{\partial \xi(x, z, t)}{\partial z} = a_{peak}k_{peak} \exp(k_{peak}z) \sin(k_{peak}x - \omega_{peak}t) \quad (2.31b)$$

The wind velocities due to the transformed log boundary layer are given by Eqs. 2.32.

$$W_{x_{log}} = U(\zeta(x, z, t)) * \frac{\partial \xi(x, z, t)}{\partial x} \quad (2.32a)$$

$$W_{z_{log}} = U(\zeta(x, z, t)) * \frac{\partial \xi(x, z, t)}{\partial z} \quad (2.32b)$$

The perturbation velocities induced by wave pumping are given by Eqs. 2.33. These are derived from differentiating the surface coordinates moving at the wave speed $\sqrt{\frac{g}{k_{peak}}}$ and applying an exponential decay with altitude as shown experimentally in Ref. [30].

$$W_{x_{pump}} = -a_{peak} \sqrt{gk_{peak}} \cos(k_{peak}x - \omega_{peak}t) \exp(-k_{peak}\zeta(x, z, t)) \quad (2.33a)$$

$$W_{z_{pump}} = -a_{peak} \sqrt{gk_{peak}} \sin(k_{peak}x - \omega_{peak}t) \exp(-k_{peak}\zeta(x, z, t)) \quad (2.33b)$$

$$(2.33c)$$

The final equations defining the wind-wave boundary layer are given by Eqs. 2.34. The inputs to this model are the friction velocity, u^* , which defines the reference wind speed, and the wave amplitude, a_{peak} . In the model, the wave amplitude is a function of u^* , however, as will be discussed later, a sequence of trajectory optimizations will be performed with slowly increasing wave amplitudes in order to improve convergence

at the desired wave amplitude. An example wave field is shown in Fig. 2.5 for $u^* = 0.5$ m/s and $a_{peak} = 1$ m.

$$W_x = W_{x_{log}} + W_{x_{pump}} \quad (2.34a)$$

$$W_y = 0 \quad (2.34b)$$

$$W_z = W_{z_{log}} + W_{z_{pump}} \quad (2.34c)$$

$$\frac{\partial W_x}{\partial x} = \frac{\partial W_{x_{log}}}{\partial x} + \frac{\partial W_{x_{pump}}}{\partial x} \quad (2.34d)$$

$$\frac{\partial W_x}{\partial z} = \frac{\partial W_{x_{log}}}{\partial z} + \frac{\partial W_{x_{pump}}}{\partial z} \quad (2.34e)$$

$$\frac{\partial W_x}{\partial t} = \frac{\partial W_{x_{log}}}{\partial t} + \frac{\partial W_{x_{pump}}}{\partial t} \quad (2.34f)$$

$$\frac{\partial W_x}{\partial y} = \frac{\partial W_y}{\partial t} = \frac{\partial W_y}{\partial x} = \frac{\partial W_y}{\partial y} = \frac{\partial W_y}{\partial z} = \frac{\partial W_z}{\partial y} = 0 \quad (2.34g)$$

$$\frac{\partial W_z}{\partial t} = \frac{\partial W_{z_{log}}}{\partial x} + \frac{\partial W_{z_{pump}}}{\partial x} \quad (2.34h)$$

$$\frac{\partial W_z}{\partial x} = \frac{\partial W_{z_{log}}}{\partial z} + \frac{\partial W_{z_{pump}}}{\partial z} \quad (2.34i)$$

$$\frac{\partial W_z}{\partial z} = \frac{\partial W_{z_{log}}}{\partial t} + \frac{\partial W_{z_{pump}}}{\partial t} \quad (2.34j)$$

It should be noted that this wind-wave model ignores asymmetries in the boundary layer between the lee and windward sides of the waves that are predicted by detailed CFD simulations [31], however, it does approximate experimentally measured wave induced wind field perturbations allowing us to at least gain insight into how seabirds take advantage of waves and how UAVs might be able to as well. The most interesting effect of the waves on the wind field follows from the wave pumping, which induces a vertical wind ($W_z < 0$) on the leeward side of the waves. Most people assume there is upward moving air on the windward side of waves, as is the case when the wind is blowing up a mountain slope. Near the surface this is incorrect as the wind velocity must approach the surface velocity to satisfy the no slip condition. Therefore, the surface interface velocities are mean zero and are always significantly less than both the reference wind speed and the traveling wave speed. The wave pumping effect also explains the observations of albatross flying in the “sheltered” separated region

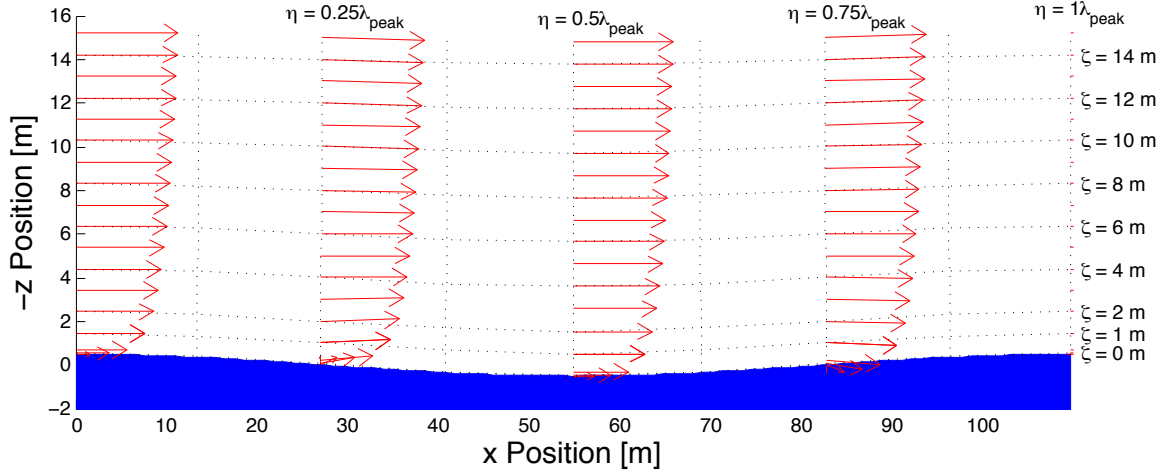


Figure 2.5: Wind-wave boundary layer profile with $u^* = 0.5$ m/s and $a_{peak} = 1$ m. The wave period is 8.383 seconds, the wave number is 0.0573 and the wavelength is 109.7 m. Lines of constant ξ and constant ζ are shown as well as the wind profile at four locations along the wave at $t = 0$. The nominal wind speed at 10 m above the surfaces is 10.65 m/s and the wave is propagating to the right at 13.09 m/s.

behind large waves [34]. Even if the boundary layer profile is significantly altered by flow separating over the wave, there are still a vertical winds near the surface induced by wave pumping that the bird may take advantage of. The next section will show that flying in a vertical wind field is the easiest way to extract energy from wind.

2.2 EOM Energy Analysis

In this section, the equations of motion are examined to better understand the mechanism for energy transfer from the wind to the aircraft. Two energy measures will be examined. The first, total energy in the inertial frame, is given by the sum of the potential and kinetic energies (Eq. 2.35). The second is the air relative total energy, which is the sum of the potential energy and the air relative kinetic energy (Eq. 2.36). The air relative kinetic energy indicates the ability of an aircraft to continue flying as the aerodynamic forces generated on the aircraft depend on the airspeed, not the inertial speed.

$$E_{total} = -mgz + \frac{1}{2}m(\dot{x}^2 + \dot{y}^2 + \dot{z}^2) \quad (2.35)$$

$$E_{air\ relative} = -mgz + \frac{1}{2}mV^2 \quad (2.36)$$

Next, Eqs. 2.35 and 2.36 are differentiated with respect to time resulting in Eqs. 2.37 and 2.38.

$$\dot{E}_{total} = -mg\dot{z} + m\dot{x}\ddot{x} + m\dot{y}\ddot{y} + m\dot{z}\ddot{z} \quad (2.37)$$

$$\dot{E}_{air\ relative} = -mg\dot{z} + mV\dot{V} \quad (2.38)$$

Eqs. 2.39 and 2.40 are derived by substituting Eqs. 2.8 and 2.9 into the above where appropriate and manipulating the resulting expressions. The thrust and generator drag are both assumed to be zero here, although their inclusion is trivial.

$$\dot{E}_{total} = -DV + \vec{W} \cdot (\vec{L} + \vec{D}) \quad (2.39)$$

$$\dot{E}_{air\ relative} = -DV - mgW_z - mVW_x \cos \gamma \cos \psi - mVW_y \cos \gamma \sin \psi + mVW_z \sin \gamma \quad (2.40)$$

In these equations, \vec{W} , \vec{L} , and \vec{D} are the wind, lift, and drag, respectively, represented as vectors expressed in the inertial frame.

From the first term in both energy rate equations it is evident that energy is always lost due to drag. In both cases, it is straightforward to see that energy should be available from the winds. From the second term in the air relative total energy rate equation (Eq. 2.40) it is clear that a negative W_z (a vertical wind) will act to increase the energy state of the vehicle. This is called the static soaring term and represents the energy source exploited by thermalling birds and sailplane pilots. Albatrosses and other seabirds may use this as a source of energy when flying near the surface on the lee side of waves. This term is also implicit in the inertial total energy rate equation (Eq. 2.39) where in most flight regimes the lift force typically has a large component in the direction of any vertical wind.

The final three terms in the air relative total energy rate equation show that in order to gain air relative total energy, the flight path and wind gradient seen by the vehicle need to have the correct alignment. Collectively these terms are sometimes referred to as the “dynamic soaring force.” As an example consider the simple linear wind field discussed in the previous section, where W_x increases linearly with altitude

(i.e. $\frac{dW_x}{dz} < 0$) and all other wind components are zero. For this wind field the wind speed acceleration is given by Eq. 2.41.

$$\dot{W}_x = -\frac{dW_x}{dz}V \sin \gamma \quad (2.41)$$

Equation 2.40 then simplifies to Eq. 2.42.

$$\dot{E}_{air\ relative} = -DV + mV^2 \frac{dW_x}{dz} \sin \gamma \cos \gamma \cos \psi \quad (2.42)$$

For this wind field $\frac{dW_x}{dz} < 0$, therefore it follows that for the second term to be positive the following relation must hold:

$$\sin \gamma \cos \gamma \cos \psi < 0 \quad (2.43)$$

For the assumed wind field the wind strength is increasing with altitude in the positive x-direction ($\psi = 0$), therefore the vehicle will extract energy from the wind when climbing into an increasing headwind ($0 < \gamma < \frac{\pi}{2}$ and $\frac{\pi}{2} < \psi < \frac{3\pi}{2}$) or when diving through a decreasing tailwind ($\frac{-\pi}{2} < \gamma < 0$ and $\frac{-\pi}{2} < \psi < \frac{\pi}{2}$). The instantaneous energy gain from the wind is maximized by flying directly into (or with) the wind ($\psi = 0$ or $\psi = \pi$), by climbing (or diving) at a 45 degree angle ($\gamma = \pm \frac{\pi}{4}$), by flying where the wind gradient is strongest, and by flying fast. The last recommendation is not always true as the power lost to drag scales with the cube of the airspeed for a given drag coefficient.

The next sections will examine the importance of major vehicle design parameters by looking at flight through two basic boundary layer shapes, each illustrating the applicability of one of the two energy perspectives described above. First, dynamic soaring through a step boundary layer will be investigated from the inertial total energy perspective to determine the step wind speed required to fly continuous cycles. Subsequently, steady climbing flight through a linear boundary layer will be examined from the air relative total energy perspective. The wind gradient required to fly a constant airspeed and angle climb will be determined.

2.2.1 Step Wind Profile Analysis

A step boundary layer is illustrated in Fig. 2.6 along with a nominal dynamic soaring trajectory through it. The wind velocities are given by Eqs. 2.44. The trajectory considered consists of only infinitesimal changes in altitude to traverse the step shear layer between the quiescent air and the moving air mass. Therefore, the potential energy can be assumed constant and only changes in kinetic energy need to be considered.

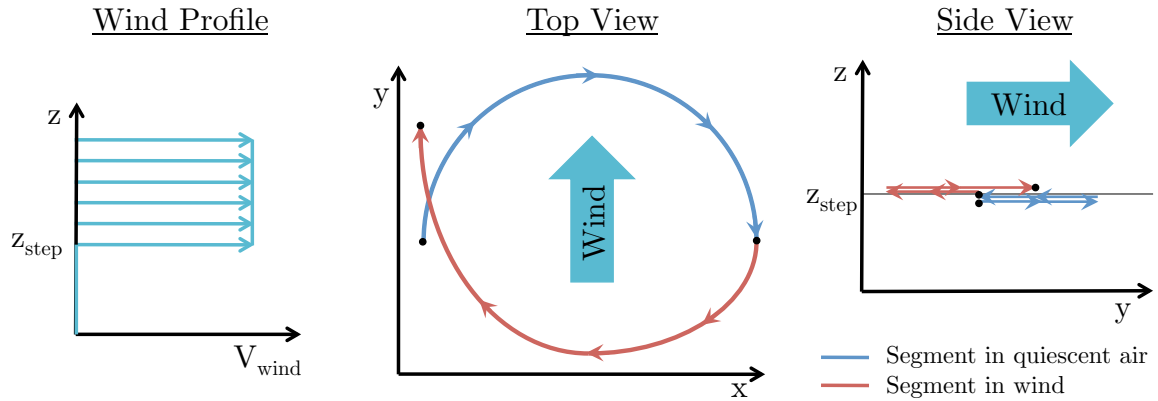


Figure 2.6: Illustration of a step wind profile and both the top and side views of a simple dynamic soaring trajectory through the shear layer.

$$W_x = \begin{cases} V_{wind} & \text{if } z > z_{step} \\ 0 & \text{if } z < z_{step} \end{cases} \quad (2.44a)$$

$$W_y = 0 \quad (2.44b)$$

$$W_z = 0 \quad (2.44c)$$

The aircraft begins the cycle in the quiescent air, flying in the direction of the wind above it. The aircraft first executes a constant radius 180 degree turn in the quiescent air. The altitude is then increased an infinitesimal amount to enter the moving air mass. Next, the vehicle executes a constant radius 180 degree turn in the moving air mass (a “J” shape viewed in the inertial frame). The aircraft then

descends an infinitesimal distance to re-enter the quiescent air and return to its initial heading, ready to repeat the cycle. This type of repeatable trajectory is referred to as a neutral energy cycle. Note that the vehicle has not necessarily returned to its initial position, if it had such a trajectory would be referred to as a neutral energy loop.

Qualitatively, the expectation is that the aircraft will be losing energy throughout the cycle due to drag. When flying in the quiescent air there is no work done on the aircraft by the wind. However, when flying in the moving air mass, the turn is executed such that the lift vector has a component in the direction of the wind, allowing the wind to do work on the aircraft. We seek to find the minimum step in wind speed such that the work done by the wind during the 180 degree turn cancels the power lost to drag over the whole cycle. The subsequent analysis makes use of the following assumptions:

1. The vehicle has a quadratic drag polar of the form: $C_D = C_{D_0} + \frac{C_L^2}{\pi R}$
2. The vehicle flies at a roughly constant airspeed (i.e. the drag is computed at the mean airspeed)
3. The vehicle flies a constant radius and constant load factor turn when viewed in the local wind reference frame

The second assumption should be relatively accurate so long as the the wind speed is much less than the airspeed. This can be viewed as assuming that the vehicle begins the trajectory at both an airspeed and an inertial speed of $V + V_{wind}/2$. Throughout the first 180 degree turn the drag reduces the airspeed and inertial speed to $V - V_{wind}/2$. After entering the moving airmass the airspeed increases to $V + V_{wind}/2$, however, the inertial speed is still $V - V_{wind}/2$. During the second 180 degree turn the airspeed again decreases to $V - V_{wind}/2$, but the inertial speed increases to $V + V_{wind}/2$. When the vehicle re-enters the quiescent air the airspeed and inertial speed are both at their original values of $V + V_{wind}/2$ and the aircraft is ready to repeat the cycle. As long as $V_{wind}/V \ll 1$ then the drag throughout the cycle should be roughly constant and near that computed when at the average airspeed of V .

Moving to the analysis, first the energy lost throughout the cycle due to drag is computed using Eq. 2.45, where $\Delta t = \frac{2\pi V}{g\sqrt{n^2 - 1}}$ is the time required to turn 360 degrees and n is the load factor.

$$\Delta E_{drag} = -D * V * \Delta t = -1/2\rho V^2 S C_D * V * \frac{2\pi V}{g\sqrt{n^2 - 1}} \quad (2.45)$$

Substitute for C_D and n to obtain Eq. 2.46.

$$\Delta E_{drag} = -\frac{\pi\rho V^4 S (C_{D_0} + \frac{C_L^2}{\pi AR})}{g\sqrt{(\frac{\rho V^2 S C_L}{2mg})^2 - 1}} \quad (2.46)$$

Next, the energy gained from the wind during the 180 degree turn in the moving air mass is computed.

$$\Delta E_{wind} = \int_0^{\Delta t/2} \vec{W} \cdot (\vec{L} + \vec{D}) dt = \int_0^{\Delta t/2} V_{wind} mg \sqrt{n^2 - 1} \sin \psi dt + \int_0^{\Delta t/2} V_{wind} D \cos \psi dt \quad (2.47)$$

As before, by assuming a constant radius turn at constant velocity the substitution $dt = \frac{V}{g\sqrt{n^2 - 1}} d\psi$ can be made to obtain Eq. 2.49.

$$\Delta E_{wind} = m V_{wind} V \int_0^\pi \sin \psi d\psi + V_{wind} D \frac{V}{g\sqrt{n^2 - 1}} \int_0^\pi \cos \psi d\psi \quad (2.48)$$

$$\Rightarrow \Delta E_{wind} = 2mVV_{wind} \quad (2.49)$$

Equating the energy gained from the wind with the energy lost to drag, we can solve for the required wind speed for a neutral energy cycle given airplane characteristics (S, C_{D_0}, AR, m), the environment (g, ρ) and the operating conditions (C_L, V).

$$V_{wind} = \frac{\pi\rho V^3 S (C_{D_0} + \frac{C_L^2}{\pi AR})}{2mg \sqrt{(\frac{\rho V^2 S C_L}{2mg})^2 - 1}} \quad (2.50)$$

Expressions for the minimum wind step speed were derived for two cases. In the first, the aircraft flies at it's maximum lift-to-drag ratio with $C_L = \sqrt{\pi AR C_{D_0}}$. For the second, both the optimum C_L and V that minimize V_{wind} are determined. Not

unexpectedly, in this case the optimum C_L corresponds to that for minimum power required. It should be noted that the optimum C_L for minimum power occurs for a much higher C_L than can be realistically achieved when assuming a quadratic drag polar for most dynamic soaring vehicles with high aspect ratios. For this reason the $(L/D)_{max}$ case should be considered more realistic. A summary of the results for the two cases is shown in Table 2.2 where the common term $\frac{mg}{S}$ is recognized as the wing loading ($\frac{W}{S}$). The derivations are not presented here in the interest of space, but are straightforward.

Table 2.2: Minimum required wind speed and the corresponding lift coefficient, airspeed, and load factor for an aircraft flying neutral energy cycles in a step boundary layer at $(L/D)_{max}$ or at the optimum V and C_L .

Parameter	$(L/D)_{max}$ Case	Optimum V and C_L Case
$V_{Wind_{opt}}$	$3^{\frac{3}{4}} \sqrt{\frac{2\pi(W/S)}{\rho AR(L/D)_{max}}}$	$4^{\frac{3}{4}} \sqrt{\frac{\pi(W/S)}{\rho AR(L/D)_{max}}}$
$C_{L_{opt}}$	$\sqrt{\pi AR C_{D_0}}$	$\sqrt{3\pi AR C_{D_0}}$
V_{opt}	$2\sqrt{\frac{\sqrt{3}(L/D)_{max}(W/S)}{\pi\rho R}}$	$2\sqrt{\frac{(L/D)_{max}(W/S)}{\pi\rho R}}$
n_{opt}	$\sqrt{3}$	$\sqrt{3}$
$\frac{V_{wind_{opt}}}{V_{opt}}$	$\sqrt{\frac{3}{2} \frac{\pi}{(L/D)_{max}}}$	$\frac{\sqrt{2}\pi}{(L/D)_{max}}$

The final row of the table shows the ratio between the required wind speed step and the airspeed, which allows us to verify the validity of the assumption that $\frac{V_{wind}}{V} \ll 1$. Based on this, we expect the validity of the calculations to improve as $(L/D)_{max}$ increases. Most proposed dynamic soaring aircraft designs (and seabirds that use dynamic soaring) have lift-to-drag ratios over 20, where $V_{wind}/V \approx 0.2$ indicating that this simple analysis is at least reasonable to understand the important factors and trends in the design of a dynamic soaring aircraft.

This also indicates the primary non-dimensional result, that the important parameter for dynamic soaring is not the actual change in wind speed, but rather the change in wind speed compared to the aircraft's cruise speed. It is for this reason that albatrosses and model gliders are able to dynamic soar in reasonable wind gradients, while it is rare that sufficient wind gradients exist for manned aircraft.

In terms of aircraft design parameters, the trends are the same in both cases, only the leading constants vary. To reduce required wind step speed the aircraft should have a low wing loading, a high lift-to-drag ratio, and a high aspect ratio.

A similar analysis was performed by Lissaman in Ref. [35] where the turn radius is allowed to vary and the effect of changing airspeed is taken into account. The same expressions are obtained for n_{opt} and $\frac{V_{wind, opt}}{V_{opt}}$ as the optimum V and C_L case.

2.2.2 Wind Gradient for Constant Airspeed and Flight Path Angle Climb

Steady-state climbing flight through a linear shear layer is examined in this section. Such a trajectory is not likely to be practical to use in a typical dynamic soaring trajectory, but it provides another measure of the dynamic soaring ability of a given aircraft design. Here the goal is to determine the minimum wind gradient strength required to sustain a constant airspeed, and constant air-relative flight path angle climb. This analysis assumes that the aircraft is flying in the positive x-direction ($\psi = 0$), and as before, that the vehicle has a quadratic drag polar.

By equating the \ddot{x} and \ddot{z} equations from Eqs. 2.4 and 2.8 with the assumptions that $\psi = 0$, $\dot{\gamma} = \dot{\psi} = 0$, $W_y = W_z = 0$, and $W_x = -V \sin \gamma \frac{\partial W_x}{\partial z}$ leads to Eqs. 2.51.

$$\frac{\partial V}{\partial t} \cos \gamma = \frac{-D \cos \gamma - L \sin \gamma}{m} + V \sin \gamma \frac{\partial W_x}{\partial z} \quad (2.51a)$$

$$\frac{\partial V}{\partial t} \sin \gamma = \frac{-D \sin \gamma + L \cos \gamma - mg}{m} \quad (2.51b)$$

Multiplying the first expression above by $\sin \gamma$, the second expression by $\cos \gamma$, and subtracting the second from the first to eliminate the $\frac{\partial V}{\partial t}$ terms generates an expression for the lift in terms of airspeed, flight path angle, and wind gradient strength (Eq. 2.52):

$$L = mg \cos \gamma + V \sin^2 \gamma \frac{\partial W_x}{\partial z} = \frac{1}{2} \rho V^2 S C_L. \quad (2.52)$$

After solving for C_L and plugging the result into the quadratic drag polar, Eq. 2.9e is manipulated to obtain Eq. 2.53. This is an expression for the airspeed acceleration,

\dot{V} , as a function of the environment (g , $\frac{\partial W_x}{\partial z}$, ρ), flight conditions (γ , V), and vehicle design parameters (m, S, AR, C_{D_0})

$$\dot{V} = -\frac{\rho V^2 S C_{D_0}}{2m} - \frac{2m}{\rho V^2 S \pi R} (g \cos \gamma + V \sin \gamma \frac{\partial W_x}{\partial z})^2 - g \sin \gamma + V \sin \gamma \cos \gamma \frac{\partial W_x}{\partial z}. \quad (2.53)$$

By setting $\dot{V} = 0$ and solving for $\frac{\partial W_x}{\partial z}$ an expression for the required wind gradient for a constant climb angle with no airspeed loss can be derived. Note that Eq. 2.53 is quadratic in $\frac{\partial W_x}{\partial z}$. Solving the quadratic equation leads to Eq. 2.54 for the required linear wind gradient strength to fly at a constant flight path angle and airspeed. If real solutions exist, the “–” solution is the physical one.

$$\begin{aligned} \frac{\partial w_x}{\partial z} = & (4mg \cos \gamma \sin \gamma - \rho V^2 S \pi R \cos \gamma) \\ & \pm \sqrt{16m^2 g^2 \cos^2 \gamma \sin^2 \gamma - 8mg\rho V^2 S \pi R \cos^2 \gamma \sin \gamma} \\ & + \rho^2 V^4 S^2 \pi^2 R^2 \cos^2 \gamma - 8mg\rho V^2 S \pi R \sin^3 \gamma \\ & + 16m^2 g^2 \sin^4 \gamma - 4\rho^2 V^4 S^2 C_{D_0} \pi R \sin^2 \gamma - 16m^2 g^2 \sin^2 \gamma \Big) \\ & /(mV \sin^3 \gamma) \end{aligned} \quad (2.54a)$$

It is reasonable to assume that a minimum required wind gradient strength exists for a given aircraft design. There are no closed form solutions for the optimum V and γ , instead numerical investigations are carried out. For the following examples, Wandering Albatross parameters as used by Sachs are assumed [13]. The parameter values are repeated in Table 2.3.

Table 2.3: Model albatross parameter values used (Ref. [13]).

Parameter	Value
Mass [kg]	8.5
Wing Area [m^2]	0.65
Aspect Ratio	16.81
C_{D_0}	0.033
$(L/D)_{max}$	20
Span [m]	3.306

Figure 2.7 shows the required linear wind gradient strength to fly at a given airspeed as a function of climb angle. It is obvious that there is a optimum climb angle for each airspeed and that there is an overall optimal airspeed. The corresponding optimum climb angles and lift coefficients are shown as a function of airspeed in Fig. 2.8. The minimum gradient strength is shown as a function of airspeed in Fig. 2.9, where the optimum gradient of 0.398 s^{-1} occurs at an airspeed of about 61 m/s , a $C_L \approx 0$, and an air relative climb angle of 35.3 degrees.

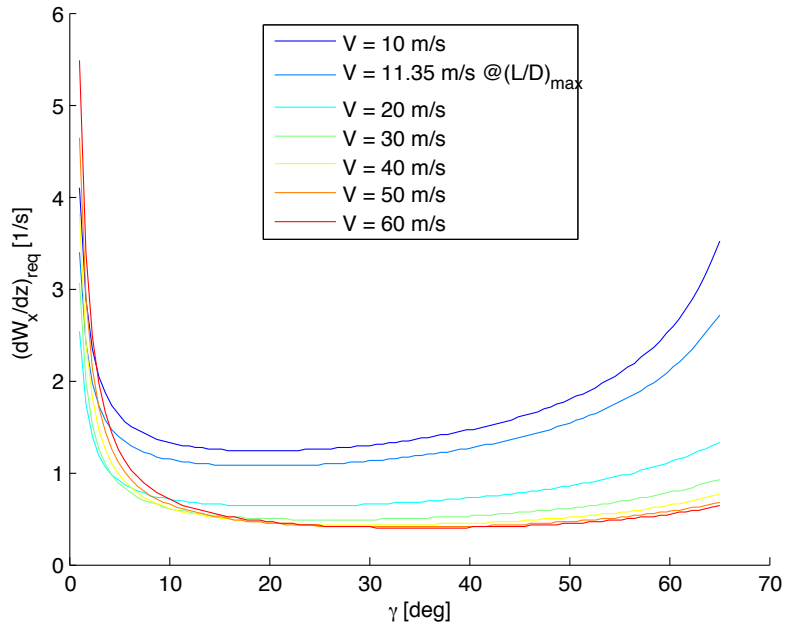


Figure 2.7: Required linear wind gradient strength for steady state flight at a given airspeed as a function of climb angle for the model Wandering Albatross.

Comparing this optimum to the still air gliding speed at $(L/D)_{max}$ of 12.6 m/s at $C_L = 1.32$, we see that the optimum is unreasonably fast and at a very low lift coefficient. It is hard to imagine an aircraft or bird accelerating to that many times its optimum gliding speed solely by climbing through a linear wind gradient. Fortunately, as seen in Fig. 2.7, the required wind gradient as a function of airspeed and flight path angle is relatively flat, indicating that a value close to the optimum is achievable at a much lower airspeed. For instance, at 20 m/s , which is a reasonable speed for the model albatross, the required wind gradient is 0.635 s^{-1} .

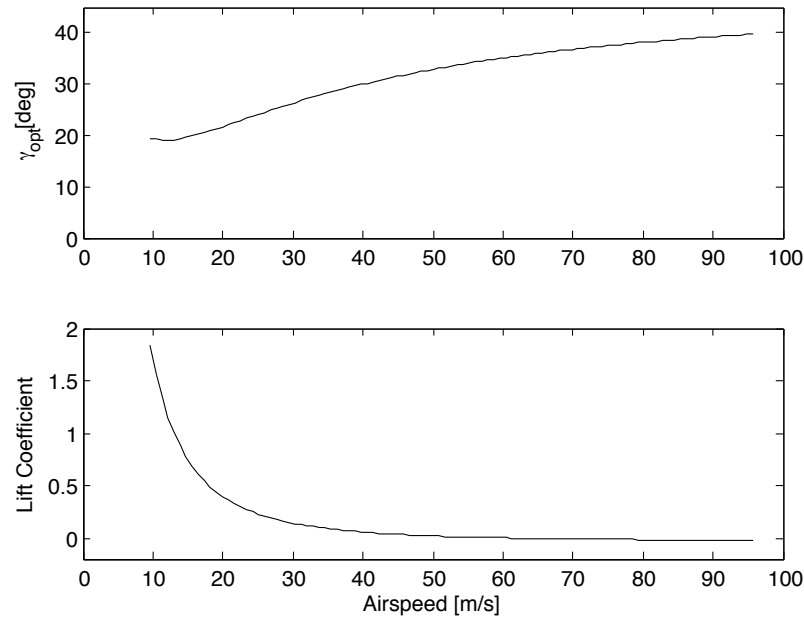


Figure 2.8: Optimum climb angle and lift coefficient for a steady climb as a function of airspeed for the model Wandering Albatross.

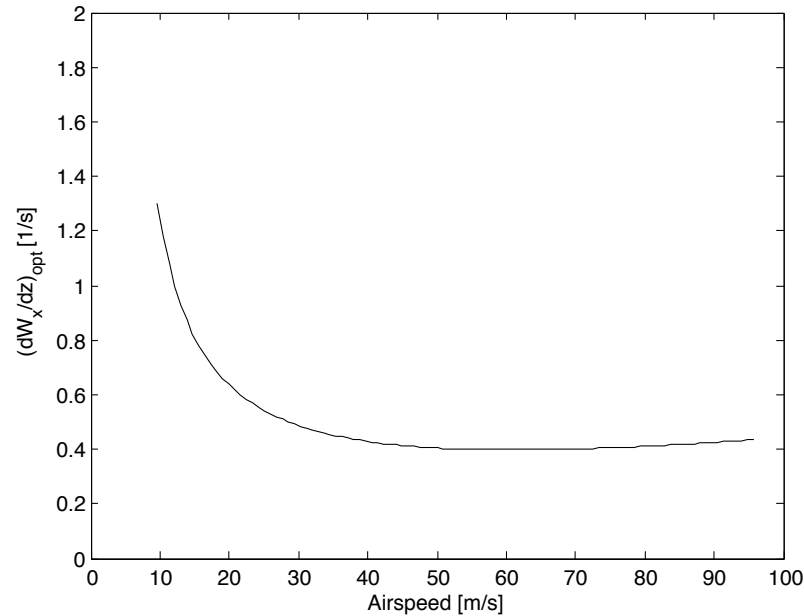


Figure 2.9: Minimum linear wind gradient strength for a steady climb as a function of airspeed for the model Wandering Albatross.

In the following sensitivity analysis we will take the required wind gradient at the C_L for $(L/D)_{max}$ as a reasonable performance metric for comparing different designs. For the baseline it occurs at an airspeed of 11.35 m/s where the required wind gradient strength is 1.072 s^{-1} . Figure 2.10 shows the variation in the required gradient strength for $\pm 50\%$ variations of m , S , \mathcal{R} , and C_{D_0} from the baseline albatross parameters.

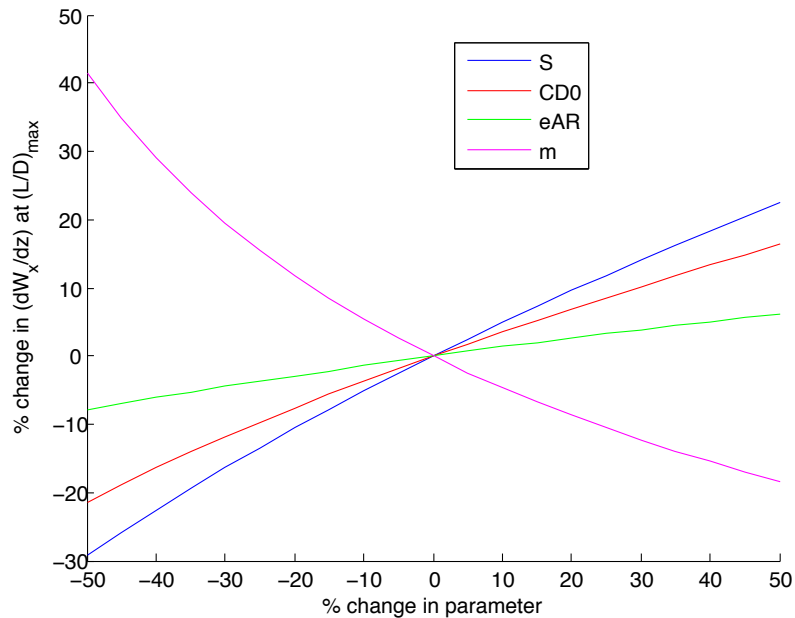


Figure 2.10: Sensitivity plot showing the % variation in required linear wind gradient strength for a constant airspeed and air relative angle climb as a function of the % variation in S , \mathcal{R} , C_{D_0} , and m about the baseline model albatross from Table 2.3.

From the sensitivity plot it is clear that a higher mass and/or smaller wing area (i.e. higher wing loading) reduces the required wind gradient strength for a constant airspeed and angle climb. As expected a lower C_{D_0} also decreases the required wind gradient. Somewhat surprisingly, decreasing the aspect ratio, which also decreases $(L/D)_{max}$, decreases the required wind gradient strength.

The wing loading and aspect ratio trends run counter to the step wind profile results of the previous section which favored lower wing loadings and higher aspect ratios. Intuitively, the aspect ratio trend is due to the difference between constantly turning flight at relatively high lift coefficients for the step wind profile and zero bank

flight at low lift coefficients for the climb through a constant wind gradient. Based on observed dynamic soaring trajectories in nature, and from the trajectory optimization results that follow it will be clear that realistic trajectories include mostly turning flight, leading to the conclusion that high aspect ratios are preferable. This is seen among dynamic soaring birds, which all have aspect ratios in the range of 12 to 16 (Wandering Albatross, Black-Browed Albatross, Giant Petrel). In contrast, other seabirds that do not use boundary layer dynamic soaring have aspect ratios in the range of 7 to 10 (Wilson's Petrel, Cape Pigeon) [36]. The wing loading is likely set by a balance between the desire for high net travel speeds which favors higher wing loadings and the ability to fly in lighter winds which favors lower wing loadings.

2.3 Trajectory Optimization

This section details the formulation of a trajectory optimization problem, then discusses a number of solution methods used in the literature. The efficiency and robustness of these methods are compared. In the next chapter, a number of key results are presented. These results and those of similar problems are then used in subsequent chapters. In Chapter 4, optimal trajectories are used as initial target trajectories for the mid-level model predictive controller as well as to build up performance polars that are used by the high-level mission planner. In Chapter 5, characteristics of optimal trajectories such as travel speed or minimum required wind speed are used as objective functions for aircraft design studies.

2.3.1 Problem Formulation

The goal of the trajectory optimization problem is to find the state and control time histories that minimize a selected cost function while satisfying the three degree of freedom point mass equations of motion (see Section 2.1) and any additional constraints. The general optimal control problem is defined below, where J is the objective function, \bar{x} is the set of state time histories, \bar{u} is the set of control time histories, g is a set of inequality constraints, and h is a set of equality constraints.

$$\begin{aligned}
\text{Min : } & J(\bar{x}, \bar{u}) \\
\text{w.r.t. : } & \bar{x}, \bar{u} \\
\text{s.t. : } & g(\bar{x}, \bar{u}) \leq 0 \\
& h(\bar{x}, \bar{u}) = 0
\end{aligned}$$

For dynamic soaring trajectories a common constraint will be the requirement that the optimal trajectories are periodic in some or all of the state variables. In the majority of problems, the North and East positions will not require periodicity, but all other states will have the periodic boundary conditions imposed. This implies that for fixed wind conditions the optimal trajectories are repeatable neutral energy cycles.

The state variables, control variables, and equations of motion that are used were derived in Section 2.1.2. The state variables include the x , y , and z positions, airspeed (V), air relative flight path angle (γ), air relative heading angle (ψ) and where applicable the battery energy state (E). The control variables include the lift coefficient (C_L), bank angle (ϕ), and where applicable the thrust (T) and generator drag (D_{gen}). In addition, the cycle period, t_{cycle} , and reference wind speed V_{ref} may be included as variables in the optimization.

There are many potentially interesting objectives that could be used, however, we will only consider the following two objectives in this work:

1. Minimum reference wind speed ($J = V_{ref}$)
2. Maximum net speed $\left(J = -\frac{\sqrt{\Delta x^2 + \Delta y^2}}{t_{cycle}} \right)$

The reference wind speed will depend on the boundary layer shape being considered, but can generally be thought of as a multiplicative scale factor on a general boundary layer shape. It will be used to define the wind regime that a given design is capable of flying in. The net speed is defined as the ground distance travelled between the start and end of a cycle divided by the cycle period. This objective will be used to generate

speed versus direction polars that characterize the performance of a given design in known wind conditions.

In addition to these objectives, previous researchers have used objectives such as minimum cycle time [22], maximum distance traveled [18, 37], altitude gain [22], and minimum average power or thrust [38, 21, 39].

In addition to satisfying the equations of motion, the solution must satisfy additional inequality and equality constraints. Table 2.4 lists the constraints that are used throughout this work, some subset of which are applied to any given trajectory optimization problem.

Table 2.4: List of trajectory optimization constraints, the state variables they depend on, and whether or not they are equality or inequality constraints.

Constraint	State Variables	= or \leq	Notes
Equations of motion	All	=	Eqs. 2.9 and 2.11
State bounds	$x, y, z, V, \gamma, \psi, E$	\leq	
Control bounds	C_L, ϕ, T, D_{gen}	\leq	
Propulsive power bound	V, T	\leq	$P = TV$
Generator power bound	V, D_{gen}	\leq	$P_{gen} = D_{gen}V$
Control rates	$\frac{\partial C_L}{\partial t}, \frac{\partial \phi}{\partial t}, \frac{\partial T}{\partial t}, \frac{\partial D_{gen}}{\partial t}$	\leq	
Propulsive power rate	$\frac{\partial P}{\partial t}$	\leq	
Generator power rate	$\frac{\partial P_{gen}}{\partial t}$	\leq	
Load factor	V, C_L	\leq	$n = \frac{\frac{1}{2}\rho V^2 S C_L}{mg}$
Wingtip height	z, γ, ϕ	\leq	$h_{tip} = z \pm \frac{b}{2} \cos(\gamma) \sin(\phi)$
Initial conditions	All	= or \leq	Some subset of states
Periodicity conditions	All	=	Some subset of states
Flight direction	x, y	=	$\psi_{net} = \tan^{-1} \Delta y / \Delta x$
Wave phase angle	x	=	Only for wind-wave BL
Battery energy rate	E	=	$E_{rate} = \frac{\Delta E}{t_{cycle}}$

2.3.2 Solution Methodologies

The dynamic soaring trajectory optimization problem has received a fair amount of attention in the literature with many different solution algorithms applied to it. In early research on the topic, the equations of motion were simplified in order to

derive analytic solutions or to apply simple numerical methods [40, 41, 42, 43]. Later, methods for finding optimal trajectories that satisfied the full equations of motion were derived.

Sachs describes using a “sophisticated” algorithm in his work [44, 13], which was likely the shooting method applied in Ref. [45]. In this later work he derives the Hamiltonian of the problem and identifies conditions for optimality. By minimizing the Hamiltonian, the optimum bank angle and lift coefficient are derived. A number of switching conditions are found that are due to the minimum altitude constraints and bounds on the control variables. A multiple shooting method is then used to solve the resulting boundary value problem and find the optimal trajectory. Sachs’ results from Ref. [13] will be used as a baseline for comparison to other trajectory optimization methods.

A number of researchers have applied direct optimization methods solve for the optimal trajectory on a discretized representation of the problem. Zhao uses a collocation approach based on 3rd degree Gauss-Lobatto quadrature [22, 46]. In this method, the trajectory is discretized into a fixed number of control points that are equally spaced in time. The discretized EOM are satisfied at the midpoints of the time intervals. The set of equations that are used to calculate the EOM constraints are given by Eqs. 2.56 to 2.58. Here N is the number of collocation points, \bar{f} is the vector function representing the equations of motion, \bar{x}_i is the vector of states at collocation point i , \bar{u}_i is the vector of controls at collocation point i , Δt_i is the i^{th} time interval, subscript m represents values at the midpoint of the interval, and $C_{k+(i-1)(N-1)}$ represents the i^{th} equality constraint corresponding to the k^{th} equation of motion.

$$\bar{x}_{m_i} = \frac{1}{2}(\bar{x}_i + \bar{x}_{i+1}) - \frac{1}{8}(\bar{f}(\bar{x}_{i+1}, \bar{u}_{i+1}) - \bar{f}(\bar{x}_i, \bar{u}_i))\Delta t_i \quad (2.56)$$

$$\bar{u}_{m_i} = \frac{1}{2}(\bar{u}_i + \bar{u}_{i+1}) \quad (2.57)$$

$$C_{i+(k-1)(N-1)} = x_{i+1}^k - x_i^k - \frac{1}{6}(f_k(\bar{x}_i, \bar{u}_i) + 4f_k(\bar{x}_{m_i}, \bar{u}_{m_i}) + f_k(\bar{x}_{i+1}, \bar{u}_{i+1}))\Delta t_i \quad (2.58)$$

The first equation is the estimate of the state vector at the midpoint and the last equation is known as the Hermite-Simpson system constraint. This method is

equivalent to assuming piecewise constant control histories and piecewise linear state histories [21]. Since the system constraints for time interval i only depend on the state and control values at times i and $i+1$, the resulting constraint Jacobian matrix is sparse. The additional constraints given in Table 2.4 may also be discretized and evaluated at the collocation points. Due to the sparsity structure of the Jacobian matrix, the optimization problem corresponding to the collocation method can be efficiently solved with a sparse nonlinear SQP method like the one implemented in SNOPT [47]. This method will be used in the majority of our work due to its speed, convergence properties and solution quality compared to the other methods.

Pseudospectral methods are similar to the collocation method in that the equations of motion are discretized in time. However, the control points are intelligently chosen to minimize errors in the constraint equations. In addition, more recent implementations include knot points that allow for switching conditions in the optimal control problem to be captured [48]. For this work the dynamic soaring optimal control problem was implemented in the General Pseudospectral Optimal Control Software (GPOPS) [49]. GPOPS implements both the Gauss pseudospectral method and the Radu pseudospectral method.

The final method considered relies on the observation that the dynamic soaring equation of motion are differentially flat [50]. The idea behind differential flatness is to find the inverse dynamics of a system based on a new set of outputs. The dimensionality of the trajectory optimization problem is reduced by mapping the state space into a lower dimensional output space. Additionally, by inverting the dynamics, the equations of motion for a given trajectory are automatically satisfied, and it is only necessary to satisfy any additional constraints.

For the differentially flat dynamic soaring trajectory optimization problem the states are x , y , z , V , γ , and ψ , the control inputs are C_L , ϕ , and T . In this case, the outputs of the system are selected to be the same as the states and controls, and the differentially flat outputs are only x , y , and z . The remainder of the outputs are expressed as a function of the flat outputs and a finite number of their time derivatives.

The flat outputs are typically expressed as a series of basis functions. The implementation used by Deittert in Ref. [50] was followed in this work. It uses a truncated Fourier series with N terms for the outputs and includes additional terms representing the net speed and direction of flight as well as an altitude offset. The basis functions are given by Eqs. 2.59.

$$x_i = a_{x_0} + V_{net} \cos(\psi_{net}) t_i + \sum_{j=1}^N a_{x_j} \sin\left(\frac{2\pi j t_i}{t_{cycle}} + \eta_{x_j}\right) \quad (2.59a)$$

$$y_i = a_{y_0} + V_{net} \sin(\psi_{net}) t_i + \sum_{j=1}^N a_{y_j} \sin\left(\frac{2\pi j t_i}{t_{cycle}} + \eta_{y_j}\right) \quad (2.59b)$$

$$z_i = a_{z_0} + \sum_{j=1}^N a_{z_j} \sin\left(\frac{2\pi j t_i}{t_{cycle}} + \eta_{z_j}\right) \quad (2.59c)$$

By selecting these basis functions periodicity constraints are automatically satisfied. Given the series approximations for the flat outputs and their time derivates, the other states may then be calculated. V , γ , and ψ are calculated using the equations in Section 2.1.1. Finally, C_L , ϕ and T are calculated using Eqs. 2.9d to 2.9f.

While the equations of motion are automatically satisfied for any x , y , z trajectory, additional constraints such as state bounds, control bounds, and the load factor are not. These constraints are typically evaluated at some fixed number of time points along the trajectory. Care needs to be taken to ensure that enough points are chosen so that the trajectory does not exceed the bounds between the fixed time points.

The optimal trajectory is identified by running a gradient based optimizer to minimize the objective function by varying the basis function parameters (a_{x_0} , a_{y_0} , a_{z_0} , V_{net} , ψ_{net} , and a_{x_j} , a_{y_j} , a_{z_j} , η_{x_j} , η_{y_j} , η_{z_j} for $j = 1, \dots, N$) while satisfying the additional constraints. The resulting problem has a dense Jacobian matrix as almost all of the constraint outputs depend on all of the basis function parameters. SNOPT was used to solve the optimization problem in this work, however, as the Jacobian is dense it defaults to using the dense NPSOL solver. Despite the dense problem structure, an advantage of this method is that the number of design variables and constraints may be significantly reduced compared to the collocation method. As will

be seen in the next section, this method performs well, but is not quite as fast or robust as the collocation method.

2.3.3 Validation

The solution methodologies from the previous section were all tested on the same problem to compare solution quality and computation times. The minimum wind speed result generated by Sachs in Ref. [13] for the model Wandering Albatross (Table 2.3) was used as the point of comparison. For this problem the lift coefficient was bounded between -0.2 and 1.5 , the maximum bank angle was set to ± 80 degrees, the minimum altitude allowed was 1.5 m, and the maximum load factor was limited to 3 . No thrust is allowed and the battery energy EOM is ignored. Additionally, all of the rate constraints and the wingtip height constraints are not imposed. The wind profile is the log boundary layer with $h_{ref} = 10$ m and $h_0 = 0.03$ m.

All of the following results were generated on a 2008 MacbookPro with a 2.4 GHz Intel Core 2 Duo processor and 4 GB of RAM. Solutions for the collocation method and differential flatness method were generated using SNOPT. The objective and constraint routines were coded in Fortran and compiled using the Intel Fortran Compiler. The pseudospectral method results were generated using the GPOPS library running through Matlab [49]. The GPOPS library also uses SNOPT to drive the optimization.

The collocation results were generated using both analytic expressions for the Jacobian elements, and using finite differencing with a step length of $1.5\text{e-}8$. The trajectory was discretized into 51 equally spaced (in time) collocation points. The convergence tolerance for the design variables, objective and constraints were all set to $1\text{e-}8$. The following set of initial conditions were used:

- $t_{cycle} = 7$
- $x_i = y_i = t_i * 13.75$
- $z_i = -8$
- $V_i = 20.625 + 6.875 \cos(2\pi t_i/t_{cycle})$

- $\gamma_i = 2\pi/9 \sin(2\pi t_i/t_{cycle})$
- $\psi_i = \pi/2(1 - \sin(2\pi t_i/t_{cycle}))$
- $C_{L_i} = 0.65$
- $\phi_i = -4\pi/9 + 8\pi/9 \sin(\pi t_i/t_{cycle})$
- $T_i = 0$

Many other initial conditions were tried and a majority converged to within 0.01% of the solution for these initial conditions.

The pseudospectral result was generated using the Radau pseudospectral method in the GPOPS library. The same initial condition was used as for the collocation method. All of the derivatives were calculated using the complex step method. Other GPOPS settings included initializing the trajectory with ten intervals having three points each, turning on automatic scaling, and activating the automatic mesh refinement. Three mesh iterations were allowed with a mesh tolerance of 1e-3. Default convergence tolerances of 1e-6 were used.

Finally, three cases were run for the differential flatness method with $N=10$, 15 , and 20 Fourier series terms. In all cases, the constraints were enforced at $M=5*N$ points equally spaced in time as suggested in Ref. [50]. The initial conditions for the differential flatness method were selected by fitting a five term Fourier series to the resulting trajectories from the collocation method and initializing the additional terms to zero. The zero thrust constraint was imposed as an inequality requiring the thrust at each constraint point to be less than or equal to zero. Convergence tolerances for the objective, constraints and variables were set to 1e-6.

Qualitatively, all of the methods generated results that looked very similar to Sachs' optimal trajectory, but the minimum wind speed, optimal cycle time and final trajectory dimensions varied slightly. Results are compiled in Table 2.5 below.

Based on the computation times and extensive testing of these methods it was clear that the collocation method was both the fastest and most robust. The pseudospectral method found a similar solution, but took considerably longer than the collocation method. A Fortran implementation of the pseudospectral method would certainly

Table 2.5: Comparison of solution methodologies on the validation problem from Ref. [13]. Method: a) Sachs', b) Collocation with analytic gradients ($N=51$), c) Collocation with finite difference gradients ($N=51$), d) Pseudospectral method, e) Differential flatness ($N=10$, $M=50$), f) Differential flatness ($N=15$, $M=75$), g) Differential flatness ($N=20$, $M=100$)

Method	Objective	Cycle Time	N-S Extent	E-W Extent	Solution Time
a	8.6 m/s	7.1 s	66.2 m	66.5 m	Unknown
b	8.56011 m/s	7.0025 s	62.74 m	65.71 m	1.90 s
c	8.56120 m/s	6.9887 s	64.65 m	65.76 m	8.52 s
d	8.56402 m/s	7.0148 s	62.39 m	65.96 m	79.00 s
e	8.58863 m/s	6.9596 s	61.48 m	65.71 m	3.10 s
f	8.57855 m/s	6.9895 s	62.14 m	65.85 m	11.18 s
g	8.56926 m/s	6.9840 s	62.06 m	65.62 m	41.52 s

be faster than through the GPOPS library, however, this was not considered as the collocation method already performed well.

The differential flatness method also performed well, but it often did not converge to the correct solution if the initial conditions weren't near the optimal trajectory. The thrust constraint in the differential flatness method was the most difficult to satisfy. Even evaluating the constraints $5*N$ points was not enough to fully constrain the thrust to zero or negative values. Figure 2.11 shows the variation in thrust throughout the optimal cycle for the case with $N=15$ and $M=75$. The black dots indicate the thrust value at the constraint times, which all occur at or below zero thrust. The high frequency content of the solution is still able to achieve positive thrust at some locations between the constraint times. Additionally, the regions of negative thrust reduce the minimum wind speed performance, this is likely why the objective values are slightly higher for the differential flatness method than for the collocation method.

For the remainder of this thesis all of the trajectory optimization results are generated using the collocation method with analytic Jacobian supplied. The following results examine the importance of some settings for the collocation method. First, the importance of the convergence tolerances on the final objective function values

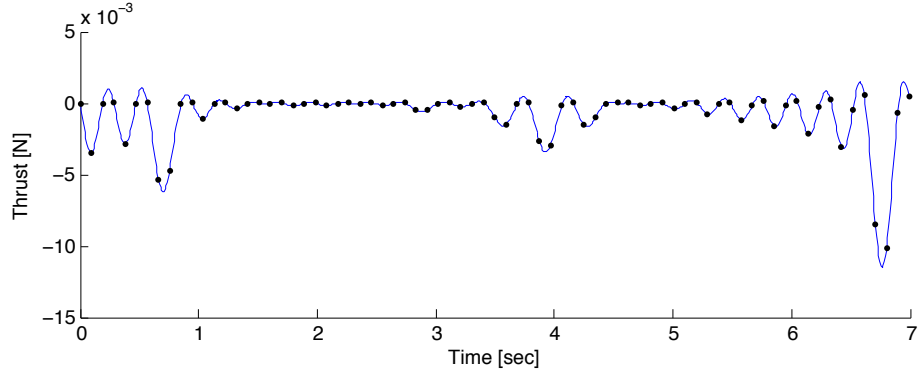


Figure 2.11: Thrust calculated at the optimum for the differential flatness method with 15 Fourier series terms and 75 constraint points. The black dots indicated the thrust value at the discrete time points that the $T \leq 0$ constraints were applied.

and the solution times were examined for the validation problem with $N=51$ collocation points. The convergence tolerances on the design variables, objective function, and constraints were varied between $1e-4$ and $1e-8$. The results are shown in Table 2.6. In all cases the objective tolerance was critical and the constraints were satisfied to roughly twice the desired number of orders of magnitude. It is clear that there is a small computation time penalty for using tighter tolerances. When generating trajectories that border on feasibility, which is always the case at some point when generating performance polars, it is important to ensure that the solutions converge as tightly as possible. For these reasons a convergence tolerance of $1e-8$ was selected.

Table 2.6: Variation in the final objective value and solution times for varying convergence tolerances for the validation problem using the collocation method with the analytic Jacobian.

Convergence Tolerance	Objective [m/s]	Solution Time [sec]
1e-4	8.56012	1.48
1e-5	8.56015	1.62
1e-6	8.56012	1.72
1e-7	8.56013	1.79
1e-8	8.56011	1.90

The next study examined the importance of the number of collocation points. Again, solutions were generated for the validation problem while varying the number of collocation points between 21 and 201. The convergence tolerances were set to 1e-8. Table 2.7 shows the variation in the number of design variables, constraints, the objective function, and the solution time for each case. The number of variables is equal to $9N+2$ (states, controls, t_{cycle} , and V_{ref}) and the number of constraints is equal to $6(N-1)+N+15$. The constraints correspond to the six EOM, the load factor, the initial conditions, and the periodicity constraints. It is clear that there is not much to be gained by using more collocation points in terms of solution accuracy for this problem as all of the objective values are within about 0.1% of each other. Unless otherwise noted, 51 collocation points were selected to provide a balance between solution time and resolution.

Table 2.7: Variation in the final objective value and solution time for different numbers of collocation points.

Points	# Variables	# Constraints	Objective [m/s]	Solution Time [sec]
21	191	156	8.55502	0.21
41	371	296	8.55940	1.20
51	461	366	8.56011	1.90
101	911	716	8.56181	7.42
151	1361	1066	8.56194	24.62
201	1811	1416	8.56206	133.32

A final validation run was conducted with the selected solution methodology, 51 collocation points, and convergence tolerances of 1e-8 to show details of the minimum wind speed trajectory for the model Wandering Albatross. Details of the trajectory are shown in Figs. 2.12 to 2.17 and may be compared to the plots presented by Sachs in Ref. [13]. As a point of comparison for future researchers, a table detailing the design variable values to 8 significant digits is presented in Table A.1 in Appendix A. As expected the trajectory exhibits the desired characteristics of turning from upwind to downwind where the wind speed is greatest and from downwind to upwind where it is lowest. This is seen clearly in Fig. 2.17 where total energy is gained from the wind at higher altitudes, but lost at lower altitudes. Examining the trajectory from the

air relative total energy perspective it is clear that energy is gained by both climbing into an increasing headwind and diving through a decreasing tailwind. In both power plots, total energy is always lost due to drag, however, the loses are greatest when the vehicle is flying the fastest and at a large load factor. The vehicle reaches its maximum load factor and lift coefficient constraints. It is also interesting to note from Fig. 2.16 that the air relative total energy is nearly constant throughout the cycle, compared to the total energy which varies dramatically.

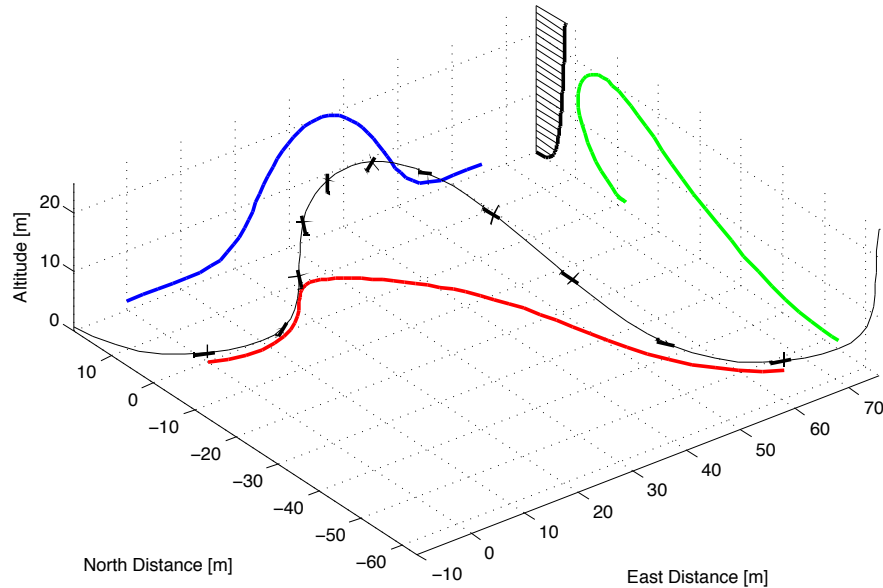


Figure 2.12: Trajectory for minimum reference wind speed (8.56 m/s) for the model Wandering Albatross flying through a log boundary layer. The boundary layer profile shown at the top of the plot indicates how far the wind travels in the time between successive instances of the vehicle along the trajectory (0.7 seconds). The colored lines show projections of the trajectory.

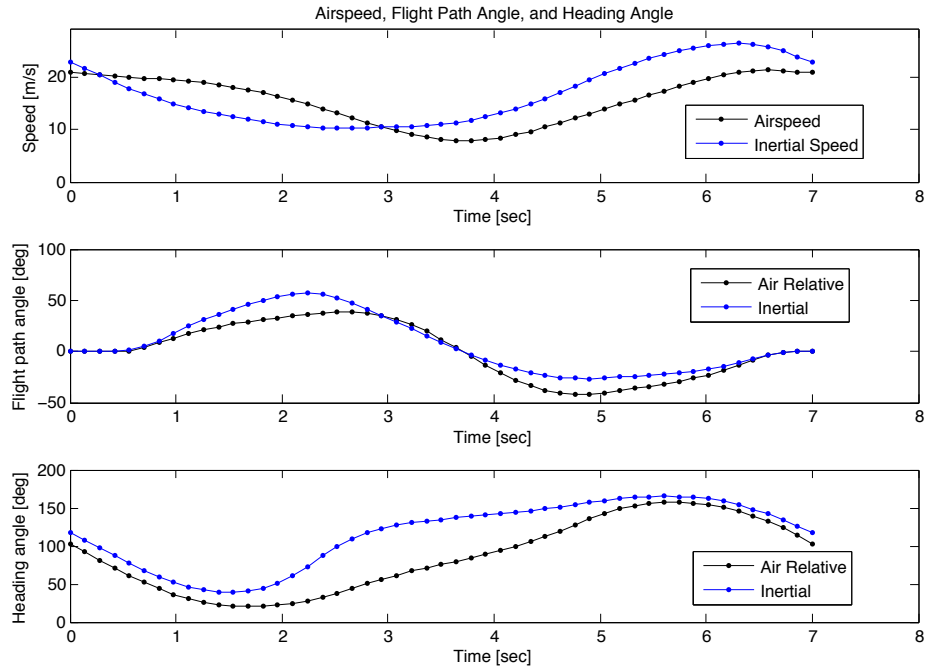


Figure 2.13: Speeds, flight path angles, and heading angles for the minimum reference wind speed trajectory for the model Wandering Albatross flying through a log boundary layer.

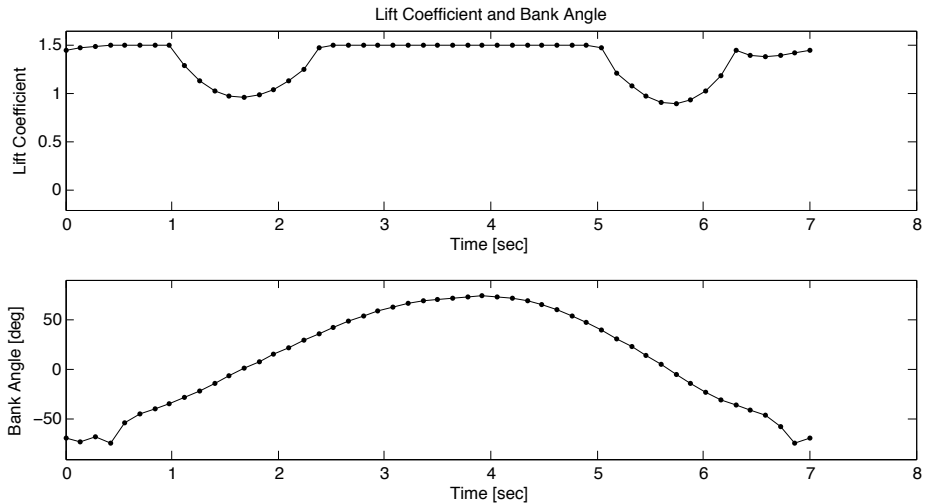


Figure 2.14: Lift coefficient and bank angle for the minimum reference wind speed trajectory for the model Wandering Albatross flying through a log boundary layer.

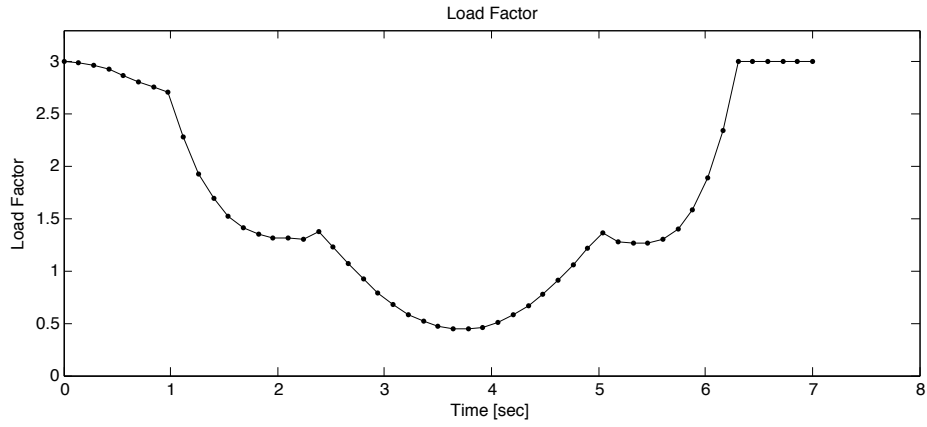


Figure 2.15: Load factor for the minimum reference wind speed trajectory for the model Wandering Albatross flying through a log boundary layer.

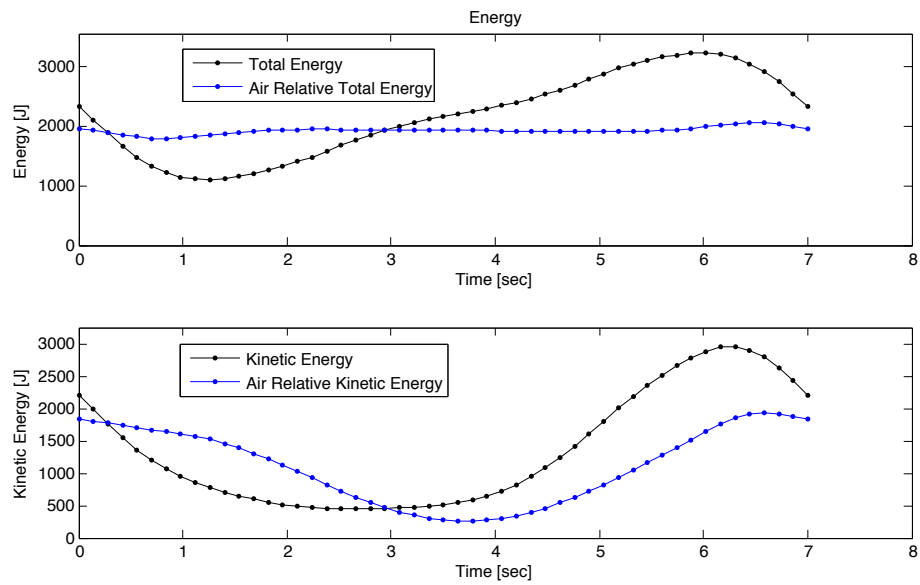


Figure 2.16: Total energy, air relative total energy, kinetic energy and air relative kinetic energy for the minimum reference wind speed trajectory for the model Wandering Albatross flying through a log boundary layer.

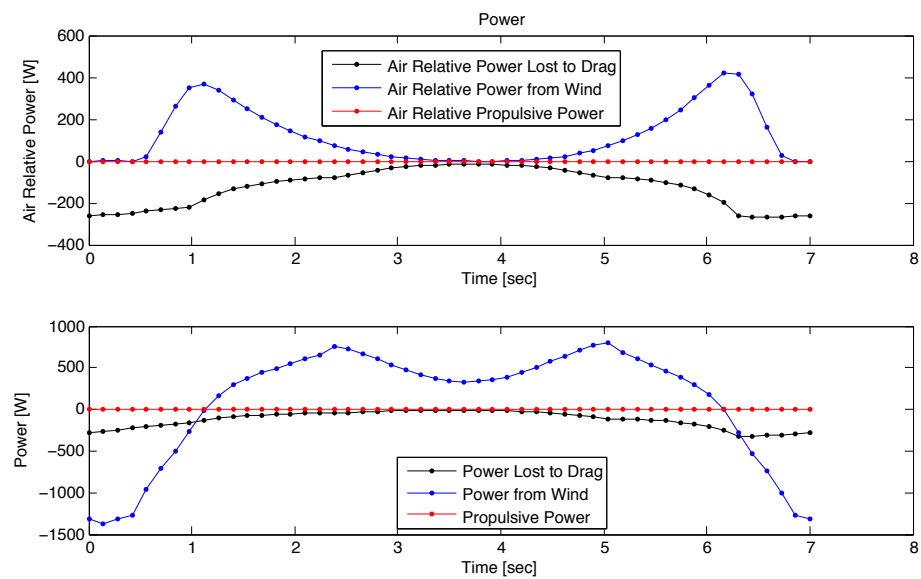


Figure 2.17: Power and air relative power due to propulsion, drag, and the wind for the minimum reference wind speed trajectory for the model Wandering Albatross flying through a log boundary layer.

Chapter 3

Trajectory Optimization Results

From the energy analysis of the equations of motion and the validation results, the primary characteristics of an unpowered dynamic soaring trajectory have become clear. In general, the aircraft or bird should turn from upwind to downwind where the wind speed is greatest and it should turn from downwind to upwind where the wind speed is lowest. Additionally, it should climb into an increasing headwind and dive through a decreasing tailwind. The optimal trajectories are expected to have these general characteristics while satisfying the constraints imposed for a given problem.

This chapter presents trajectory optimization results for dynamic soaring problems that increase in complexity. First, minimum required wind speed trajectories are found for flight through a linear boundary layer. Then, both minimum required wind speed and maximum net speed trajectories are found for flight in a log boundary layer. In the following section, a solution for flight through the wind-wave boundary layer is generated. The final section presents results that also consider the onboard electrical energy. Equation 2.11 is added to the equations of motion and trajectories are found for flight through a log boundary layer with constraints on battery energy charge/discharge rate.

3.1 Linear Boundary Layer

The model albatross parameters were used again to find the minimum required linear boundary layer strength and the corresponding optimal trajectory through it. All of the constraints were the same as in the validation problem, only the boundary layer shape was changed. Figures 3.1 to 3.6 show the minimum wind gradient trajectory, details of the state and control variables, and the energy state throughout the cycle. In this case, the optimal cycle occurs for a wind gradient of 0.1806 s^{-1} . The optimal cycle time is 10.51 seconds and computation time required to find the solution was 1.78 seconds. Note that the maximum altitude in this case is much higher than for the log boundary layer in the validation case ($\approx 50 \text{ m}$ vs. $\approx 20 \text{ m}$). In addition, the maximum airspeed and the overall variation in airspeed throughout the maneuver are greater than for the log boundary layer. Again the vehicle reaches both its maximum load factor and lift coefficient constraints. The general trends with regard to the total energy and air relative total energy follow those of the validation problem.

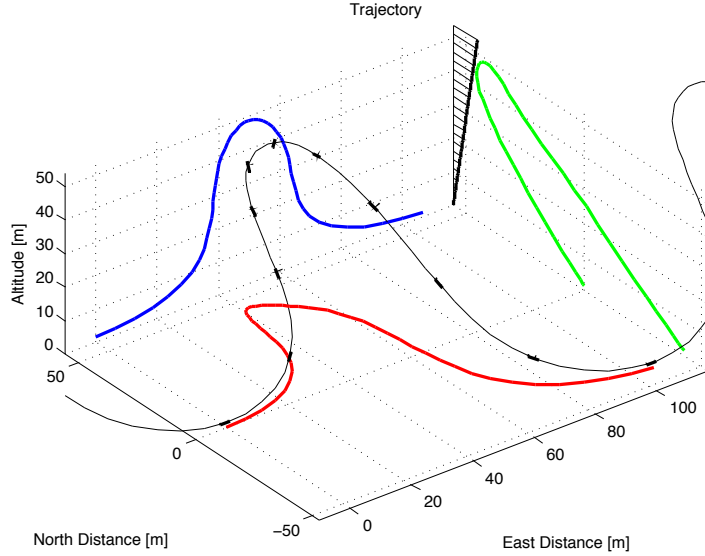


Figure 3.1: Trajectory for minimum wind gradient (0.1806 s^{-1}) for the model Wandering Albatross flying through a linear boundary layer. The boundary layer profile shown at the top of the plot indicates how far the wind travels in the time between successive instances of the vehicle along the trajectory. The colored lines show projections of the trajectory.

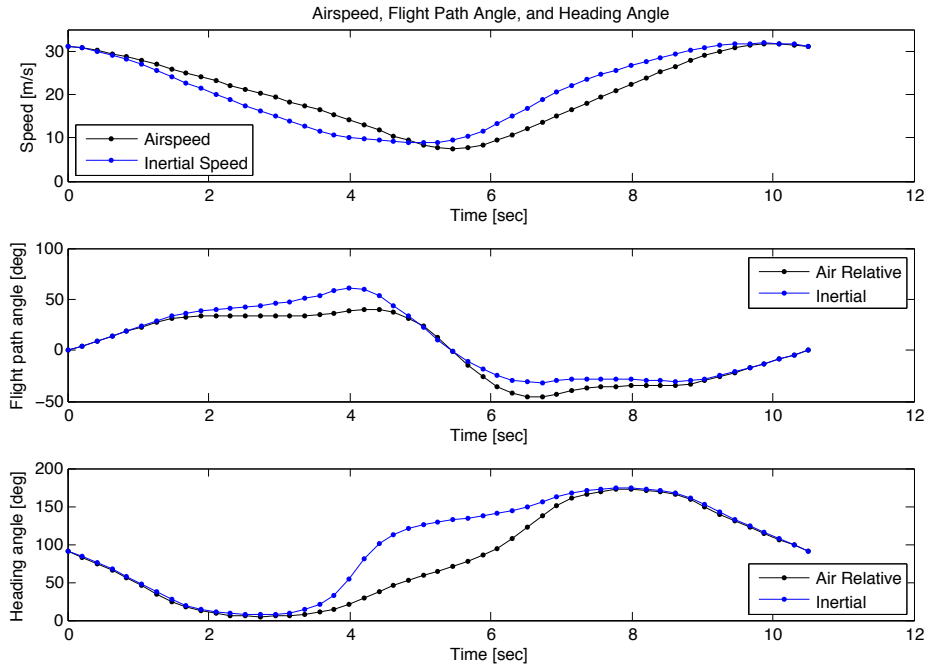


Figure 3.2: Speeds, flight path angles, and heading angles for the minimum wind gradient trajectory for the model Wandering Albatross flying through a linear boundary layer.

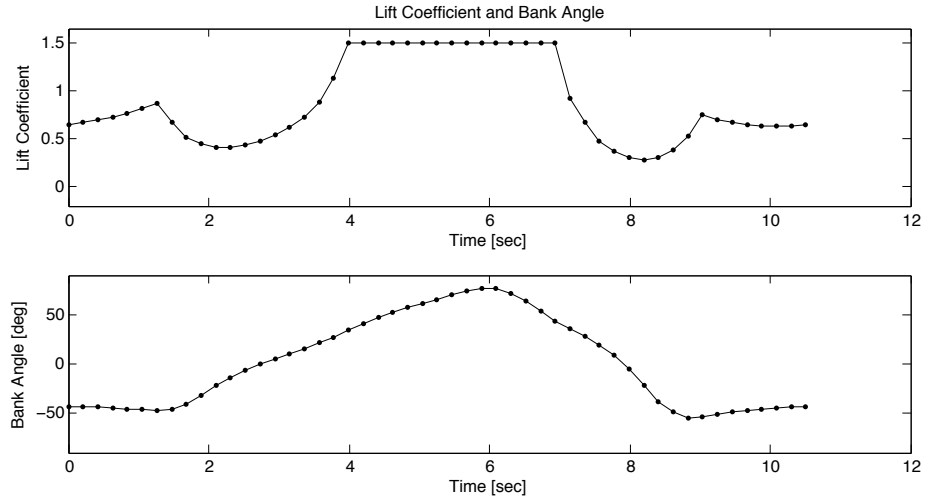


Figure 3.3: Lift coefficient and bank angle for the minimum wind gradient trajectory for the model Wandering Albatross flying through a linear boundary layer.

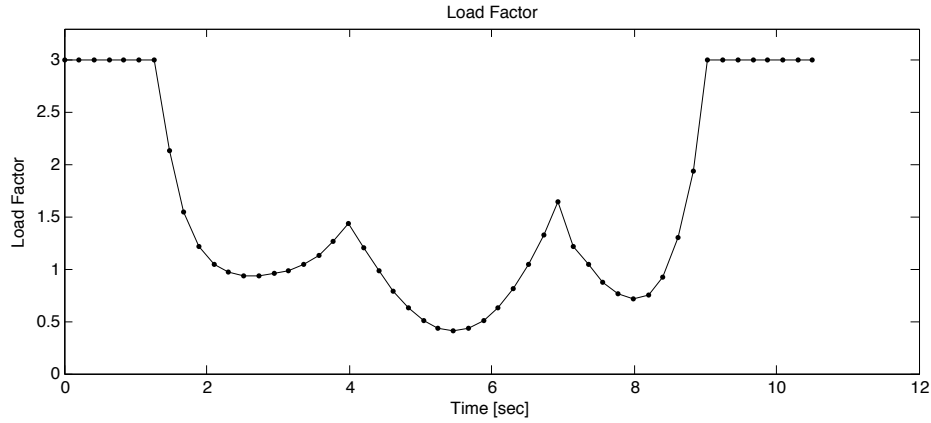


Figure 3.4: Load factor for the minimum wind gradient trajectory for the model Wandering Albatross flying through a linear boundary layer.

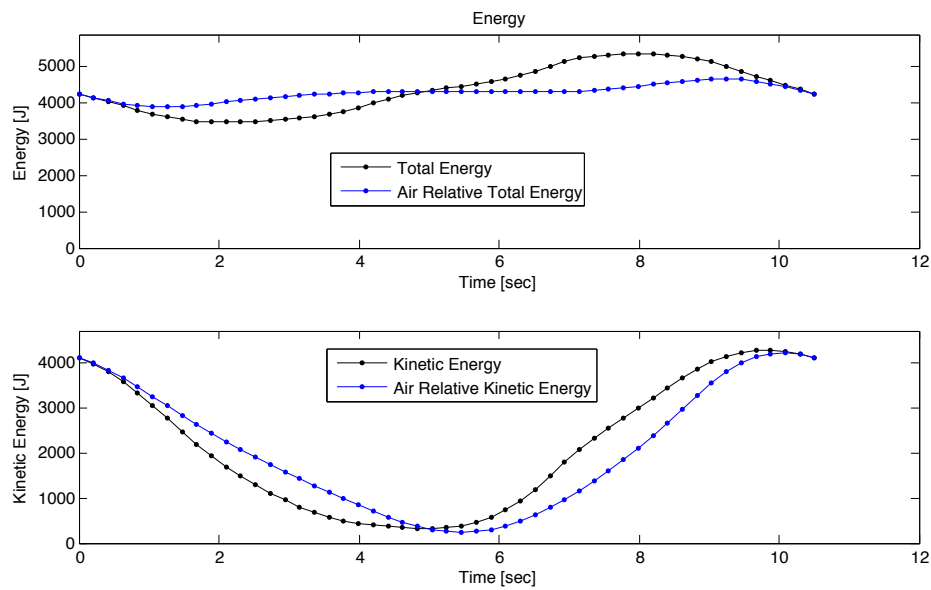


Figure 3.5: Total energy, air relative total energy, kinetic energy and air relative kinetic energy for the minimum wind gradient trajectory for the model Wandering Albatross flying through a linear boundary layer.

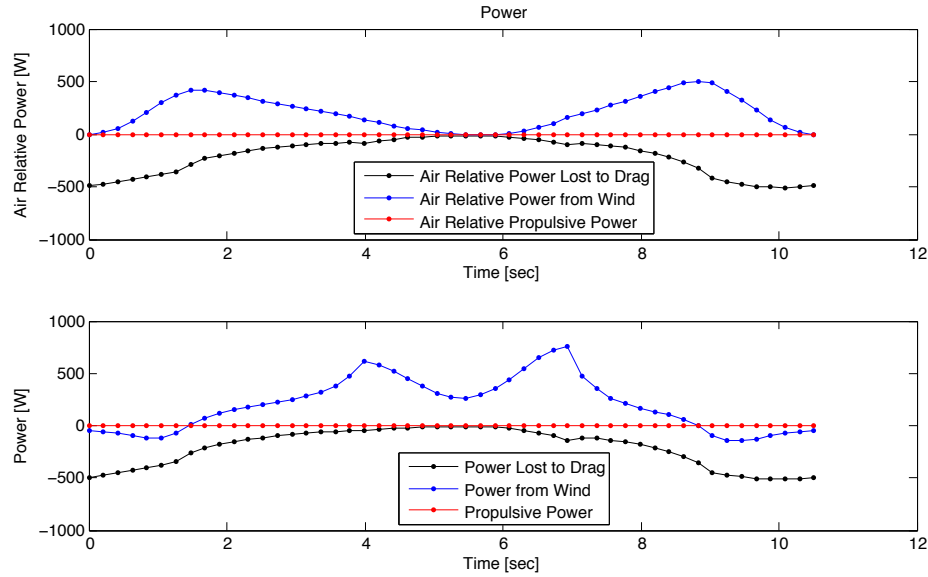


Figure 3.6: Power and air relative power due to propulsion, drag, and the wind for the minimum wind gradient trajectory for the model Wandering Albatross flying through a linear boundary layer.

Next, a constraint was introduced on the heading direction and a series of optimizations were run to generate a minimum reference wind speed polar. This polar for the linear boundary layer is shown in Fig. 3.7, where the distance from the origin indicates the minimum required wind gradient strength and the angle indicates the trajectory's net travel direction with respect to the wind. The solution for the minimum required wind speed without a direction constraint is used as an initial condition for the first direction constrained optimization. The net travel direction is then stepped in 0.5 degree increments, using the previous solution as the initial condition for the next run. Overall, it took about 12 minutes to generate this minimum wind speed polar and required 451 separate trajectory optimizations.

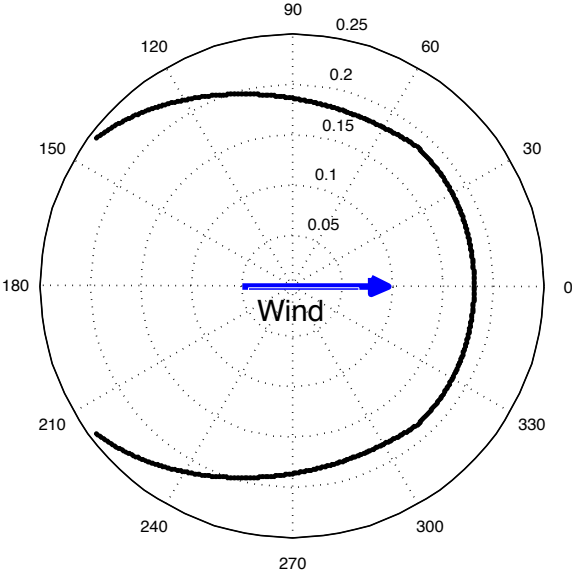


Figure 3.7: Polar plot of the minimum linear wind gradient in $[s^{-1}]$ required to fly in each direction with respect to the wind for the model Wandering Albatross.

There are a couple of important items to note about this figure. The first is that the model albatross can only fly in a linear boundary layer up about 142 degrees off the wind direction, and as this angle is approached, the required wind speed increases substantially. This will be the case for many vehicles, where they are unable to fly in every direction with respect to the wind. In general, as the aerodynamic performance of a vehicle improves, the extents of the directions in which they can fly neutral energy cycles will increase.

The second item of interest is the slight kink in the polar around 47 degrees off of the wind direction. Here the minimum wind speed trajectory changes character. The general character can be seen in Fig. 3.8 where in the net downwind trajectory shows two climbs into the wind to get back to the initial conditions. The rest of the trajectories up to 47 degrees off the wind look very similar to this one. The other trajectories all have the same general character as the minimum reference wind speed trajectory without a net travel direction constraint. Figure 3.9 shows the variation in the optimal cycle times for each of the trajectories on the polar, with roughly a factor of two change in the cycle time near the phase transition at 47 degrees.

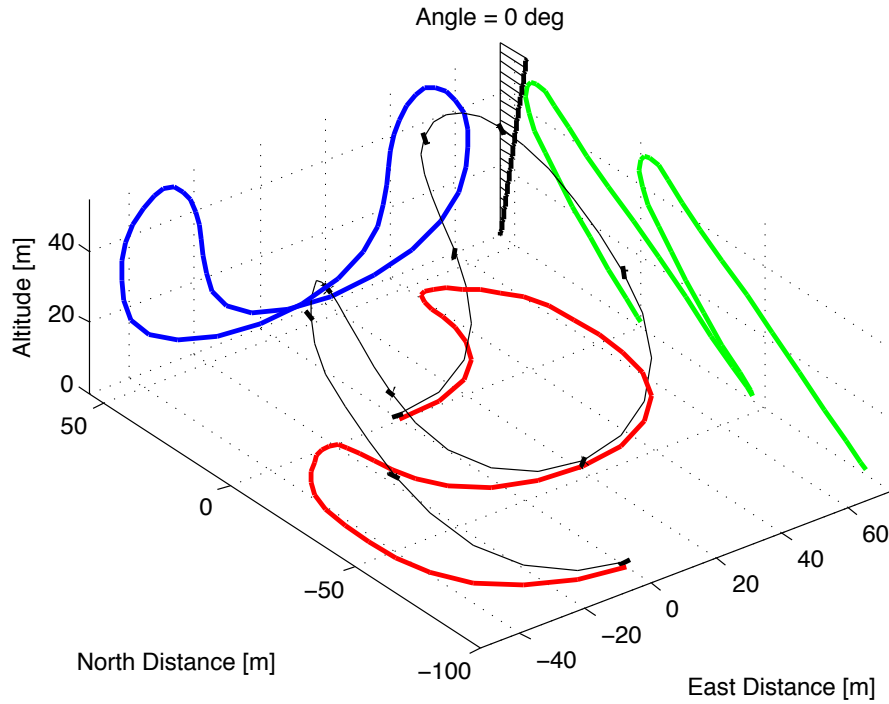


Figure 3.8: Downwind trajectory from the minimum required wind gradient polar for the model Wandering Albatross.

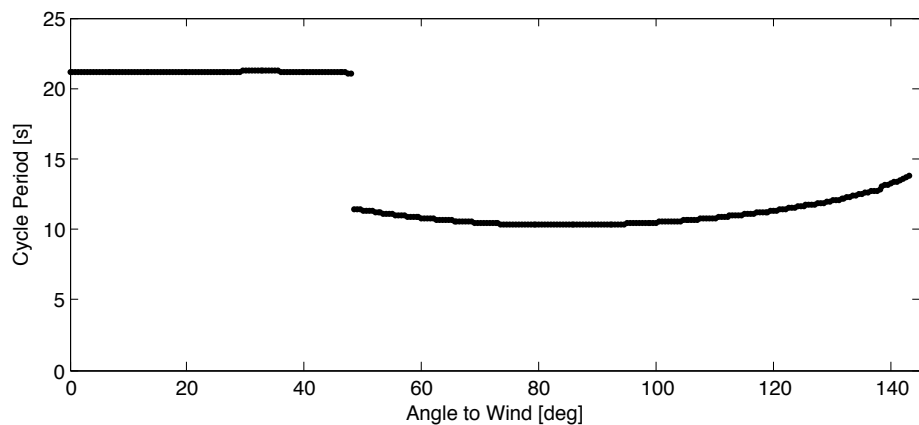


Figure 3.9: Variation in optimal cycle time as a function of the angle flown with respect to the wind from the minimum required wind gradient polar.

3.2 Log Boundary Layer - Minimum Reference Wind Speed

Next, the polar depicting the minimum required wind speed to fly in each direction was generated for the model Wandering Albatross flying in a log boundary layer (Fig. 3.10). The unconstrained minimum wind speed validation case was used as the initial trajectory to generate this polar. Some of the corresponding trajectories are shown in Fig. 3.11 and cycle times in Fig. 3.12. Again we see that the model Wandering Albatross is not capable of making progress in every direction with respect to the wind. In this case, the maximum angle is approximately 86 degrees. Additionally, there is a phase changes that occurs at an angle of about 25 degrees. This can be easily been seen in Fig. 3.11 where 0 degree case shows a two climb trajectory and the other three have a character similar to the unconstrained minimum wind speed case.

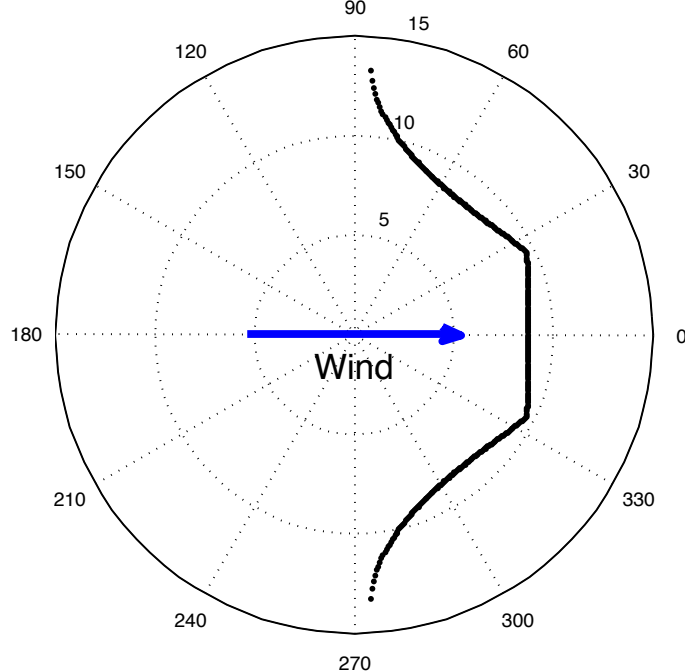


Figure 3.10: Polar plot of the minimum wind speed required to fly in each direction with respect to the wind for the model Wandering Albatross in a log boundary layer.

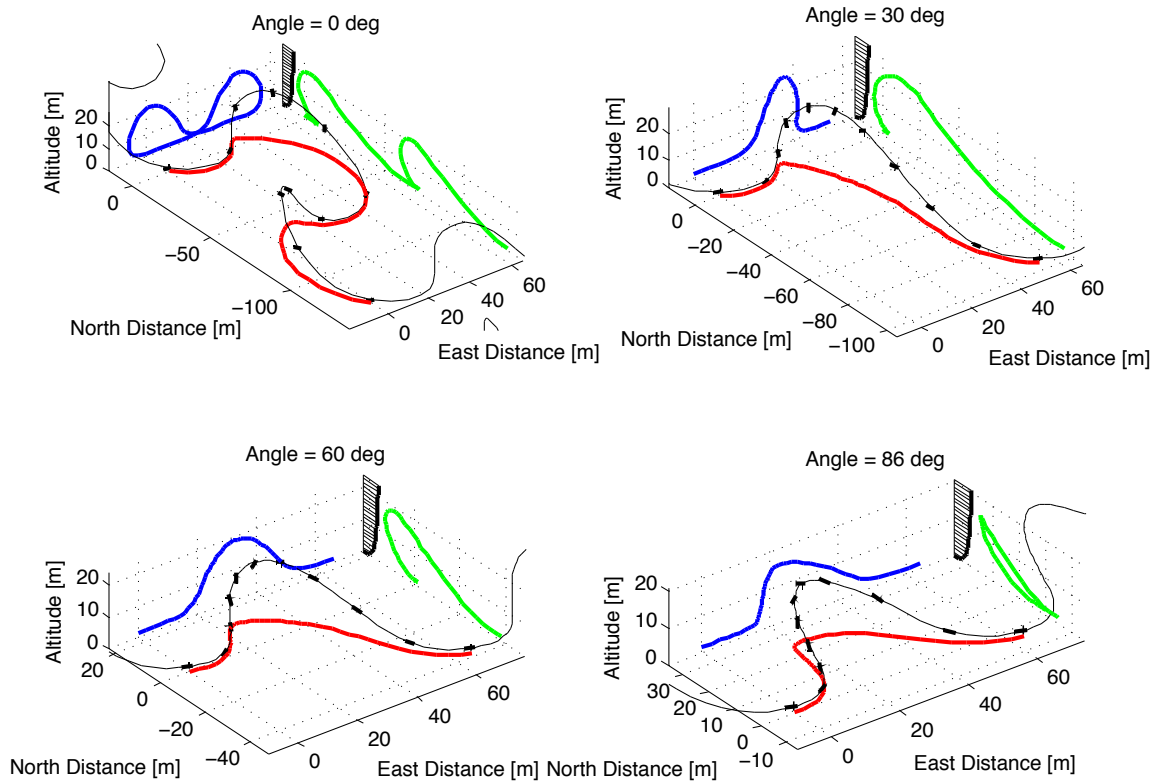


Figure 3.11: Four trajectories selected from the minimum required wind speed polar for the model albatross in a log boundary layer.

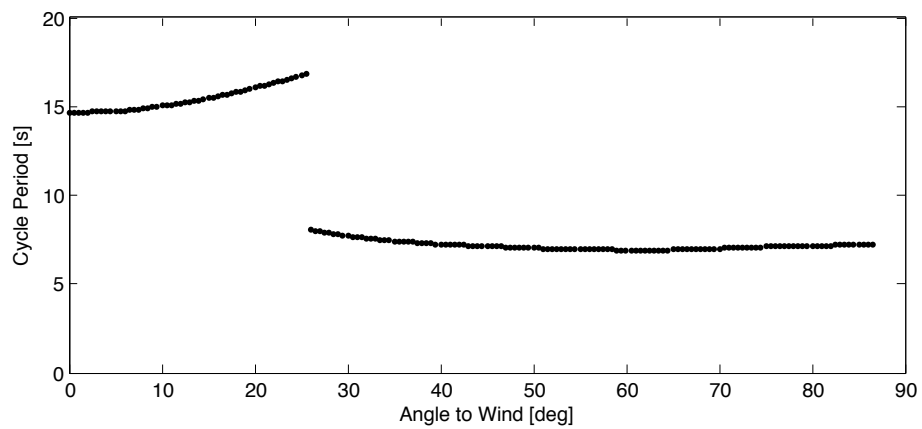


Figure 3.12: Variation in optimal cycle time as a function of the angle flown with respect to the wind for the minimum required wind speed polar in a log boundary layer.

3.3 Log Boundary Layer - Maximum Net Speed

In this section, the performance polar idea is taken one step further. The objective is switched to maximizing the net speed over the trajectory, while maintaining the net flight direction constraint. The wind speed is fixed at a specific value, which might, for instance, represent the current measured reference wind speed. For the polar plot, the distance from the origin now indicates how fast the vehicle will move over the long term and the direction indicates the net travel direction. For example, the polar shown in Fig. 3.13 shows the maximum net speed the model Wandering Albatross is able to fly in each direction given that the reference wind speed is 12 m/s for a log boundary layer. This polar was generated by a sequence of trajectory optimizations that started with the initial condition of the unconstrained minimum wind speed case. The wind speed was then incremented to 12 m/s and then the flight direction constraint was varied in 1 degree increments.

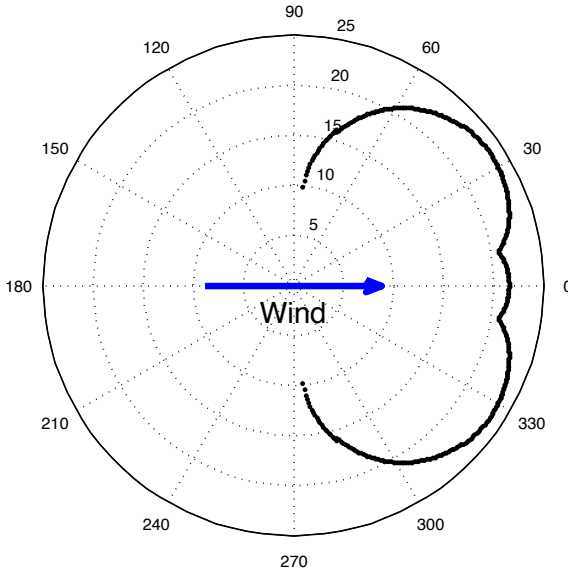


Figure 3.13: Net speed polar for the model Wandering Albatross in a log boundary layer with a 12 m/s reference wind speed.

It is obvious from this plot that the vehicle is unable to fly at an angle greater than about 84 degrees with respect to the wind for the 12 m/s wind speed. As this angle is approached the net speed tends quickly towards zero. It is also interesting

to note that the maximum speed occurs for flight roughly 35 degrees off of the wind. The phase change is also evident in this plot, but occurs for a smaller angle, around 10 degrees. This is because in many cases the two climb trajectories take longer to fly, so while the minimum required speed may be lower, the net speed may not be as great as for a single climb trajectories. The optimum cycle times are for the maximum net speed polar are shown in Fig. 3.14. Four of the resulting trajectories are shown in Fig. 3.15. It is also worth noting that the net speed and the overall distance travelled in these trajectories is greater than the minimum wind speed trajectories.

By aggregating the maximum net speed polars for different wind conditions an overall performance polar for a dynamic soaring vehicle can be generated. The usefulness of this type of performance polar will be shown in Chapter 4, where it is used in the context of planning long range missions.

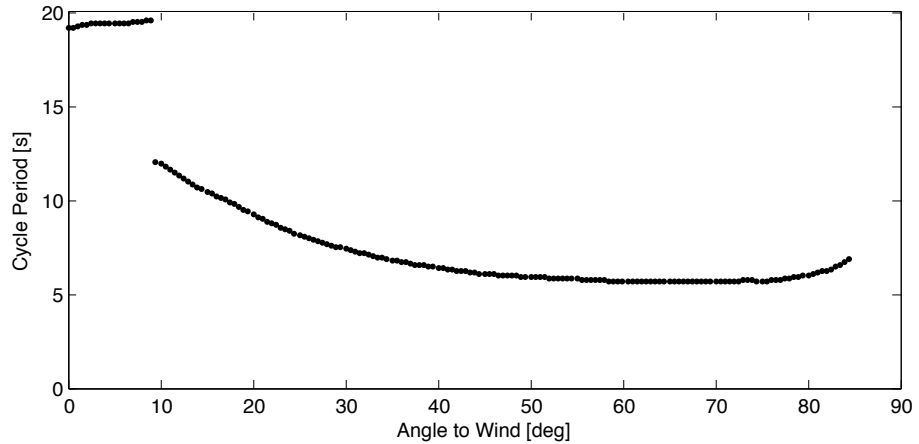


Figure 3.14: Variation in optimal cycle time as a function of the angle flown with respect to the wind for the maximum net speed polar in a log boundary layer with 12 m/s reference wind speed.

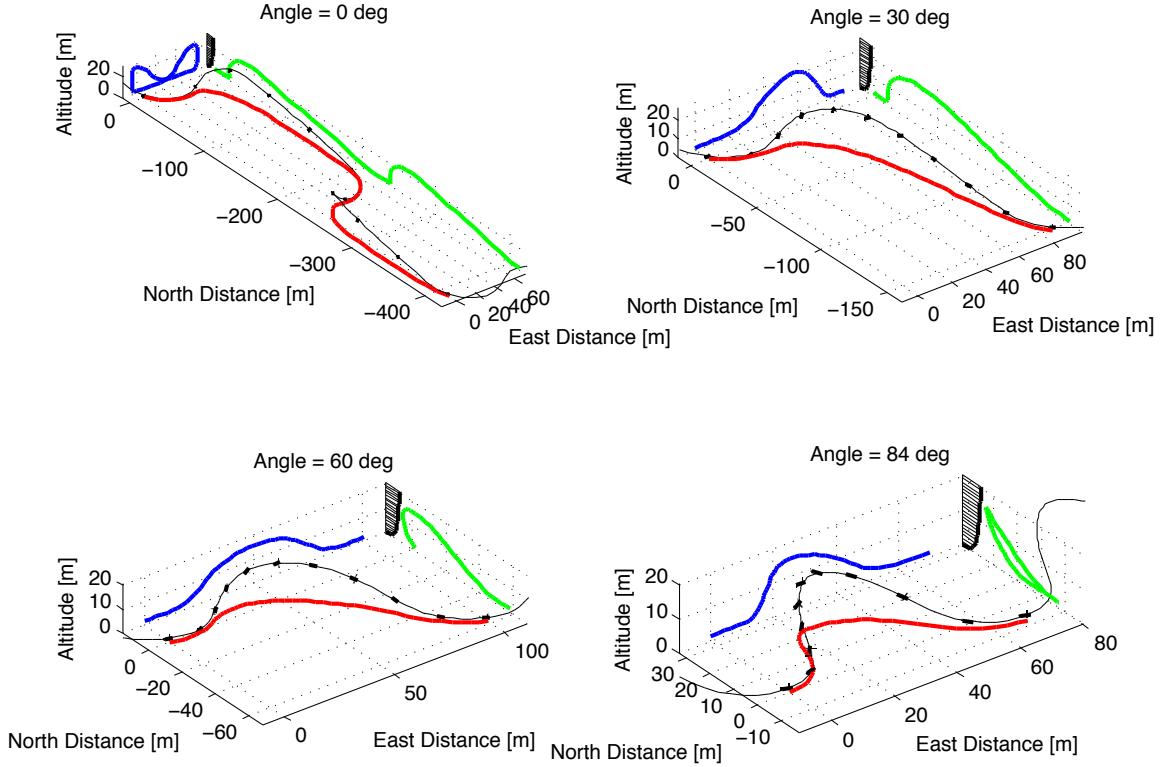


Figure 3.15: Four trajectories selected from the maximum net speed polar for the model Wandering Albatross in a log boundary layer with 12 m/s reference wind speed.

3.4 Ocean Boundary Layer with Waves

In this section, the reference wind speed for the model Wandering Albatross flying through the wind-wave boundary layer is minimized. The variable that controls the wave amplitude, wave period, and reference wind speed, as described in Section 2.1.6, is the friction velocity, u^* . It is used as the objective directly instead of the reference wind speed. Two cases are examined in detail. The first is the optimal periodic trajectory where the vehicle starts and finishes at the same phase along the same wave. In the second case, the vehicle is forced to fly from one wave to the next upwind, but is still required to start and finish the trajectory at the same wave phase angle. By starting and finishing at the same wave phase angle the solutions are

periodic.

For the second case, 101 collocation points were used to maintain a reasonable temporal resolution since the optimal cycle times turned out to be longer than in previous studies. Some additional constraints were also applied. The first was the addition of the aforementioned wave phase angle constraint, given by Eq. 3.1, where n_{peaks} is the number of waves from the initial one that the vehicle must traverse. n_{peaks} must be an integer and the sign convention is that positive values indicate transferring to waves further downstream and negative values to upstream ($n_{peaks} = 0$ and -1 for the two cases).

$$0 = x_{final} - x_0 - \lambda_{peak}(n_{peaks} + t_{cycle} * f_{peak}) \quad (3.1)$$

Additionally, the minimum wingtip height constraint was activated requiring each wingtip and the center of gravity to be at least 0.05 m above the water surface throughout the trajectory. Control rate constraints were also imposed on both C_L (2.0 s^{-1}) and ϕ ($180^\circ/\text{s}$).

SNOPT had a tough time generating feasible trajectories that met the wave phase angle constraints from the baseline initial conditions. Similar to the procedure used to generate the performance polars, a series of optimizations were performed building up to the desired result. First, the wave phase angle constraint was gradually tightened with the wave amplitude set to zero. Once the wave phase angle constraint was exactly satisfied the wave amplitude was slowly increased. The minimum u^* value for a run was used to calculate the actual wave amplitude that would be generated by such a wind according to Eq. 2.27. At some point, the calculated wave amplitude will equal the run wave amplitude. If the wave period, given by Eq. 2.26 also matches, then a consistent wind-wave field is achieved and the resulting trajectory is locally optimal. There are no guarantees that the globally optimal solution will be found with this method, but the resulting trajectories exhibit many of the expected characteristics and look very reasonable.

3.4.1 Start and End on the Same Wave

For $n_{peaks} = 0$, one expected result was for the bird to fly at constant altitude along the lee side of the wave near the surface where the vertical wind velocity is maximized. For the model albatross the minimum sink rate is 0.596 m/s at an airspeed of 11.82 m/s. The required u^* to achieve a vertical wind speed of 0.596 m/s at an altitude of 0.05 m is 0.817 m/s. By flying dynamic soaring trajectories similar to the cases without waves, the minimum u^* value may be significantly reduced compared to this value.

Details of the minimum u^* trajectory with $n_{peaks} = 0$ are shown in Figs. 3.16 to 3.23. Note, that the trajectory is similar to the cases without waves, it is just shown from a different perspective and the initial point is at the maximum altitude instead of the minimum. At the optimum, $u^* = 0.539$ m/s, where the corresponding wave amplitude is 1.11 m, the wave period is 8.9 sec, and the reference wind speed at 10 meters altitude is 11.28 m/s. It is difficult to compare this result to the validation case as the h_0 values vary with the reference wind speed for this boundary layer model. At the optimum, $h_0 = 0.0023$ m in this case compared to $h_0 = 0.03$ m in the validation case. For smaller values of h_0 the boundary layer shape is “fuller” requiring a higher reference wind speed or greater altitude traversal to get the same difference between the minimum wind speed and maximum wind speed seen by the vehicle. As expected, by taking advantage of the vertical wind induced by the waves, the minimum u^* value of 0.539 m/s (11.28 m/s wind speed at 10 m) is less than if there was no wave amplitude where $u^* = 0.598$ m/s (12.20 m/s wind speed at 10 m). Note that, for the comparison case with no wave amplitude, the wave phase angle constraint is still enforced.

From Figs. 3.22 and 3.23 it is clear that the vehicle always benefits from vertical winds induced by the waves as the whole trajectory is flown over the part of the wave where there is a positive vertical velocity. The optimum cycle period is 5.81 seconds and the bank angle and load factor constraints are not active at any point throughout the trajectory. The maximum C_L constraint is active for much of the trajectory.

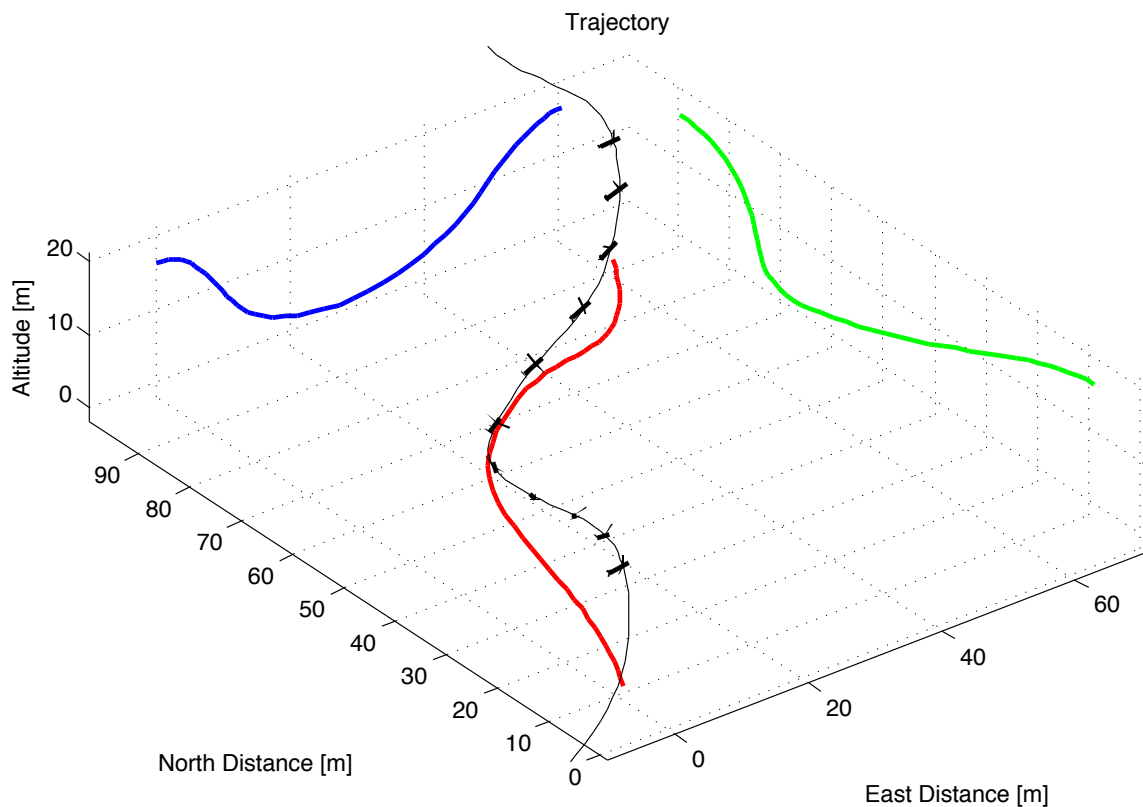


Figure 3.16: Minimum u^* ($= 0.539 \text{ m/s}$) trajectory for the model Wandering Albatross flying through the wind-wave boundary layer, starting and finishing on the same wave. The wave amplitude is 1.11 m , the wave period is 8.9 sec , and the reference wind speed at 10 m is 11.28 m/s . The wind and the waves are both moving to the North.

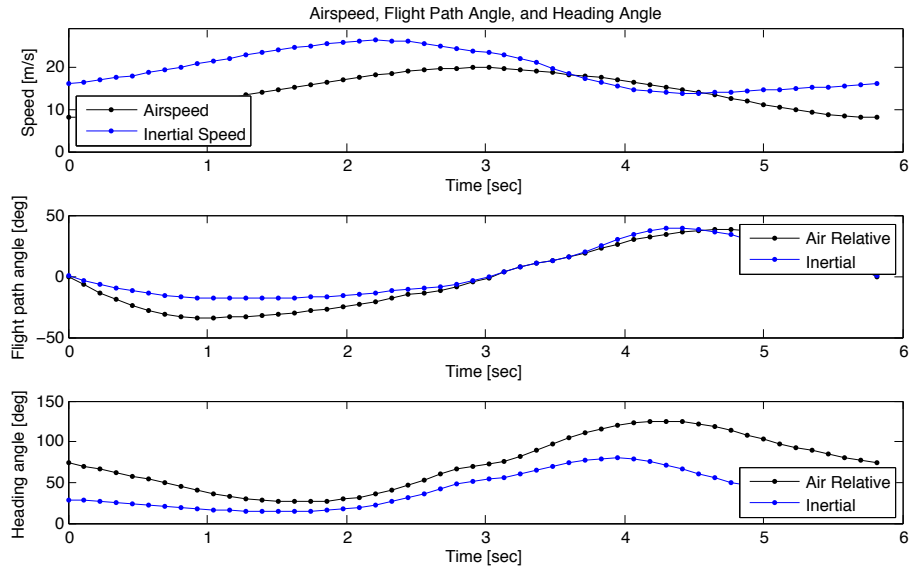


Figure 3.17: Speeds, flight path angles, and heading angles for the minimum u^* ($= 0.539 \text{ m/s}$) trajectory for the model Wandering Albatross flying through the wind-wave boundary layer, starting and finishing on the same wave.

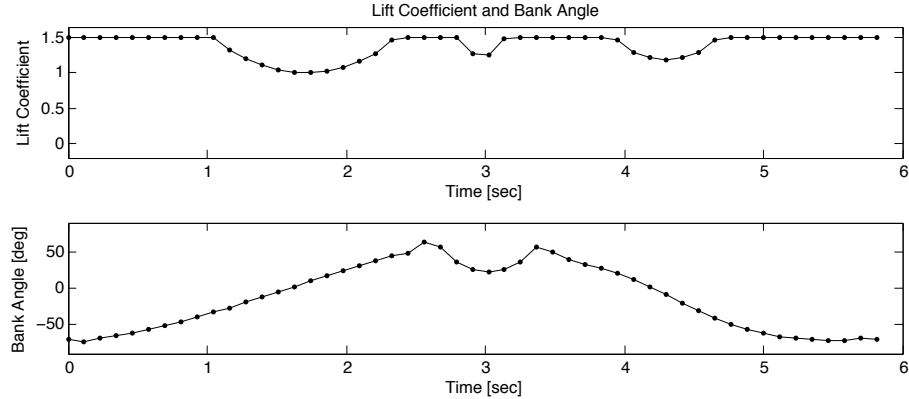


Figure 3.18: Lift coefficient and bank angle for the minimum u^* ($= 0.539 \text{ m/s}$) trajectory for the model Wandering Albatross flying through the wind-wave boundary layer, starting and finishing on the same wave.

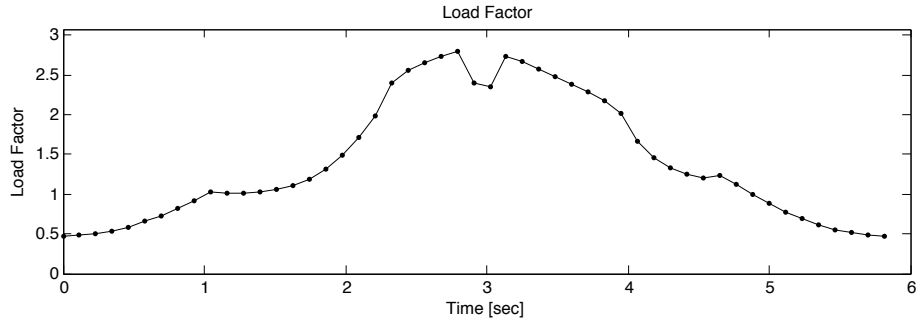


Figure 3.19: Load factor for the minimum u^* ($= 0.539 \text{ m/s}$) trajectory for the model Wandering Albatross flying through the wind-wave boundary layer, starting and finishing on the same wave.

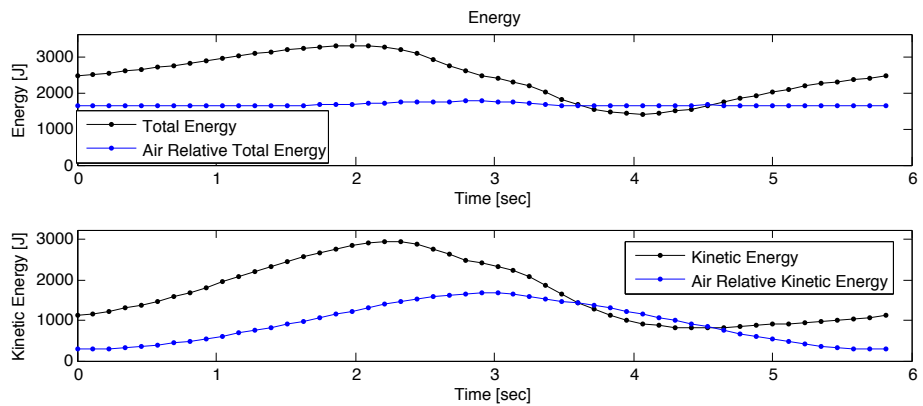


Figure 3.20: Total energy, air relative total energy, kinetic energy and air relative kinetic energy for the minimum u^* ($= 0.539 \text{ m/s}$) trajectory for the model Wandering Albatross flying through the wind-wave boundary layer, starting and finishing on the same wave.

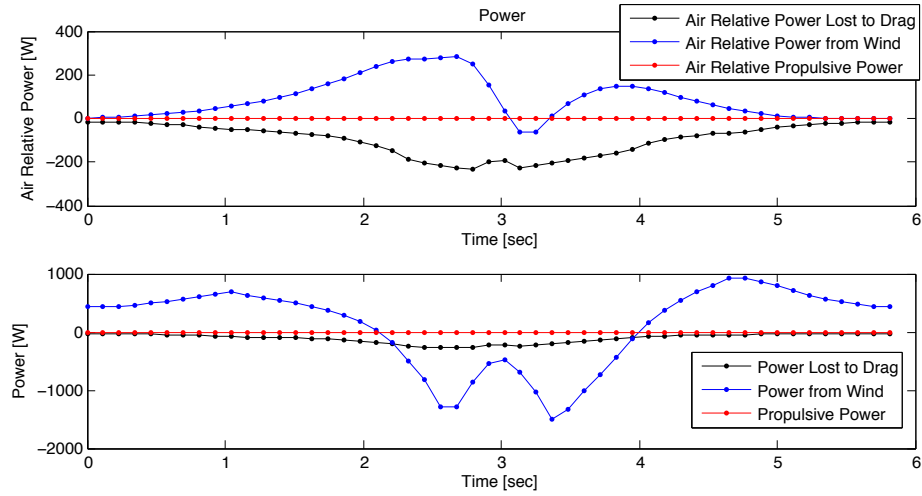


Figure 3.21: Power and air relative power due to propulsion, drag, and the wind for the minimum u^* ($= 0.539 \text{ m/s}$) trajectory for the model Wandering Albatross flying through the wind-wave boundary layer, starting and finishing on the same wave.

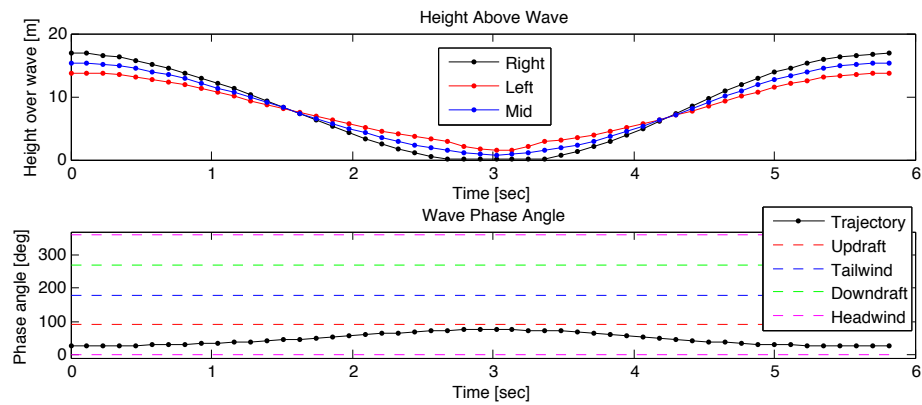


Figure 3.22: Wave phase angle of the center of gravity and the right, left, and midspan heights above the wave surface for the minimum u^* ($= 0.539 \text{ m/s}$) trajectory for the model Wandering Albatross flying through the wind-wave boundary layer, starting and finishing on the same wave.

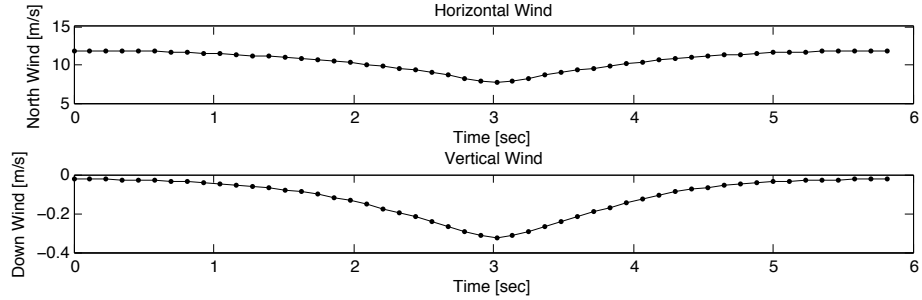


Figure 3.23: North and down winds at the center of gravity for the minimum u^* ($= 0.539$ m/s) trajectory for the model Wandering Albatross flying through the wind-wave boundary layer, starting and finishing on the same wave.

3.4.2 Transfer One Wave Upstream

The next set of results are for $n_{peaks} = -1$, requiring a transfer from one wave to the next one upstream. In this case, there are a number of effects we expect to see. First, so that the vehicle does not have to fly too far upwind, the cycle time should be longer so that the upstream wave has a chance to propagate downstream relative to the vehicle's initial position. In addition, it is expected that the vehicle will fly in the region with a strong vertical velocity when it is near the surface, and transition between the waves at higher altitudes where the downward velocity is weaker.

Figures 3.24 to 3.31 show details of the resulting optimal trajectory where $u^* = 0.806$ m/s. The corresponding wave amplitude is 2.02 m, the wave period is 12.1 seconds, and the corresponding reference wind speed at 10 meters is 15.23 m/s. The optimal cycle period is significantly longer than the first case at 17.1 seconds, likely to let the wave propagate far enough downstream so that the vehicle does not have to move upwind. This case is even more difficult to compare to the validation case as the wave phase angle constraint severely limits the direction that the vehicle can fly in. Again, by comparing the optimum result to the case where the same constraints are imposed, but there is no wave amplitude, the effect of the waves becomes apparent. With no wave amplitude the optimum $u^* = 0.872$ m/s (16.14 m/s wind speed at 10 m), compared to $u^* = 0.806$ m/s (15.23 m/s wind speed at 10 m) with the proper wave amplitude. This result and the previous result indicate that waves have the

potential to reduce the required reference wind speed by about 10 %.

Overall, the resulting trajectory looks reasonable and has the expected characteristics. Further observations of albatross will need to be conducted to verify that they take advantage of the waves in the manner shown here or whether they are taking advantage of other wind energy transfer mechanisms, such as gusts as proposed by Pennycuick [34]. It is hoped that the trackers described in Section 6.1 will aid in these studies. Additional effects not modeled here, such as the stochastic nature of the atmosphere and the sea surface, non-alignment of the wind and the waves, etc., will clearly have an effect on the optimal trajectories. From these results we see that the required wind speed to dynamic soar can be reduced if the waves are taken advantage of, however, the reduction is relatively small. For the aircraft design studies conducted in Chapter 5 the effects of the waves on the wind field will be ignored and the basic log boundary layer profile will be used.

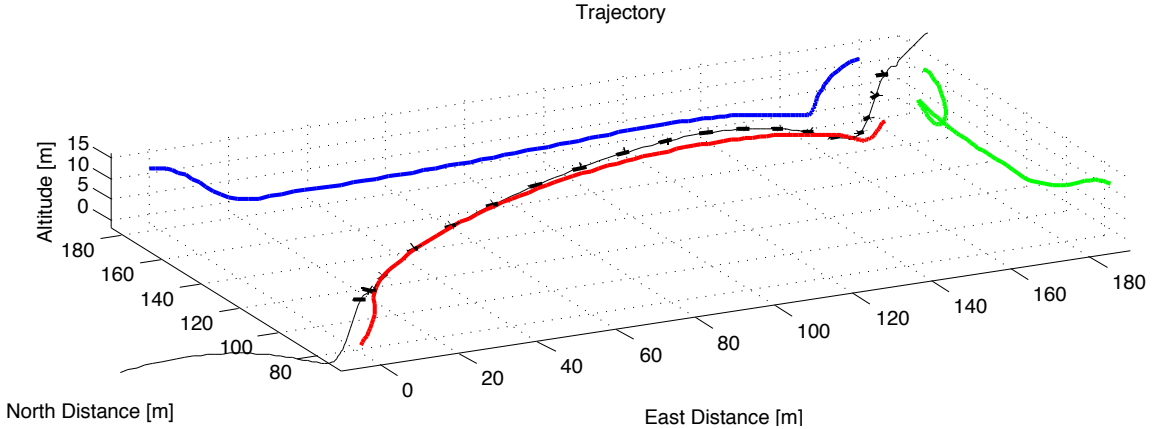


Figure 3.24: Minimum u^* ($= 0.806 \text{ m/s}$) trajectory for the model Wandering Albatross flying through the wind-wave boundary layer, transferring one wave upstream ($n_{\text{peaks}} = -1$). The wave amplitude is 2.02 m, the wave period is 17.1 sec, and the reference wind speed at 10 m is 15.23 m/s. The wind and the waves are both moving to the North.

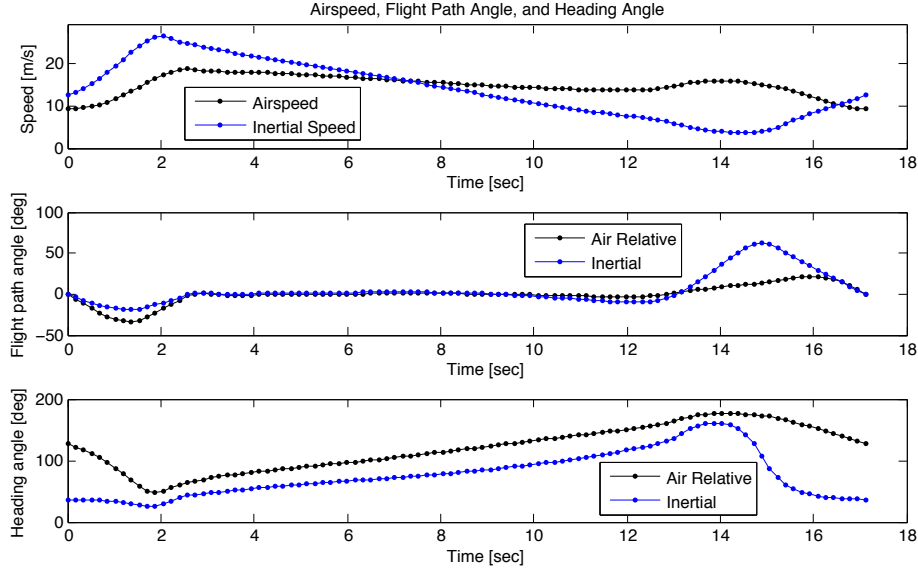


Figure 3.25: Speeds, flight path angles, and heading angles the minimum u^* ($= 0.806$ m/s) trajectory for the model Wandering Albatross flying through the wind-wave boundary layer, transferring one wave upstream ($n_{peaks} = -1$).

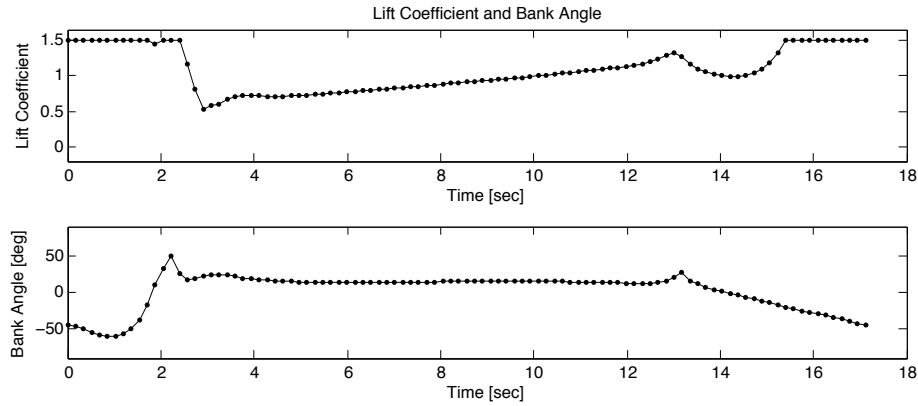


Figure 3.26: Lift coefficient and bank angle for the minimum u^* ($= 0.806$ m/s) trajectory for the model Wandering Albatross flying through the wind-wave boundary layer, transferring one wave upstream ($n_{peaks} = -1$).

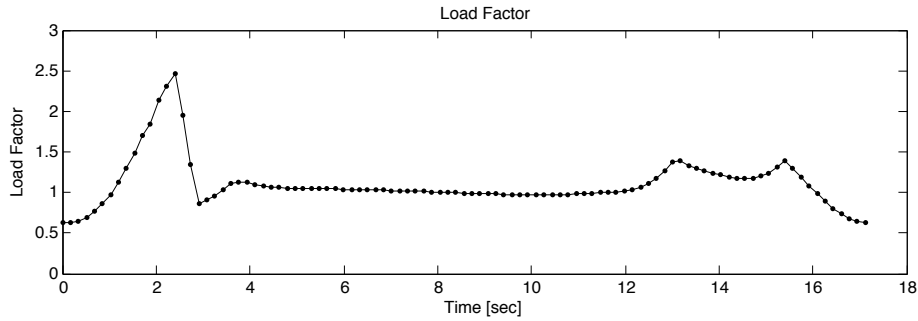


Figure 3.27: Load factor for the minimum u^* ($= 0.806 \text{ m/s}$) trajectory for the model Wandering Albatross flying through the wind-wave boundary layer, transferring one wave upstream ($n_{\text{peaks}} = -1$).

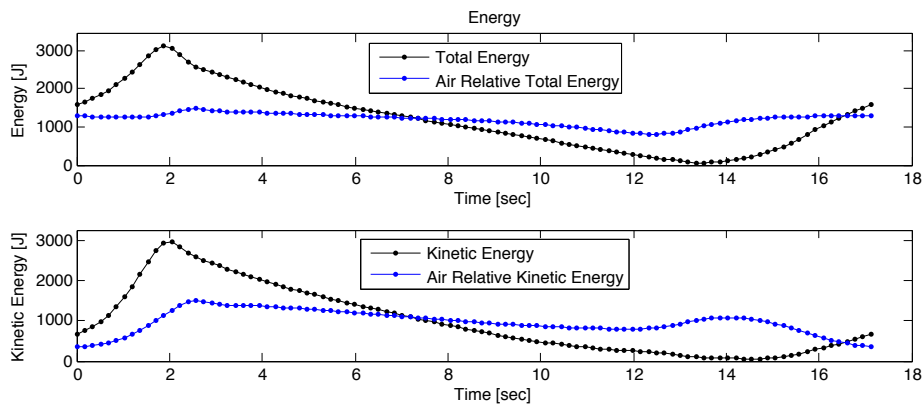


Figure 3.28: Total energy, air relative total energy, kinetic energy and air relative kinetic energy for the minimum u^* ($= 0.806 \text{ m/s}$) trajectory for the model Wandering Albatross flying through the wind-wave boundary layer, transferring one wave upstream ($n_{\text{peaks}} = -1$).

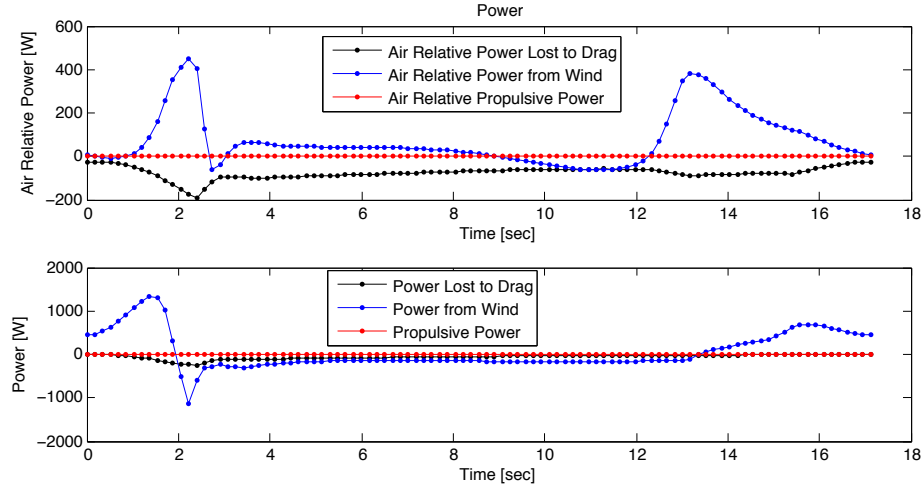


Figure 3.29: Power and air relative power due to propulsion, drag, and the wind for the minimum u^* ($= 0.806 \text{ m/s}$) trajectory for the model Wandering Albatross flying through the wind-wave boundary layer, transferring one wave upstream ($n_{\text{peaks}} = -1$).

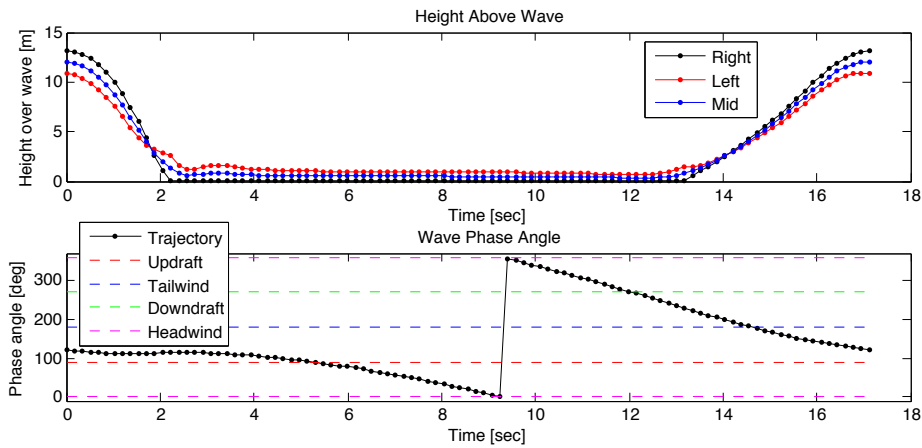


Figure 3.30: Wave phase angle of the center of gravity and the right, left, and midspan heights above the wave surface for the minimum u^* ($= 0.806 \text{ m/s}$) trajectory for the model Wandering Albatross flying through the wind-wave boundary layer, transferring one wave upstream ($n_{\text{peaks}} = -1$).

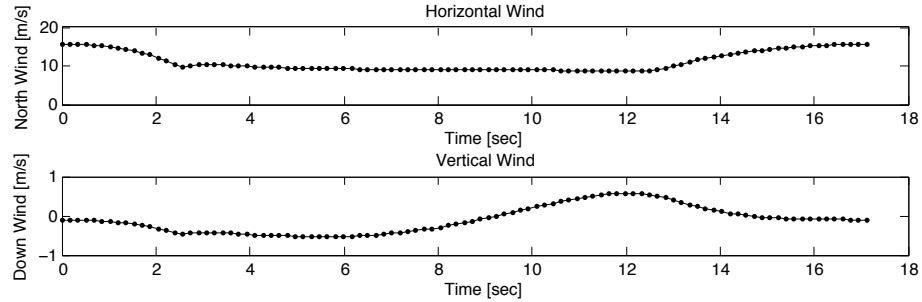


Figure 3.31: North and down winds at the center of gravity for the minimum u^* ($= 0.806 \text{ m/s}$) trajectory for the model Wandering Albatross flying through the wind-wave boundary layer, transferring one wave upstream ($n_{peaks} = -1$).

3.5 Electrical Energy System

The results in this section explore the inclusion of an electrical energy system and its impact on the optimal trajectories . The vehicle model for these studies has the same aerodynamic parameters as the model Wandering Albatross, but adds an electrical power system with a battery, an electric motor/generator, and solar panels. Details of the vehicle that are not given in Table 2.3 are presented in Table 3.1 below. Control rate limits were imposed to prevent instantaneous changes in control variables. The minimum wingtip height above the surface is limited to 0.1 m, and the minimum altitude of the center of gravity is limited to one quarter of the wingspan. The maximum power and rates of change of power were selected to represent modest model airplane propulsion systems for vehicles in the size class of a Wandering Albatross. Other than the propulsion system, no other electrical loads are assumed to exist. The log boundary layer profile is used with $h_0 = 0.03 \text{ m}$ and $h_{ref} = 10 \text{ m}$. Unless otherwise indicated, the solar irradiance is assumed to be 1367 W/m^2 , the clearness index (k_t) is 0.7, and the ground reflectance (ρ_g) is 0.05.

Table 3.1: Vehicle and energy system parameter values.

Parameter	Value	Parameter	Value
C_{L_α}	5.15	$z_{tip_{max}} [m]$	-0.1
C_{D_0}	0.033	$z_{cg_{max}} = -b/4 [m]$	-0.8263
C_{D_2}	0.01894	$P_{max} [W]$	1000
n_{max}	± 3	$P_{gen_{max}} [W]$	1000
$\frac{\partial C_L}{\partial t} [1/sec]$	2	$(\frac{\partial P}{\partial t})_{max} [W/sec]$	250
$\frac{\partial \phi}{\partial t} [^\circ/sec]$	180	$(\frac{\partial P_{gen}}{\partial t})_{max} [W/sec]$	250
η_{sun}	0.0675	k_t	0.7
η_{prop}	0.56	ρ_g	0.05
η_{gen}	0.64	$P_{load} [W]$	0

3.5.1 Minimum Wind Speed Case

Results from three distinct case studies are presented. In the first, the minimum required wind speed is found as a function of the sun location in the sky with respect to the wind direction. It is expected that the vehicle may alter its trajectory to achieve more direct illumination of the solar panels. The generator is not used in this study, but solar energy may be stored in the battery and used later in the cycle, however, the initial and final battery charge states must be the same. Optimal trajectories were generated for each sun location on a 10 degree solar azimuth by 10 degree solar elevation grid.

Details of the optimal trajectory when the sun is located at the zenith are shown in Figs. 3.32 to 3.37. The required reference wind speed is 5.26 m/s compared to 8.66 m/s for the dynamic soaring only case. The bold lines in the plots indicate the trajectories that utilize solar energy, while the thin lines are for the case of pure dynamic soaring. The solar augmented trajectory takes longer to fly (8.17 sec vs. 6.42 sec) and is generally flown at lower speeds. The thrust is applied during the climbing portion of the flight. The thrust as a function of time takes on a triangular distribution because of the control rate limits imposed. Due to the lower wind speeds, the power from the wind is less than in the purely dynamic soaring case. From Fig. 3.37 it is clear that the vehicle receives a substantial amount of solar energy throughout the cycle as the slope angle and solar incidence angle are kept low. In fact, it is everywhere

lower than in the pure dynamic soaring case in order to extract more energy from the sun.

Figure 3.38 shows the aggregate results for all of the possible sun locations with respect to the wind direction. Only half the plot is shown as the other half is a mirror image of the part shown. In this plot the distance of a point on the surface from the origin and the color both indicate the required reference wind speed to fly neutral energy cycles when the sun is located at the corresponding azimuth and elevation angle. The outer transparent shell indicates the required reference wind speed for the pure dynamic soaring case. As expected, the use of solar power decreases the required wind speed for all sun locations, with the most dramatic reductions ($> 35\%$) occurring when the sun is near the zenith with a slight preference for the sun azimuth to be in the direction the wind is blowing.

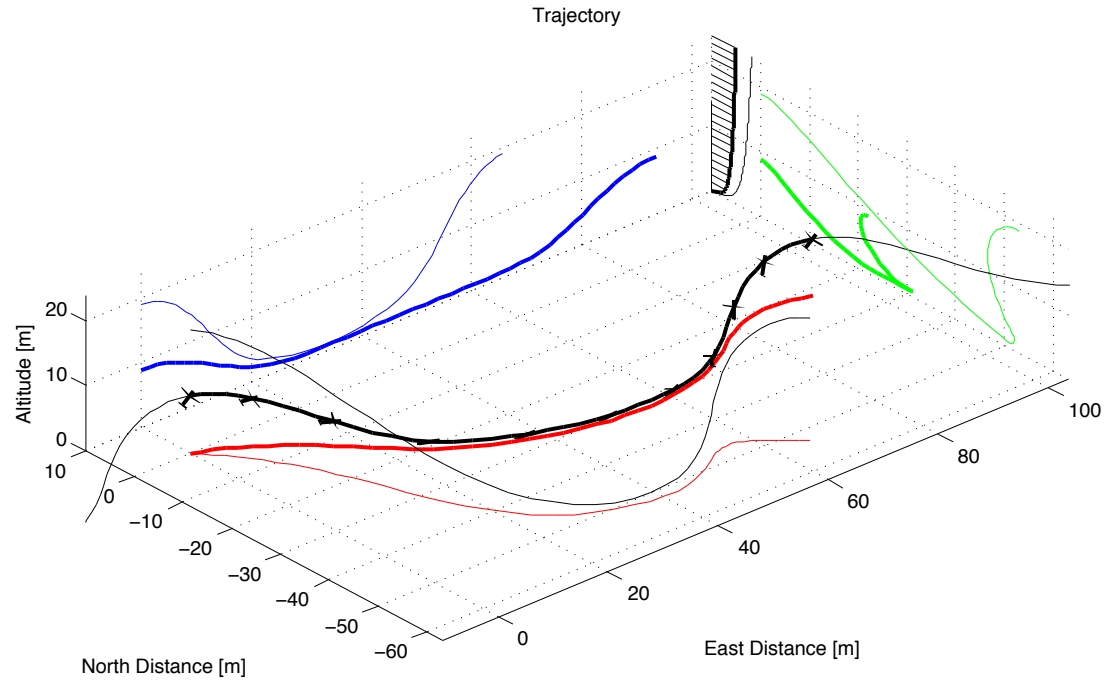


Figure 3.32: Minimum wind speed trajectories for solar augmented dynamic soaring with the sun at the zenith ($v_{ref} = 5.26$ m/s, bold lines) and pure dynamic soaring ($v_{ref} = 8.66$ m/s, thin lines). The bold wind profile near the top right indicates the distance the wind moves between successive plots of the airplane along the bold trajectory. The thin line indicates the wind profile for the pure dynamic soaring case.

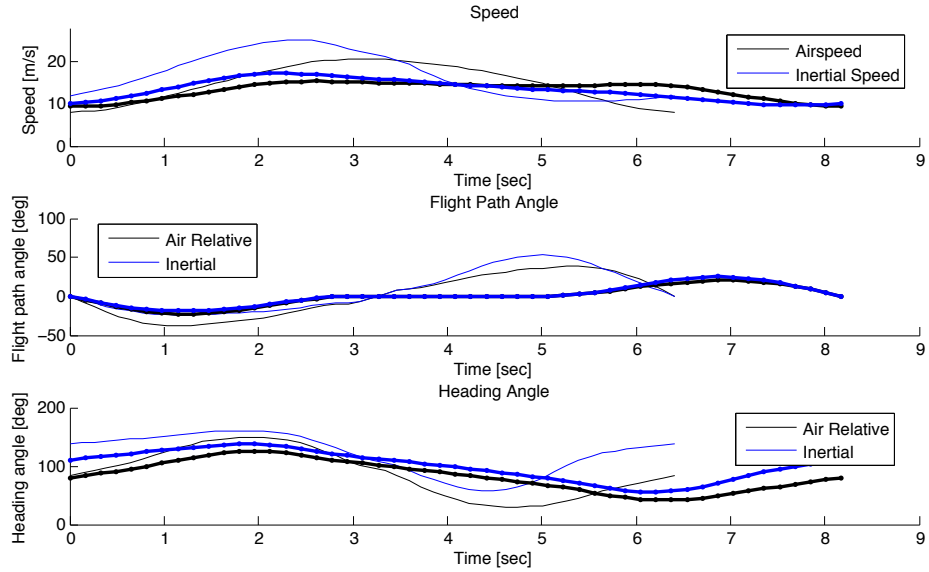


Figure 3.33: Airspeed, inertial speed, flight path angles, and heading angles for the minimum wind speed trajectories for both solar augmented dynamic soaring (bold lines) and pure dynamic soaring (thin lines).

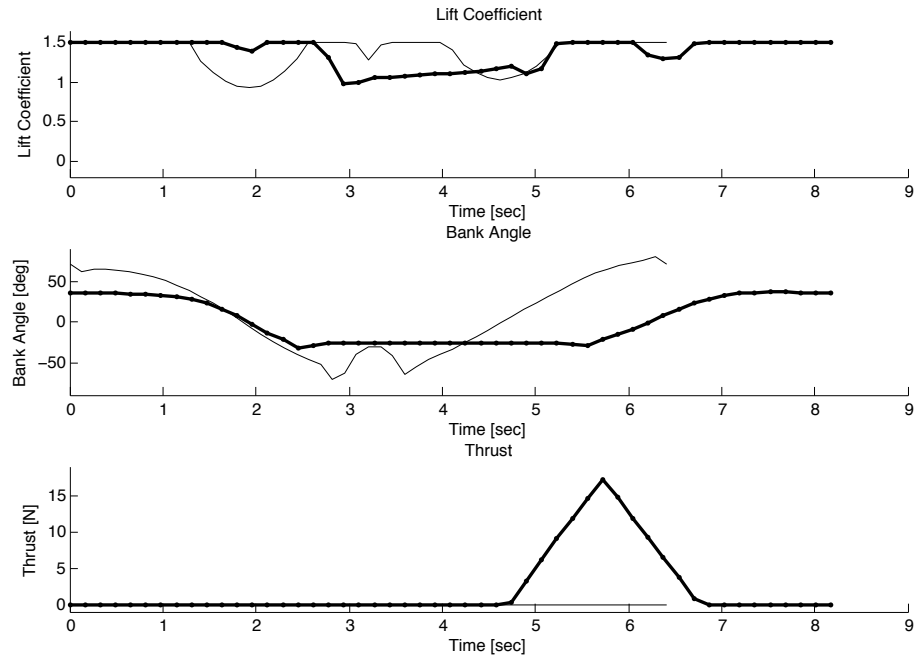


Figure 3.34: Lift coefficient, bank angle, and thrust control inputs for the minimum wind speed trajectories for both solar augmented dynamic soaring (bold lines) and pure dynamic soaring (thin lines).

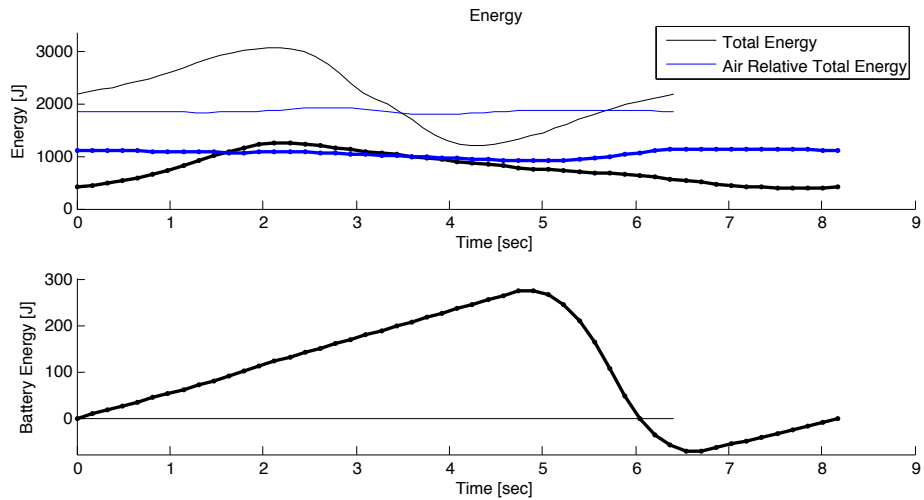


Figure 3.35: Total energy, air relative total energy, and battery energy state for the minimum wind speed trajectories for both solar augmented dynamic soaring (bold lines) and pure dynamic soaring (thin lines).

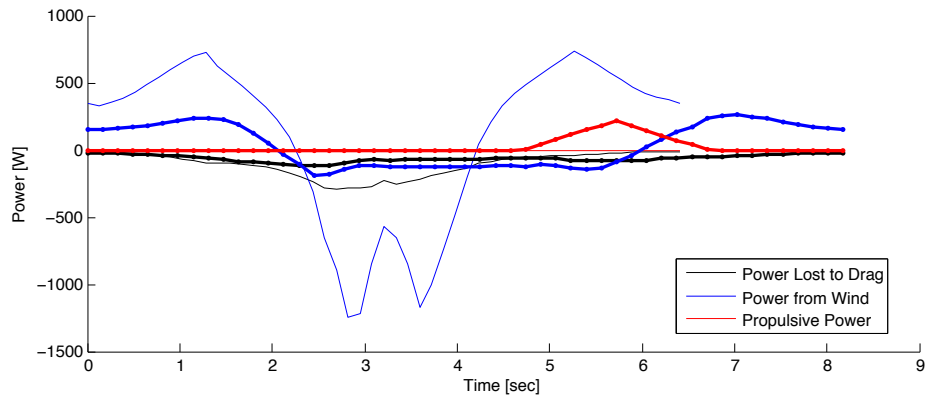


Figure 3.36: Propulsive power, power from the wind, and power lost to drag for the minimum wind speed trajectories for both solar augmented dynamic soaring (bold lines) and pure dynamic soaring (thin lines).

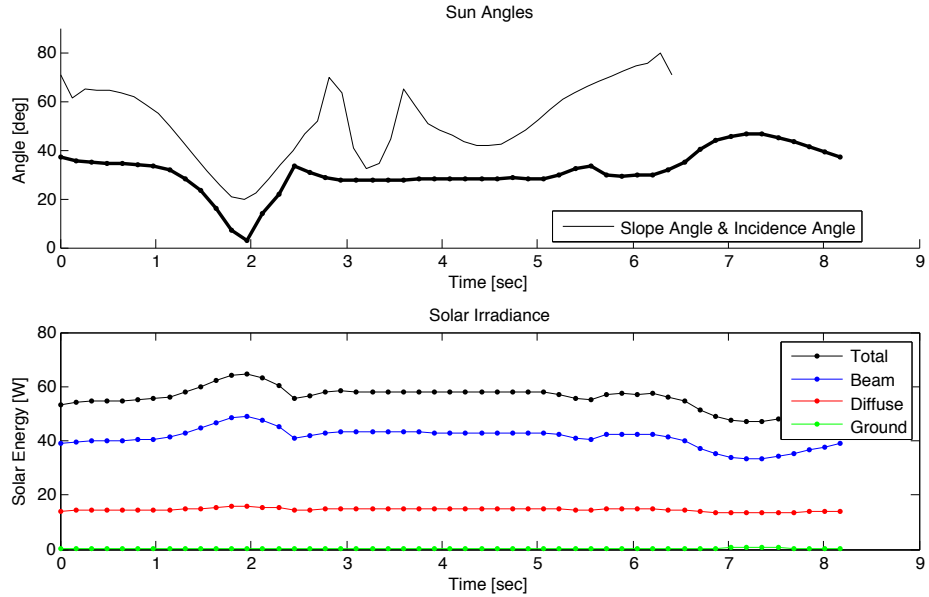


Figure 3.37: The solar panel slope angle (β) and incident light angle (θ) for the minimum wind speed trajectories for both solar augmented dynamic soaring (bold lines) and pure dynamic soaring (thin lines). The total irradiance and its three components are also shown for the solar augmented dynamic soaring trajectory.

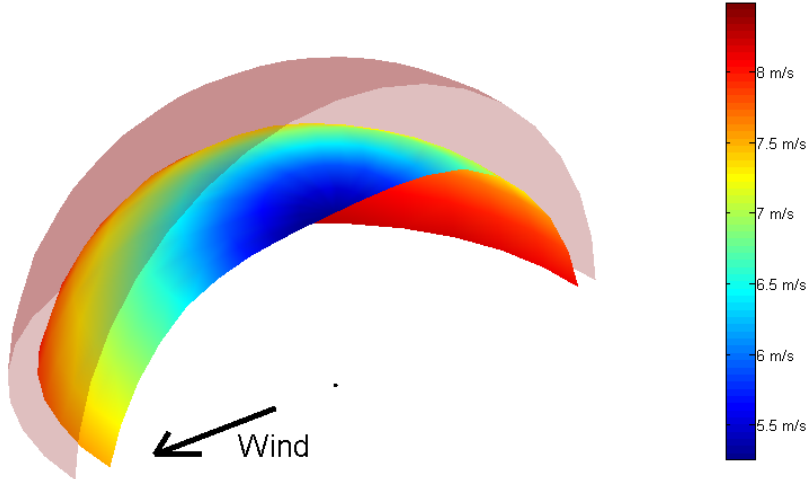


Figure 3.38: Aggregation of minimum required wind speed for solar augmented dynamic soaring as a function of the sun azimuth with respect to the wind and the elevation angle. Both the distance from the origin and the color indicate the required wind speed. The transparent shell indicates the required wind speed for pure dynamic soaring case (no dependence on the sun location).

3.5.2 Maximum Net Speed

For the second case study the objective is to maximize the net speed when flying in a net cross-country direction. For the example, the net direction was constrained to be 45 degrees off of the wind direction as this is near the maximum speed for most vehicles. Again, the optimal trajectories are found as a function of the sun location in the sky with respect to the wind direction for a fixed reference wind speed of 12 m/s. As before, the generator is not used, but solar energy may be stored in the battery for use later during the same cycle. Again, the initial and final battery charge states must be the same. Optimal trajectories were generated for each sun location on a 10 degree solar azimuth by 10 degree elevation grid.

Figures 3.39 to 3.44 present details of the optimal trajectory when the sun is located at the zenith. The maximum net speed for the solar augmented trajectory is 24.97 m/s compared to 22.93 m/s for the pure dynamic soaring case. Again, the bold lines indicate the trajectories that utilize solar energy, while the thin lines indicate pure dynamic soaring. In general, the trajectories are very similar. This is primarily due to the fact that the pure dynamic soaring trajectory is already extracting as much energy as possible from the winds, which in general is greater than that available from the solar panels. Therefore, beyond small tweaks to the trajectory it is not beneficial to give up power from the wind for solar power. The solar augmented trajectories have slightly shorter periods than the pure dynamic soaring trajectory. As before, the thrust is applied during the climbing phase of the trajectory.

One would expect the solar power augmentation to have the greatest effect on expanding the flight envelope by lowering the minimum required reference wind speed or to allow neutral energy cycles at greater angles off of the wind direction. It is clearly less useful in increasing the net speed, especially at higher wind speeds. Solar power will also prove useful for powering onboard electronics for sensors, controls, and communications that would otherwise deplete the battery or require the generator to provide power.

The aggregate results for all of the possible sun locations with respect to the wind are shown in Fig. 3.45. Here the color and distance from the origin indicate the maximum net speed when flying 45 degrees off the wind. The transparent shell on the

inside indicates the net speed for the pure dynamic soaring trajectory. As mentioned before, the addition of solar power only marginally increases the net speed as more energy is available from the wind at this reference wind speed.

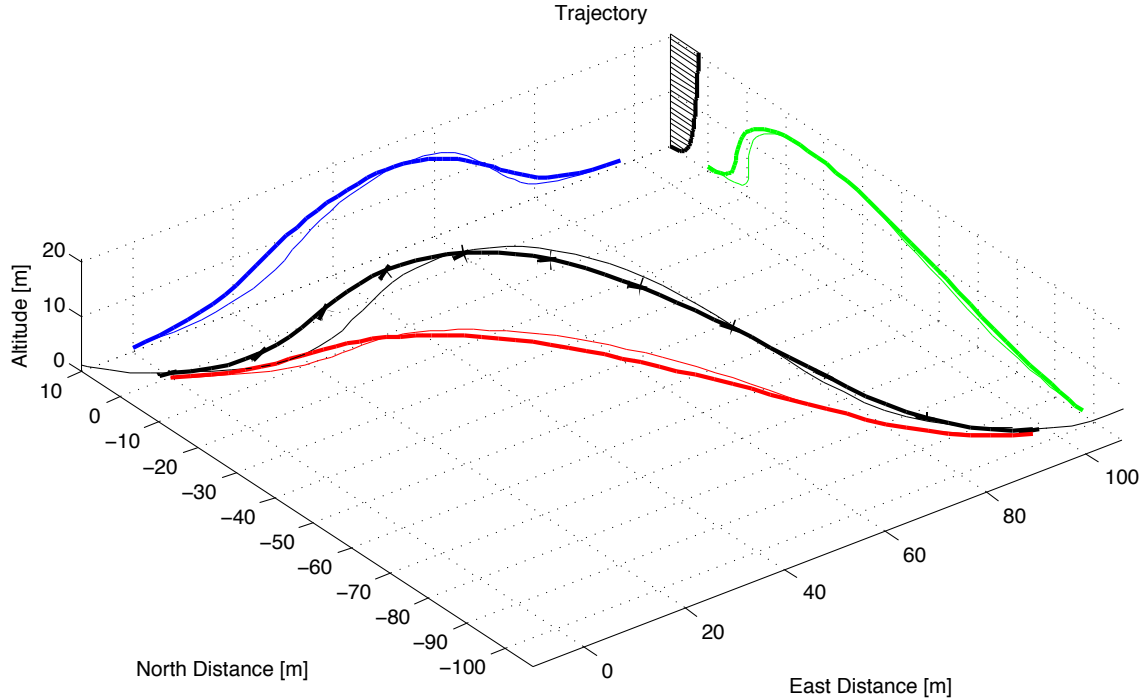


Figure 3.39: Maximum net speed trajectories for solar augmented dynamic soaring with the sun at the zenith ($v_{net} = 24.97 \text{ m/s}$, bold lines) and pure dynamic soaring ($v_{net} = 22.93 \text{ m/s}$, thin lines) when flying 45° off the wind direction with a 12 m/s reference wind speed. The bold wind profile near the top right indicates the distance the wind moves between successive plots of the airplane along the bold trajectory.

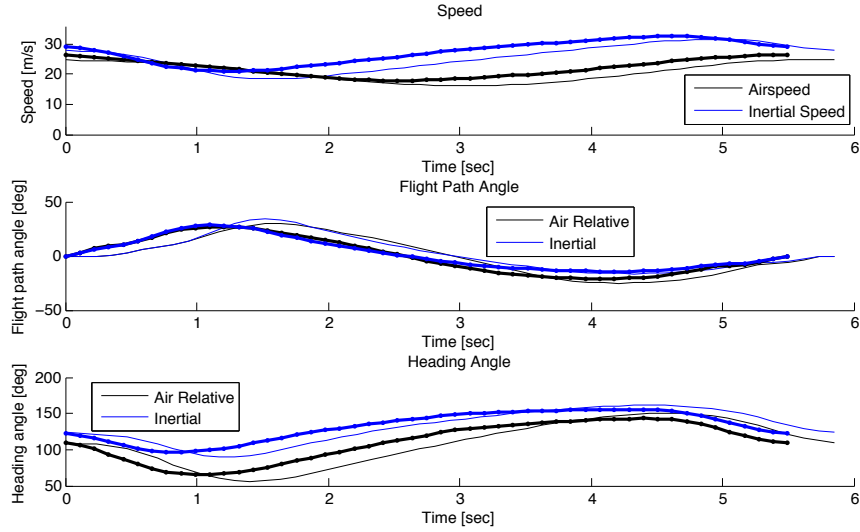


Figure 3.40: Airspeed, inertial speed, flight path angles, and heading angles for the maximum net speed trajectories for both solar augmented dynamic soaring (bold lines) and pure dynamic soaring (thin lines) with $v_{ref} = 12$ m/s and a net travel direction of 45° off the wind.

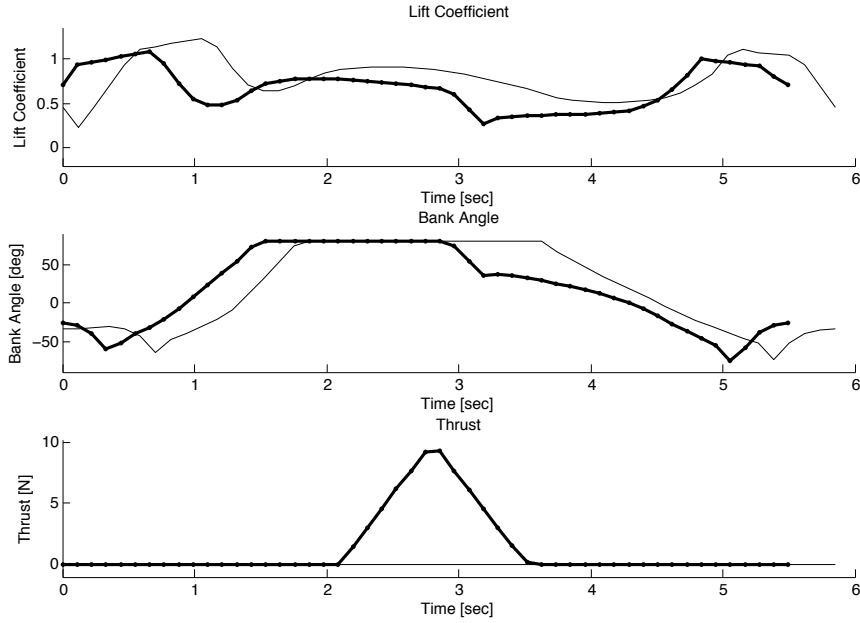


Figure 3.41: Lift coefficient, bank angle, and thrust control inputs for the maximum net speed trajectories for both solar augmented dynamic soaring (bold lines) and pure dynamic soaring (thin lines) with $v_{ref} = 12$ m/s and a net travel direction of 45° off the wind.

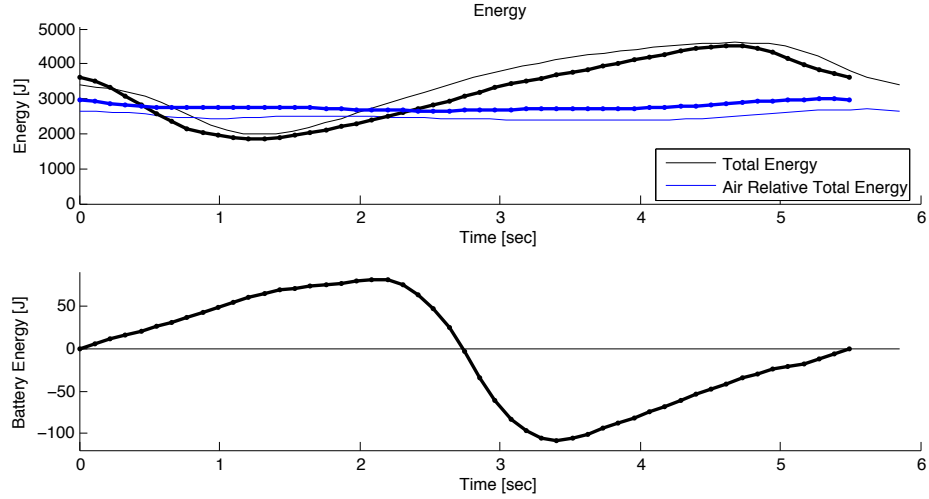


Figure 3.42: Total energy, air relative total energy, and battery energy state for the maximum net speed trajectories for both solar augmented dynamic soaring (bold lines) and pure dynamic soaring (thin lines) with $v_{ref} = 12$ m/s and a net travel direction of 45° off the wind.

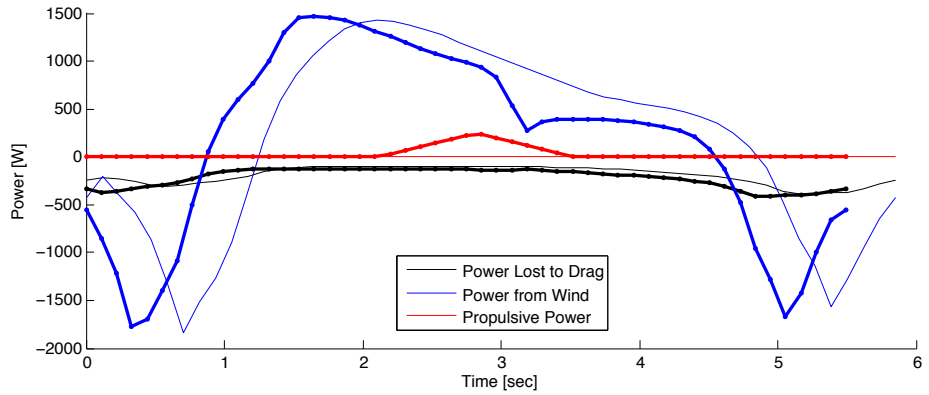


Figure 3.43: Propulsive power, power from the wind, and power lost to drag for the maximum net speed trajectories for both solar augmented dynamic soaring (bold lines) and pure dynamic soaring (thin lines) with $v_{ref} = 12$ m/s and a net travel direction of 45° off the wind.

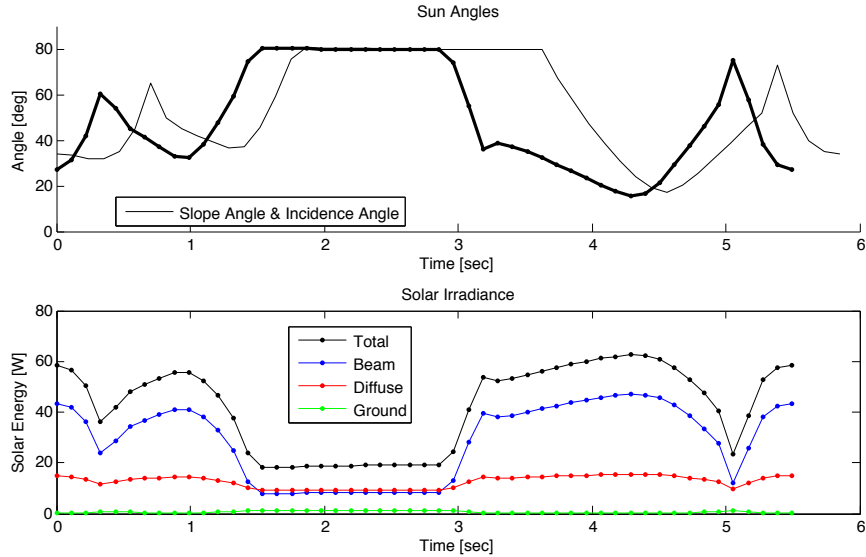


Figure 3.44: The solar panel slope angle (β) and incident light angle (θ) for the maximum net speed trajectories for both solar augmented dynamic soaring (bold lines) and pure dynamic soaring (thin lines) with $v_{ref} = 12$ m/s and a net travel direction of 45° off the wind. The total irradiance and its three components are also shown for the solar augmented dynamic soaring trajectory.

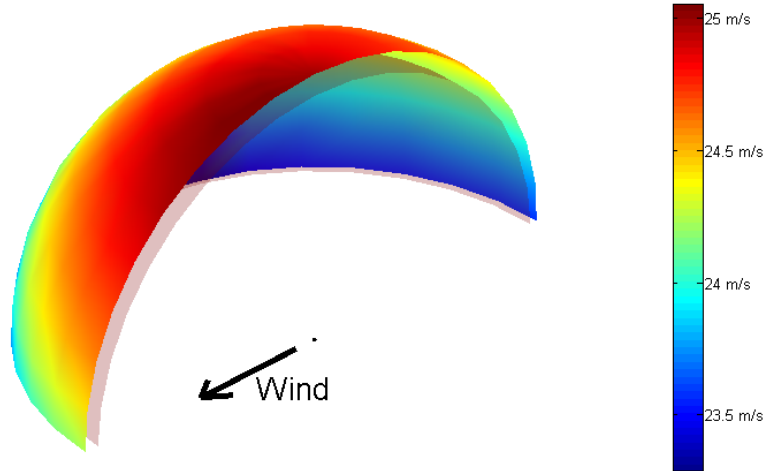


Figure 3.45: Aggregation of maximum net speed for solar augmented dynamic soaring as a function of the sun azimuth with respect to the wind and the elevation angle for $v_{ref} = 12$ m/s and a net travel direction of 45° off the wind.. Both the distance from the origin and the color indicate the net speed. The transparent shell indicates the net speed for the pure dynamic soaring case (same for all sun locations).

3.5.3 Battery Charging/Discharging

The final case study examines the effect of net battery charge rate on the maximum speed in a given direction. Here the generator may be used in addition to solar panels to provide electrical power to the battery. Again, the reference wind speed is set to 12 m/s and the net travel direction is constrained to 45° off of the wind.

Figure 3.46 shows the maximum net speed as a function of the net battery charge/discharge rate over a dynamic soaring cycle. Two sets of data are shown, in black is the set with no solar power, as would be the case at night, and blue corresponds to the sun being located at the zenith. There are two distinct sections of each curve, a linear one and curved one at higher battery charge rates. The linear sections indicate where stored battery energy and solar power are being used to increase the net speed of the vehicle. The returns are relatively modest using this energy to increase the speed. The curved portions where the net speed quickly decreases indicates trajectories where the generator is being used to charge the battery at the expense of increased drag and lower net speeds.

For other sun locations the curves will look similar and mostly lie between these two curves. The addition of a constant P_{load} for sensors, controls, and communications systems will act to shift the curves to left. If such a load exists, a conclusion from these curves is that it is best to charge the battery during the day and to drain it at night. By doing this, the vehicle can operate on the linear portions of the curves as much as possible without losing significant speed by using the generator. For example, if $P_{load} = 10$ W, then the battery will be drained at roughly 10 W during the night and is capable of being charged at a peak of about 30 W during the day without affecting the net speed.

There are many other interesting studies that could be conducted using the energy equation of motion. In general, the important conclusion is that it is possible to quickly generate trajectories that maximize net speed for given environmental conditions (wind speed and direction, sun location, clearness index) and choice of high level controls (net flight direction, net battery charge rate). Results such as these are useful for long range mission planning and will fit into the discussion in Chapter 4.

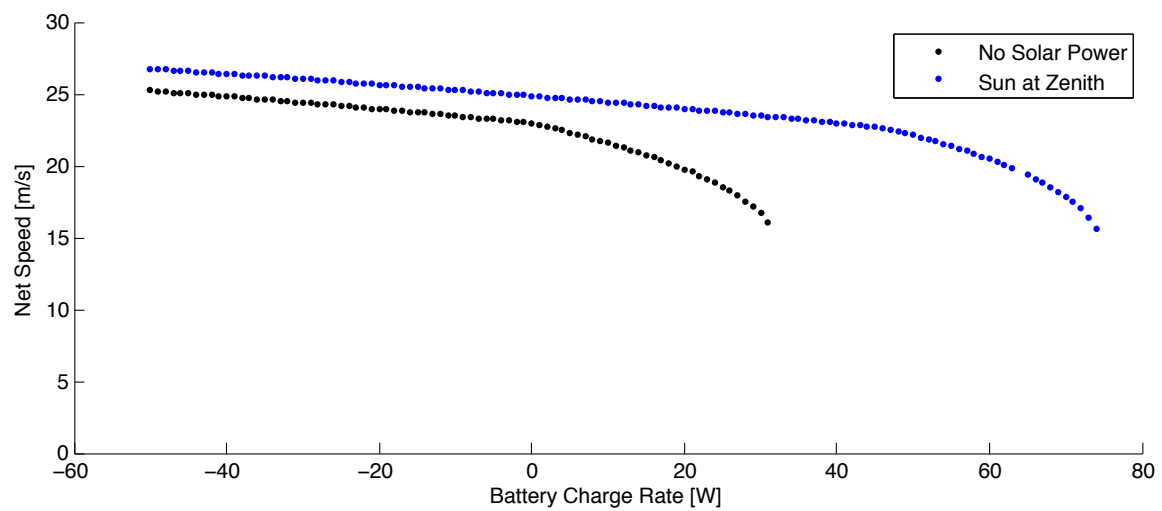


Figure 3.46: The maximum net speed as a function of the battery charge/discharge rate. The reference wind speed is 12 m/s and the vehicle is flying 45° off of the wind direction. The black dots correspond to no solar power and the blue dots correspond to the sun located at the zenith.

Chapter 4

Trajectory Planning and Control

This chapter focuses on the different control techniques required to guide a dynamic soaring UAV over the ocean. The techniques range from short-term control algorithms that are concerned with control surface deflections for the next fraction of a second, to strategic planning of multi-day routes across the ocean.

The proposed control solution has three hierachal levels. The lowest level is the inner-loop controller which deflects the control surfaces to match the state and control variable targets from the mid-level controller. The mid-level controller uses model predictive control (also known as a receding horizon control) to track a target trajectory. The target trajectory is selected from a database of optimal trajectories for different wind speeds and high-level control inputs such as net heading and net battery charge/discharge rate. The high-level mission planner makes decisions about the net heading and battery charge/discharge rate of the vehicle as it navigates across the ocean based on wind predictions from satellite and buoy wind measurements compiled as part of the National Oceanic and Atmospheric Administration's (NOAA's) Wave Watch III (NWW3) product [51].

A colleague is working on the low- and mid-level controllers as a part of his thesis, the current state of these methods will be briefly summarized [19]. The remainder of the chapter focuses on the high-level mission planner developed as part of this thesis.

4.1 Low- and Mid-Level Trajectory Planning and Control

The task of the low- and mid-level control algorithms is to guide a dynamic soaring vehicle along the optimal trajectory selected from a database for the corresponding wind conditions and high-level commands such as the net flight direction. In general, the vehicle will not be able to exactly track the desired trajectory due to modeling errors or disturbances such as wind gusts. It is also likely that the true wind profile will not match the assumed profile used to generate the optimal trajectories.

One previous study looked at using a LQR controller to track a nominal dynamic soaring trajectory in simulation [52]. For the mid-level controller in this work, Flanzer [19] has applied a model predictive controller (also known as receding horizon controller) to generate mid-level control commands such as bank angle and lift coefficient. The model predictive controller optimizes these command trajectories over finite time horizon (typically one soaring cycle) to achieve some objective, such as tracking the desired trajectory as closely as possible. The first step of the planned control actions are applied, and the process is repeated. By projecting ahead, the model predictive controller is able to conduct the fundamental dynamic soaring tradeoff of giving up some potential energy gain now in order to gain energy from the wind later in the cycle. In Flanzer's implementation, the weights applied to each state in the MPC objective differ in order to achieve the desired performance. For instance, by placing more emphasis on tracking the altitude when the vehicle is close to the ground it is possible to reduce the risk of the vehicle contacting the surface. Flanzer has also examined using stochastic collocation methods to design trajectories that are inherently robust to modeling uncertainties [53].

Additionally, Flanzer is investigating augmenting the MPC law with a repetitive control scheme. Repetitive control is based on the internal model principle which states that for a closed loop system to track a reference without steady-state error, a model capable of generating that reference must be included within the system itself. For periodic signals, this can be achieved with a time delay element inside a positive feedback loop. Applied to dynamic soaring, the idea is that after one

soaring period, the tracking errors of the trajectory just completed will be used to adapt the trajectory about to be flown. With this technique, periodic environmental disturbances and periodic errors due to model mismatch can, over time, be cancelled out.

Finally, the low-level controller is tasked with tracking the desired bank angle and lift coefficient commands by deflecting the control surfaces. Flanzer has implemented lateral and longitudinal LQR controllers augmented with error states to give appropriate integral feedback terms. The longitudinal law tracks airspeed and altitude commands using elevator and throttle. The lateral law uses roll rate and sideslip tracking (p-beta) to achieve a commanded bank angle. All of the details of these controllers are yet to be finalized and will depend on the final vehicle design and flight test results.

4.2 High-Level Trajectory Planning and Control

The high-level trajectory planner is concerned with describing the motion of the vehicle over long time scales, on the order of hours to days. This is an important aspect for the control of an operational dynamic soaring UAV, as the vehicle performance strongly depends on the available winds, which vary dramatically with location and time. For traditional airplanes the ground speed varies a small and predictable amount with wind speed and direction, indicating that for all but the longest routes, a great circle ground track will be close to optimal. For a dynamic soaring UAV, the ground speed is strongly dependent on both the reference wind speed and direction. In some cases, if the wind speed is too low, it might not be able to fly at all. Alternatively, for strong winds the vehicle may be able to fly 40 m/s in one direction, but still be unable to make any progress in another. For any long distance dynamic soaring problem of interest, the minimum distance trajectory is almost certainly not the minimum time trajectory. The remainder of this section will focus on finding the minimum time trajectory from an origin location to a target location by taking into account vehicle performance and information about the winds. Rather than invent a new method, one that has been shown to work well on similar problems was selected.

4.2.1 Problem Formulation

Finding the minimum time trajectory is formulated as an optimization problem. The vehicle state variables include the latitude (ϕ) and longitude (λ), and the control variable is the net heading (ψ). If changes in the onboard battery energy are also considered, then the battery energy ($E_{battery}$) is an additional state variable, and the charge/discharge rate ($\dot{E}_{battery}$) is a control variables.

$$\bar{x} = \begin{bmatrix} \phi & \lambda & (E_{battery}) \end{bmatrix}^T \quad (4.1)$$

$$\bar{u} = \begin{bmatrix} \psi & (\dot{E}_{battery}) \end{bmatrix}^T \quad (4.2)$$

The state and control variables may be bounded, where the latitude and longitude state bounds enforce boundaries on the navigable area. The state bounds on the battery energy correspond to a depleted and a fully charged battery. The heading angle is constrained between 0° and 360° . The battery charge rate is limited by available sunlight and generator power while the maximum discharge rate is limited by the maximum power of the propulsion system.

$$\bar{x}_{min} \leq \bar{x} \leq \bar{x}_{max} \quad (4.3)$$

$$\bar{u}_{min} \leq \bar{u} \leq \bar{u}_{max} \quad (4.4)$$

The equations of motion describe the change in the location and battery energy as a function of the current state, the control inputs, and the time. This function computes the wind speed and direction at the current location and time, then returns the vehicle's net speed at the specified net heading and battery charge/discharge rate.

$$\frac{d\bar{x}}{dt} = f(\bar{x}, \bar{u}, t) \quad (4.5)$$

For the minimum time trajectory optimization problem, the objective function, J , is the arrival time.

$$J = t_{final} \quad (4.6)$$

In addition to the bound constraints, the equation of motion constraints given by Eq. 4.5 must be satisfied at each time step.

As formulated, the calculus of variations has been proposed to solve the problem in the continuous state space [54, 55], however, other than for simple analytic cases it is intractable for this problem. The dynamic soaring aircraft performance and ocean wind models have non-smooth first derivatives that cause numerical issues. It is also difficult to generate feasible trajectories and to incorporate state and control bound constraints [54].

By discretizing the optimization problem in time and space, dynamic programming may be used to solve for the optimal trajectory. Dynamic programming recursively solves the Bellman equation to generate the optimal state and control trajectories. The accuracy of the resulting solution depends on the discretization level, so for long range trajectories with reasonable time and space discretization the problem quickly becomes intractable.

The method of isochrones, a heuristic method used in this work, discretizes the problem in time. While it is not necessarily the optimal solution to the dynamic programming problem, this method has been shown to perform well on similar problems, such as the weather routing of ships [54, 56, 57, 58, 59]. From this point on, the battery energy state variable and the battery energy rate control variable are not considered. However, this method may be expanded to include them at added computational expense.

At the first step of the method of isochrones, the vehicle state (latitude and longitude) is propagated through the equations of motion from the initial state for a discretized set of controls (net heading). This generates a new set of potential states for the start of the next time step. At the next time step, the vehicle state is again propagated through the equations of motion for a discretized set of controls, except this time it is done for each of the potential states from the previous time step. If this process is repeated at each time step it is obvious that the number of potential states will grow exponentially with time. The method of isochrones trims the set of potential states at each time step to be the set of states that are furthest from the previous state boundary. This set of points bounds the state space reachable in equal

time, hence the term isochrone. If the parent state and the control action that led to each new state are saved, then it is simple to retrace a route back to the origin location. Figure 4.1 illustrates the concept for three time steps.

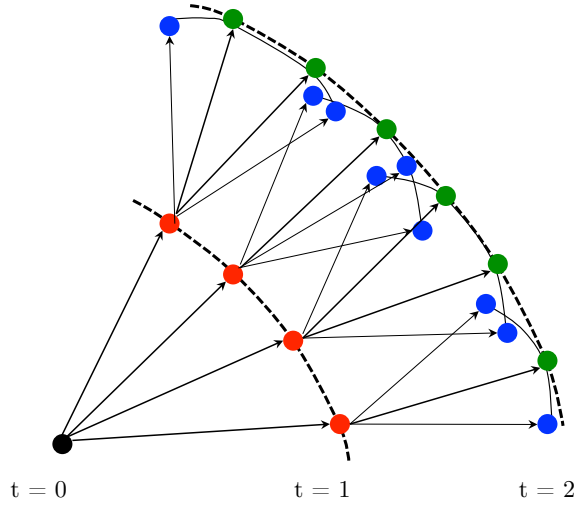


Figure 4.1: Cartoon illustrating 3 steps of the isochrone method. The initial point is shown in black. The isochrones are shown by the dashed black lines. The red points show those lying on the isochrone at $t = 1$. The green points lie on the isochrone at $t = 2$. The blue points were candidates at $t = 2$, but do not lie on the isochrone.

To solve for the optimal trajectory from an origin location to a target location, the method of isochrones is run until an isochrone encircles the target location, at which point the minimum time to reach the target location is known. The optimal route and control actions corresponding to it are then generated by starting with the isochrone point closest to the target and backtracking through the parent states and control actions.

In Fig. 4.1 it is relatively straight forward to identify the points corresponding to the isochrone at each time step, but for realistic problems the isochrones may take on complicated, non-convex shapes. Algorithm 4.1 was used to identify those points lying on the isochrone at a given time step.

The inputs to the algorithm are the set of locations reachable from the previous isochrone ($X_{candidate}$) and a length scale (d_{min}) that represents the minimum sized features that the isochrone should maintain as it grows. This distance also corresponds

Algorithm 4.1 Identify Isochrone Points ($X_{candidate}, d_{min}$)

- 1: Identify the furthest point in $X_{candidate}$ from the origin location, x_{max} , set $x_{current} = x_{max}$, and add it to the set $X_{isochrone}$
 - 2: Find the set of points in $X_{candidate}$ within distance d_{min} of $x_{current}$, call it P
 - 3: Calculate the angle measured clockwise from the vector from the origin to x_{max} to the vectors from $x_{current}$ to each of the points in P
 - 4: Select the point with the minimum angle as the next point, x_{next} , and add it to $X_{isochrone}$
 - 5: **repeat**
 - 6: Set $x_{previous} = x_{current}$ and $x_{current} = x_{next}$
 - 7: Calculate the set of points, P , within distance d_{min} of $x_{current}$
 - 8: For each point in P find the angle measured clockwise from the vector from $x_{current}$ to $x_{previous}$ to the vectors from $x_{current}$ to each point in P_{min}
 - 9: Select the point with the minimum angle as the next point, x_{next} , and add it to $X_{isochrone}$
 - 10: **until** $x_{next} = x_{max}$
 - 11: **return** $X_{isochrone}$
-

to the maximum distance between successive points identified on the next isochrone. The algorithm is shown pictorially in Fig. 4.2.

It should be noted that this algorithm does not track “islands” that are formed when an isochrone pinches off a region as illustrated in Fig. 4.3. Extensions to the algorithm have been considered that identify when these regions are formed, but were not implemented as they do not present an issue unless the target location is inside the “island”. This was not the case during any simulations in this work.

4.2.2 Receding Horizon Control with the Method of Isochrones

Using the method of isochrones to identify the minimum time trajectory requires that the true wind field be known in advance for all times until the destination is reached. In reality, when guiding the vehicle towards a distant destination this is clearly not the case. Fortunately, the future wind field can be predicted by weather models, allowing the method of isochrones to plan a route through the expected winds. A portion of the trajectory is then flown, and planning is repeated when updated wind measurements and predictions are available. This process of re-planning every time

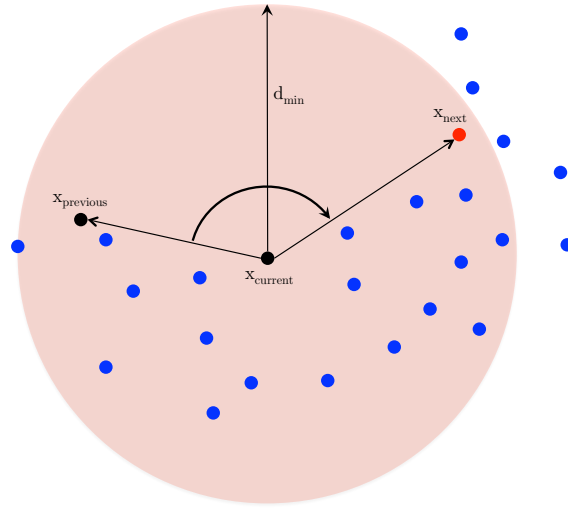


Figure 4.2: Illustration of one step of the algorithm to identify which points lie on an isochrone. The black dots indicate the previous point and the current point. The red shaded region indicates which points lie within d_{min} of the current point. The blue points represent candidate points for the next isochrone point. The red point is identified as the next point on the isochrone since it lies at the minimum angle inside the shaded region.

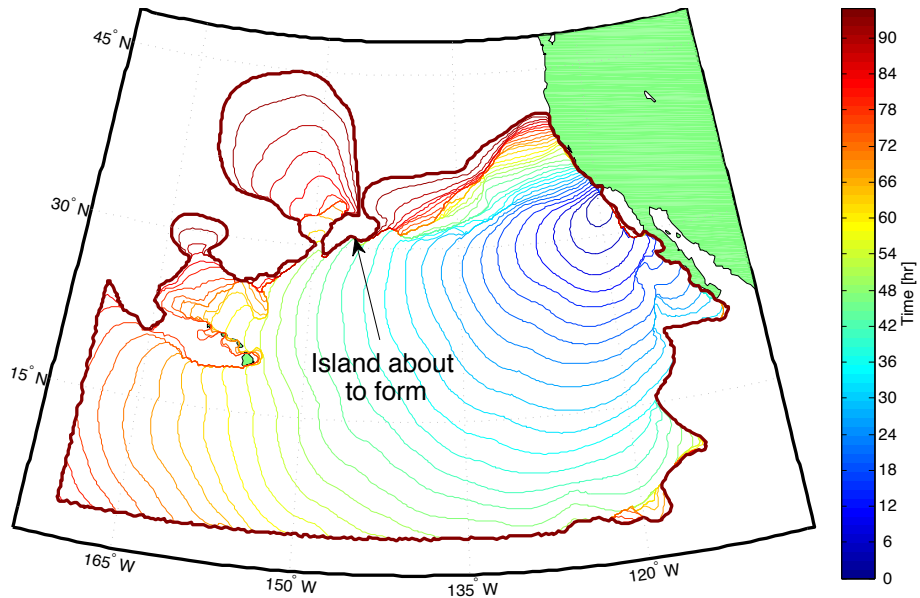


Figure 4.3: Example showing an isochrone pinching off an area to form an “island” which is no longer tracked by the current isochrone boundary identification method

new wind information is available may be repeated until the target destination is reached. Such a control scheme is closely related to receding horizon control (RHC), as discussed in the previous section, accepting that the objective function does not follow the typical RHC formulation of tracking some desired state trajectory.

As stated previously, the objective of the controller is to reach the destination in the minimum time. For some missions, it may not be possible for the planned trajectory to reach the destination within the planning horizon. The objective used to identify the best trajectory at the current time is to select the point that gets you closest to the destination within the specified planning horizon. For longer planning horizons or near the end of the mission the closest point will likely be the destination itself.

There are three time scales of interest for the receding horizon controller using the method of isochrones. There is the planning horizon, which dictates how far into the future the trajectory is planned. Next, there is the control horizon, which is the length of time the control inputs from the previous planning step will be executed until another plan is formulated. Finally, there is the integration time step, which also corresponds to the rate at which the control inputs are computed. The receding horizon controller using the method of isochrones is summarized by Alg. 4.2.

Algorithm 4.2 Receding Horizon Control with the Method of Isochrones ($x_{initial}$, x_{target} , $t_{planning}$, $t_{control}$, $t_{integrate}$)

- 1: Set $x_{current} = x_{initial}$
 - 2: **repeat**
 - 3: Run the method of isochrones from the point $x_{current}$ for $t_{planning}$ through the predicted wind field at discrete time steps of length $t_{integrate}$
 - 4: Identify the point closest to x_{target} and the trajectory leading to it from $x_{current}$
 - 5: Execute the control inputs from the plan for time $t_{control}$ on the true wind field to reach x_{next}
 - 6: Set $x_{current} = x_{next}$
 - 7: **until** $x_{current} = x_{target}$
-

4.2.3 Example Results

In this section, the receding horizon controller with the method of isochrones is used to route a dynamic soaring UAV from the Farallon Islands outside San Francisco Bay to the Northeast coast of the island of Oahu in Hawaii. The wind data released every six hours by NOAA's Wavewatch III (NWW3) between March 25th and April 4th, 2011 was archived and used for the simulations [51]. The NWW3 ocean wind data is released worldwide on a 1.25° longitude by 1° latitude grid. Higher resolution estimates are also published for a number of regions on a 0.25° by 0.25° grid, including the Northeast Pacific region used in this example. The wind estimates are based on radar scatterometer measurements by orbiting satellites and measurements from buoys. Along with the current winds, NWW3 publishes predicted winds based on their weather models for the next 180 hours in 3 hour increments. Therefore, for the example presented in this section, the control horizon was set at 6 hours, as this was how often new wind estimates were available to re-plan the trajectory. An integration time step of 0.5 hours was used, and the planning horizon was varied to gauge its impact on controller performance and computation time. All calculations were carried out assuming a spherical Earth and the parameter d_{min} was set to 0.3° .

For the example problem, the true winds at a given location and time are taken to be a linear interpolation in latitude, longitude, and time of the current winds published every 6 hours. The same linear interpolation scheme is used on the wind prediction dataset to obtain the predicted winds at any latitude, longitude, and time from the current planning time. More sophisticated interpolation schemes could be used, but were not considered for this example. For the results presented below, the simulations were started 102 hours after the start of the dataset, at 0600 GMT on March 29, 2011.

The dynamic soaring UAV that was simulated had the geometry and aerodynamic parameters given in Table 4.1, which is also used as a set of baseline design parameters in the next Chapter. Speed polars were generated using some of the constraint values shown in the table at a range of wind speeds up to 20 m/s. No wingtip height above the water constraint was included, but the minimum center of gravity height above the surface was limited to half of the wingspan. The resulting speed polars for the

airplane are shown in Fig. 4.4, where each color corresponds to a different reference wind speed. The distance from the origin to any point is the net speed that the vehicle travels, and the angle between the wind direction and the vector from the origin to that point corresponds to the flight direction with respect to the wind. Approximately 4000 discrete trajectory optimization problems were solved to generate the complete performance polar. Linear interpolation was used to obtain the net speed for any wind speed and flight direction.

Table 4.1: Geometry, aerodynamic parameters, and trajectory optimization constraints used to build the speed polar for the long range UAV.

Parameter	Value	Parameter	Value
Mass [kg]	3	Wing Loading [N/m^2]	70.632
$S [m^2]$	0.417	\mathcal{R}	15
C_{D_0}	0.01885	C_{D_2}	0.02122
$(L/D)_{max}$	25	b [m]	2.5
$\rho [kg/m^3]$	1.225	n_{max}	± 5
$C_{L_{max}}$	1.5	$C_{L_{min}}$	-0.2
$\phi_{max} [^\circ]$	80	$z_{min} [m]$	1.25 [m]

The overall minimum time solution corresponds to applying the method of isochrones to the true wind data. This result will be used for comparison along with the great circle route. The resulting minimum time trajectory is shown on top of the isochrones in Fig. 4.5. In this best case scenario using the method of isochones, knowing the true future winds allows the vehicle to reach Hawaii in 60 hours. Note the significant deviation of the minimum time route from the great circle route.

Figure 4.6 shows the resulting routes for the high-level receding horizon controller with planning horizons of 6, 12, 24, and 48 hours. The perfect knowledge route shown above and the great circle route are also shown. Table 4.2 compares the minimum time to reach the target location, the total distance travelled, and the overall computation time required. To illustrate each step of the method, Fig. 4.7 shows the series of planned and actual routes taken for the case with a planning horizon of 24 hours.

These results indicate that the high-level control algorithm does a good job of routing the aircraft over the oceans. In the best case, the vehicle is able to reach the

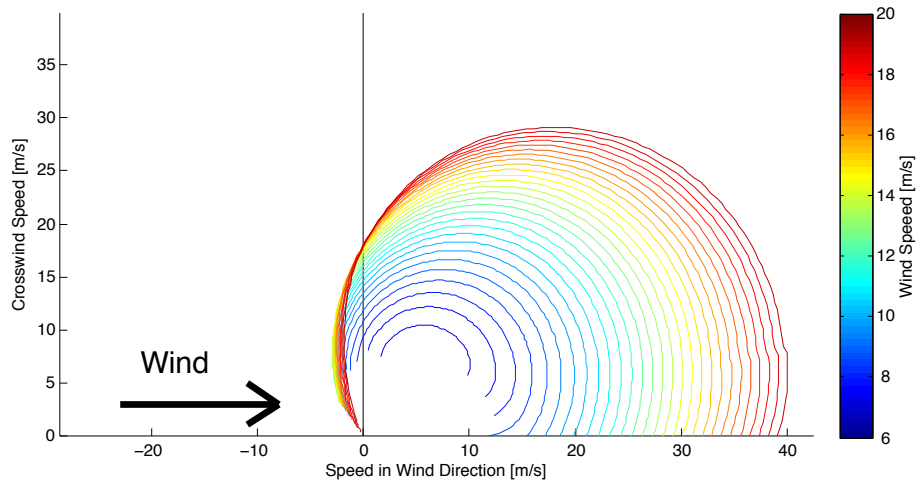


Figure 4.4: Speed polar showing the net speed as a function of heading with respect to the wind direction for different wind speeds for a long range dynamic soaring UAV. The plot may be mirrored about the $y = 0$ line to obtain the net speed for all flight directions.

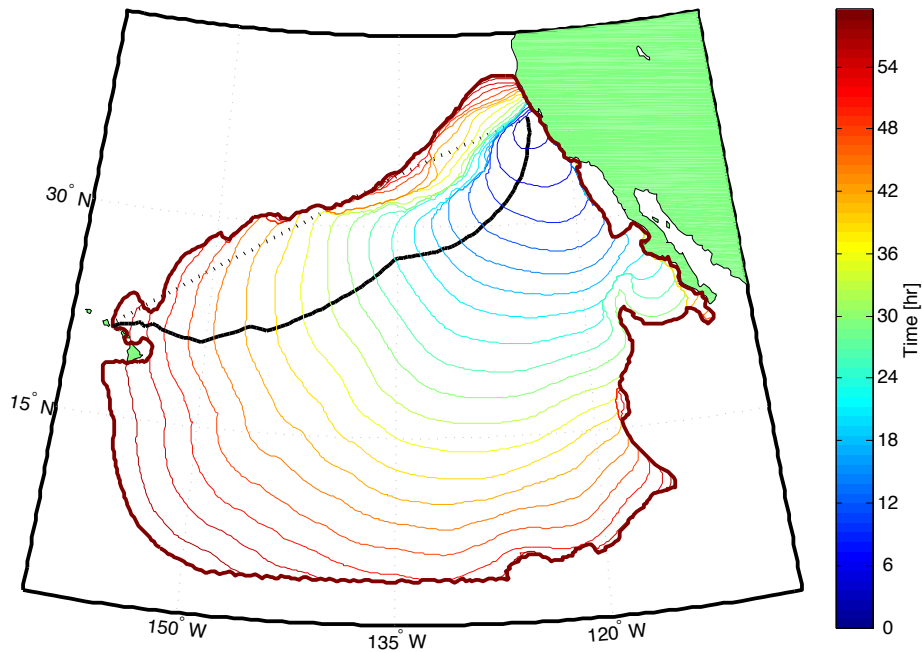


Figure 4.5: Map showing isochrones every 3 hours, and the optimal trajectory for the UAV flying from San Francisco to Oahu with perfect knowledge of the current and future winds. The minimum distance great circle route is shown by the dotted line, note the large deviations from the minimum time trajectory.

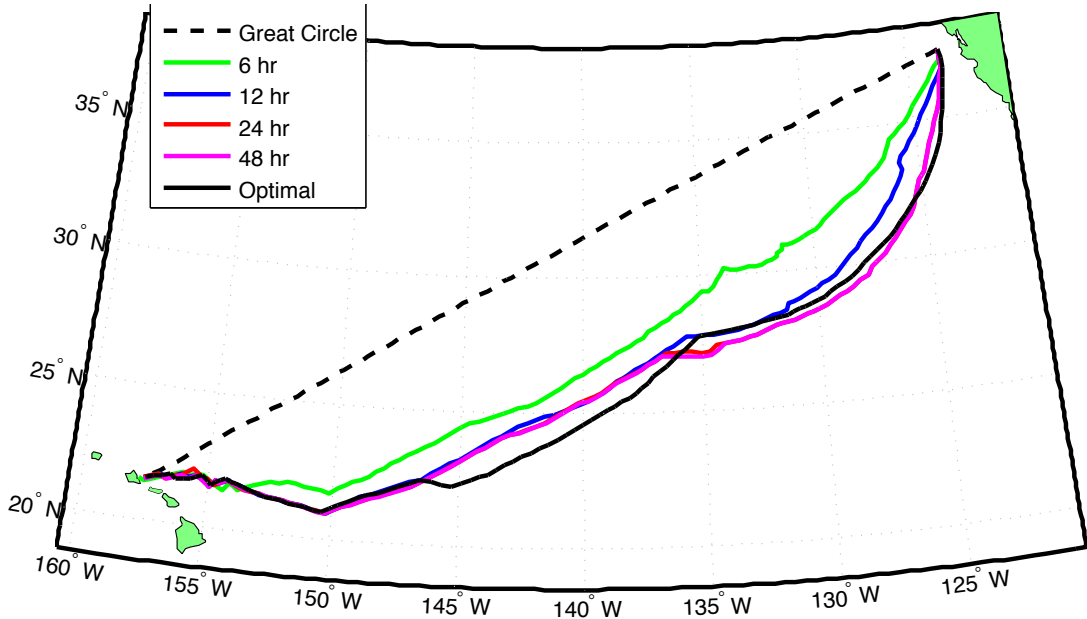


Figure 4.6: Comparison of the minimum time routes for the receding horizon controller with planning horizons of 6, 12, 24, and 48 hours. The minimum time route with perfect wind knowledge is shown by the solid black line and the great circle route is shown by the dashed black line.

Table 4.2: Comparison of travel and computation times for the high-level controller with different planning horizons. The minimum time and great circle routes are included for comparison.

Planning Horizon	Travel Time	Distance	Computation Time
(Minimum Time)	60 hr	4320 km	4353 sec
(Great Circle)	> 156 hr	3711 km	N/A
6	72.5 hr	4151 km	402 sec
12	66.5 hr	4235 km	1724 sec
24	65 hr	4296 km	5242 sec
48	66.5 hr	4306 km	15508 sec

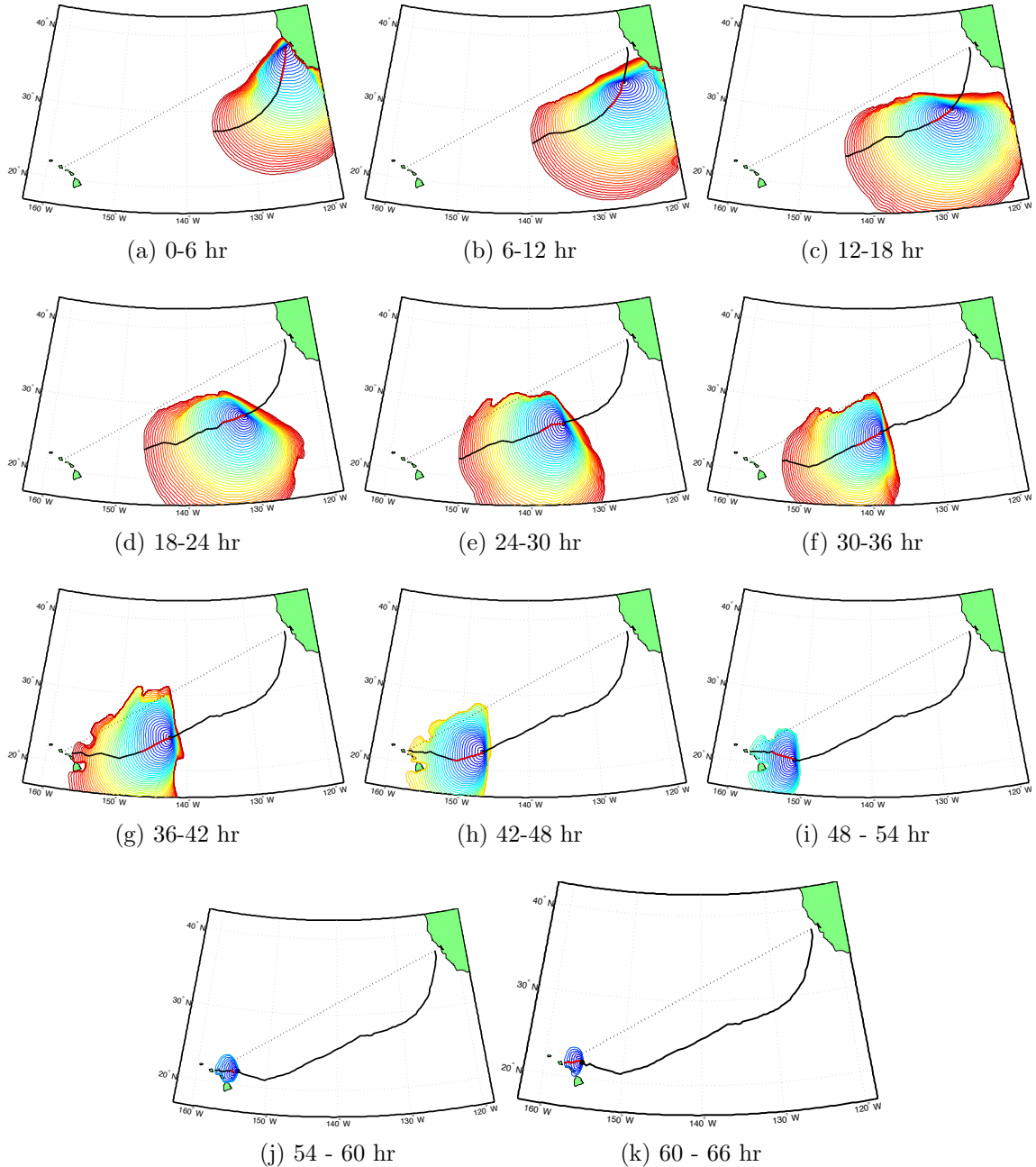


Figure 4.7: Each step of the high-level control algorithm for the 24 hour planning horizon case. Each plot shows the isochrones for the predicted wind field in half hour time steps. The solid black line indicates the current route selected by the planner and the route taken up to the indicated start time. The bold red line shows the resulting route after executing the planned controls for the control horizon of 6 hours.

destination only 8% slower than if it had perfect knowledge of the future winds. In general, all of the planned routes roughly followed the optimum route. The length of the planning horizon is shown to impact both the computation time and the overall travel time. For longer planning horizons the method of isochrones has to track more points, significantly increasing the computational resources required. Assuming a constant isochrone expansion rate (constant flight speed), the total computation time should scale with the square of the planning horizon. This growth in computation time is roughly seen in the results.

As expected, for shorter planning horizons the selected route more closely tracks the great circle route. Somewhat unexpectedly, as the planning horizon length increases, there is essentially a saturation point in terms of performance. In retrospect, it makes sense, since for longer planning horizons you are trusting the inherently uncertain wind predictions further into the future and allowing these to guide your control decision at the current time. For this example the best planning horizon length is 24 hours. For most of the 48 hour planning horizon flight, the route lies on top of the 24 hour planning horizon route. In this case there is no benefit to going to a longer planning horizon.

Further test cases are required to see how the selection of the planning horizon depends on the length of the route and the structure of the wind field. Comparing the planned and flown trajectories in Fig. 4.7, it is observed that they typically match up extremely well. This indicates that the true winds closely match the predictions, at least for the first six hours. A detailed examination of the wind prediction accuracy as a function of the time from the prediction would likely be useful in selecting the optimum planning horizon for an operational vehicle. Explicitly accounting for this uncertainty during the planning might allow selection of routes with minimum expected travel time, balancing the risks and rewards of flying in certain regions.

Finally, it should be noted that by following the great circle route in this example the aircraft is unable to reach the destination. Periodically along the route the wind speed and direction are such that the aircraft is unable make progress, so it has to wait for the winds to change. By the end of the wind dataset the vehicle has made it roughly two thirds of the way to the destination.

Chapter 5

Aircraft Design for Dynamic Soaring

This chapter details the design and sizing of a small UAV demonstrator for boundary layer dynamic soaring. As seen in the preceding chapters, dynamic soaring in the ocean boundary layer requires flying trajectories with large variations in speed and orientation over fairly short time scales. This presents many challenges compared to traditional UAV design. These include the need for precision control and trajectory tracking, especially when the vehicle is near the surface. To achieve the required precision, an accurate estimate of both the vehicle state and the wind field are necessary. This presents a challenging sensing and data fusion problem. The selected sensor suite will be discussed in this chapter, while the data fusion algorithm is discussed in the next chapter.

In terms of configuration, a conventional design was selected for its well characterized stability and control properties. The focus of this section will be on the sizing of the vehicle for minimum required reference wind speed, while imposing a reasonable constraint on the vehicle size and the requirement that it is hand launch-able. The minimum required wind speed objective was selected as the goal of this design is to demonstrate that dynamic soaring is possible, and this objective will enable that in the widest range of available winds. For an operational vehicle, designing for maximum net speed might be a better objective.

First, trade studies are conducted on basic vehicle parameters to identify the expected design trends. Next, models of the UAV's structures and aerodynamics are outlined followed by a heuristic search for a good performing design. Finally, the tail and control surfaces are sized to achieve the required stability and controllability of the final design, designated *Mariner*.

5.1 Basic Trade Studies

Trade studies were conducted on the various inputs to the minimum required wind speed trajectory optimization problem described in Chapter 2. The baseline design for these trade studies was the design used for the long range mission planning study, which is repeated in Table 5.1. Note that some of these parameters are dependent when assuming a quadratic drag polar as is done for these initial trade studies.

Table 5.1: Baseline design parameter values for basic trade studies.

Parameter	Value	Parameter	Value
Mass [kg]	3	Wing Loading [N/m ²]	70.632
S [m ²]	0.417	\mathcal{R}	15
C_{D_0}	0.01885	C_{D_2}	0.02122
$(L/D)_{max}$	25	b [m]	2.5
ρ [kg/m ³]	1.225	n_{max}	± 5
$C_{L_{max}}$	1.5	$C_{L_{min}}$	-0.2
ϕ_{max} [°]	80	$z_{tip_{min}}$ [m]	0.1
$\frac{\partial C_L}{\partial t}$	2	$\frac{\partial \phi}{\partial t}$ [°/s]	180

First, the boundary layer parameter, h_0 , was varied to gauge its impact on the required reference wind speed. Next, each of the ten independent parameters required by the trajectory optimization routine (m , S , b , C_{D_0} , $C_{L_{max}}$, ϕ_{max} , $\frac{\partial C_L}{\partial t}$, $\frac{\partial \phi}{\partial t}$, n_{max} , $z_{tip_{min}}$) were varied while holding the remainder constant. Finally, three traditional sizing and performance parameters (W/S , $(L/D)_{max}$, \mathcal{R}) were varied. These parameters match the independent variables used in the simple boundary layer analyses of Section 2.2. While each of these parameters were varied the others were held constant.

These three parameters uniquely determine C_{D_0} , m and S . Results for all fourteen trade studies are illustrated in Fig. 5.1.

As expected, large variations in h_0 impact the required reference wind speed since the “fullness” of the boundary layer depends on this parameter. If it is smaller, a larger reference wind speed will be required to achieve the same difference in wind speed between the top and bottom of the trajectory. For the subsequent design study, the nominal value of $h_0 = 0.03$ will be retained.

It is clear from Fig. 5.1b that the wing span is an important parameter. Besides controlling the induced drag it also determines how close the center of gravity of the vehicle can get to the ground. Over the range investigated it is clear that a larger span is better, however, beyond 2.5 meters there are diminishing returns. For the *Mariner* design the span will be limited to 2.5 meters to keep the vehicle a reasonable size for construction and transportation. All else being equal, for the baseline design a smaller wing area is advantageous as it leads to a higher aspect ratio and lower parasite drag.

From Fig. 5.1d it is evident that within reason, a lower mass also benefits the baseline design. This indicates the importance of selecting lightweight components to minimize the overall weight of the vehicle. It is unlikely that a mass that is low enough to hinder the performance is achievable.

As expected, C_{D_0} is a very important parameter (Fig. 5.1e). Everything possible should be done to minimize the parasite drag of the vehicle. Figure 5.1f shows the relatively small importance of achieving a high C_{Lmax} . These last two trends will be important in selecting an airfoil, as there is often a trade off between maximum lift coefficient and minimum parasite drag.

The maximum bank angle is seen to have relatively minor impact on the required reference wind speed, so long as it exceeds 45° or so. For the *Mariner* design study the limit will conservatively be set at 60° . For reference, albatross have been observed at bank angles of up to 70° [36]. The lift coefficient and bank angle rate constraints are also seen to be of minimal importance so long as the values are larger than roughly $0.5 s^{-1}$ and $60^\circ/s$, respectively. For the design problem the lift coefficient and bank angle rate constraints will be conservatively set to $0.5 s^{-1}$ and $90^\circ/s$, respectively.

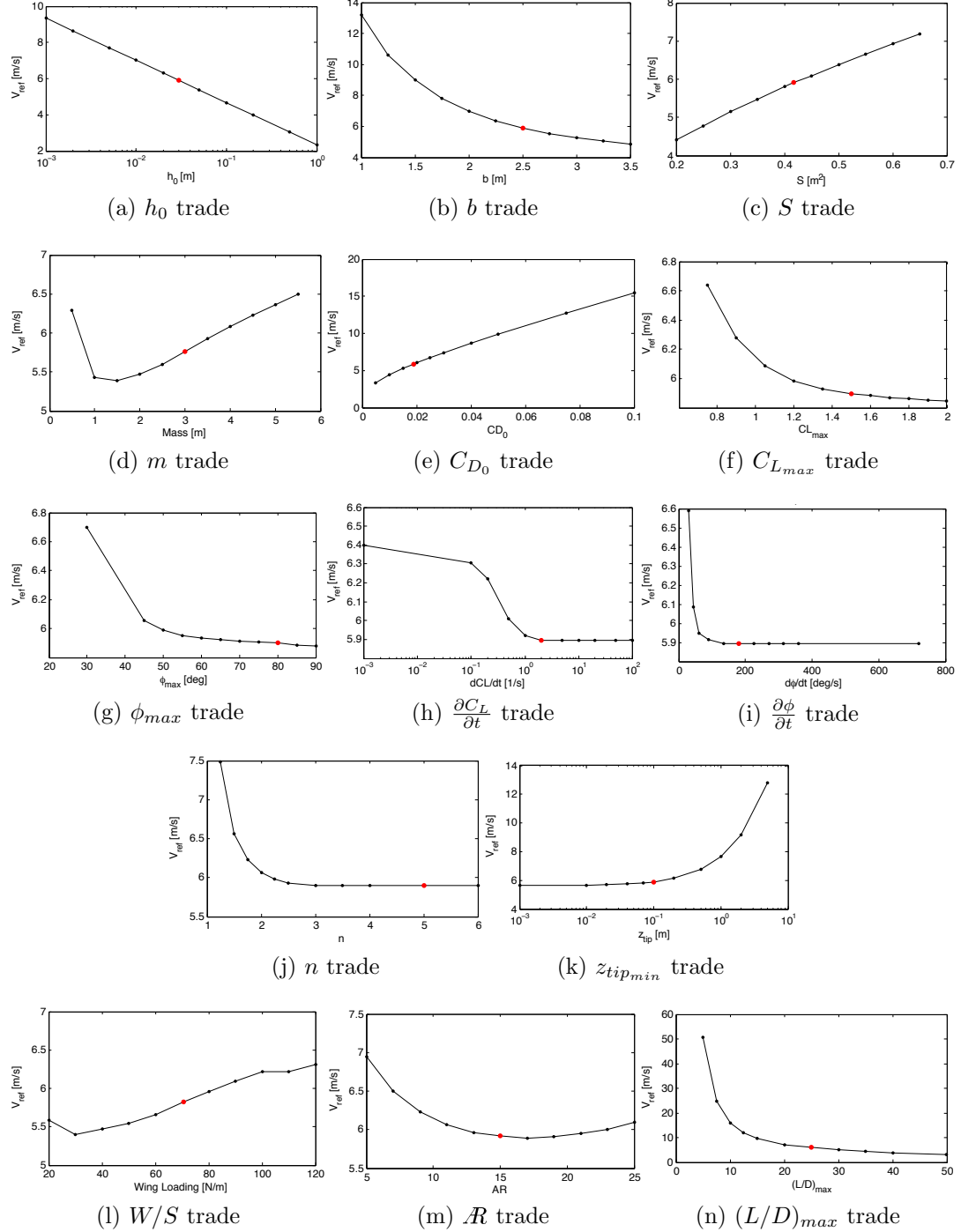


Figure 5.1: Trajectory optimization parameter sensitivity analysis about the baseline design. The red dot in each plot corresponds to the baseline design.

The maximum load factor is also observed to have no impact on the optimal trajectories so long as it is set high enough to not be an active constraint. Even if the constraint is active it has a small impact for values greater than about 2. For the following design problem the maximum load factor will be set to 3.

Figure 5.1k shows the importance of the minimum allowed wingtip height above the surface constraint. This trade is critical as it shows the importance of accurate height above ground sensors and confidence in those sensors. The more accurate the sensors are, the closer the wingtip can approach the surface, and the lower the required reference wind speed. As the *Mariner* is a demonstration vehicle, a relatively conservative constraint value of 0.5 meters will be imposed during the design.

The final three trade studies show the importance of the traditional aircraft sizing parameters. As was seen from the simple step boundary layer analysis, a lower wing loading is better, but only up to the point where the step boundary layer assumptions of Section 2.2 are valid. The required reference wind speed is fairly insensitive to \mathcal{R} , although an optimum is seen to exist for the baseline design in the range of 15 to 20. Finally, as expected the higher the maximum lift-to-drag ratio the better.

Unsurprisingly, based on the results of these trade studies, it is expected that a good dynamic soaring vehicle will have parameters somewhat similar to those of an albatross. The primary difference is that the objective of minimizing the reference wind speed should favor a design with a lower wing loading than albatross, who instead have evolved to exploit distant food sources in a timely and energy efficient manner. This likely necessitated some evolutionary compromise between minimum required wind speed to dynamic soar and maximum cross-country speed.

5.2 Aircraft Systems

The objective mission for *Mariner* is to demonstrate boundary layer dynamic soaring on short flights near either the shore or a command boat. The following requirements are critical to meeting this objective.

- Approximately 5 mile line-of-sight (LOS) communications range, with sufficient data transfer rate, preferably at 115.2 kbps

- Processing power to run the state estimation (Section 6.2) and control (Section 4.1) algorithms at at least 50 Hz
- Ability to detect height above the surface while at the maximum bank and pitch angles
- Propulsion system for flight before initiating dynamic soaring and to power the vehicle if the energy state becomes too low while soaring
- Water resistant design that can withstand brief forays into the ocean

Achieving the first requirement is perhaps the easiest. There are a number of relatively inexpensive digital RF modules on the market that provide this capability. The Digi XTend® was selected as it is a lightweight and high power 900 MHz radio that was already available in our lab. The advertised LOS range is up to 40 miles with high gain antennas, and easily meets our bandwidth and range requirements with smaller dipole antennas.

A number of solutions were investigated for the flight control computer. Ultimately, the Gumstix Overo® computer-on-module running Linux was selected for its low power, processing speed, ability to accept many peripherals, and open source architecture. The selected module has a clock speed of 1 GHz, with 256 MB of RAM, 256 MB of flash memory, a uSD card slot, and a wifi module.

Estimating the height above the water surface is likely the most difficult requirement to meet. Traditional UAV sensors such as GPS, 3-axis accelerometers, 3-axis rate gyros, 3-axis magnetometers, and barometric and differential pressure sensors will be included on *Mariner*. These sensors allow the altitude to be estimated, however, the absolute accuracy of the estimates is only as good as the long term accuracy of the GPS measurements, on the order of ± 10 meters. Dead reckoning with the inertial sensors and the altitude output of the barometric pressure sensor are useful for short term estimates of altitude, but do not achieve the required long term precision. Instead, a direct method of measuring the height above the ocean surface is required. Differential GPS from a fixed ground station was considered, however, no

commercially available units suitable for inclusion on a small UAV that has to operate at sea were found.

A number of additional sensors were considered for direct altitude estimation. The cheapest solution is the use of ultrasonic range finders. These devices send out ultrasound pulses and estimate the distance by measuring the time for the reflected signal to return to the unit. Their range is typically limited to about 10 meters. In practical tests on a small UAV their maximum measurement range is closer to 3 meters over a grass field and 6 m over a smooth water surface. Care also needs to be taken when mounting these sensors to reduce vibrations. With three range finders (one pointed down, and ones pointing 45° to each side), the distance to the surface can be estimated at any bank angle within ±60° when the vehicle is within a couple meters of the surface.

Laser rangefinders provide another possible sensor for measuring the height above the surface. Both static and scanning rangefinders are available. These sensors vary in cost between roughly \$1000 and \$10000. The cheaper sensors usually do not work in the high ambient light conditions found outdoors, and the more expensive scanning systems are too heavy and power hungry to be practical for a small UAV. The best choices are probably sensors designed specifically for small UAVs, however, their capabilities over water are unknown. We are considering using the AGL-N sensor from Latitude Engineering, which has a range up to 50 meters over land, has a small footprint, a low weight (70g), and low power requirements (1 W). Another option is a small radar altimeter such as one of the ones produced by Roke Manor Research. Again, their capabilities over water are unknown and the cost is prohibitive for a small university UAV research project.

The final sensor considered for estimating the height above the surface was stereo vision. This choice takes a cue from nature where seabirds have extraordinary vision allowing them to spot prey and obstacles while flying quickly at low altitudes [60]. Challenges with using stereo vision include the need for dedicated computing resources, significant power requirements, and unknown image feature quality over the ocean.

The propulsion requirement is also easy to achieve. An off the shelf system for powering sailplanes of a similar size was selected. This system includes the HiMax HC3516 motor coupled with a Aeronaut 10x6 folding propeller. The voltage of the flight battery was dictated by the motor and propeller choice to be a three cell lithium polymer battery. A Castle Creations Phoenix ICE 75 electronic speed controller was selected primarily for its ability to provide up to 5A of regulated 5V power for the flight controls, sensors, and communication systems. All of the selected electronic components that *Mariner* has to carry onboard are listed in Table 5.2 along with their mass and basic dimensions. The total mass of the fixed components is 931 grams.

Table 5.2: Electronic system components selected for *Mariner*.

Component	Mass	Dimensions	Notes
Himax HC3516 motor	135 g	35 dia x42 mm	$\approx 350W$ max
Aeronaut 10x6 propeller	45 g	55 dia x42 mm	Spinner dimensions
Hitec HS-85MG servos	25 g	29x13x30 mm	4 required
Spektrum AR7010 receiver	15 g	47x25x16 mm	2.4 GHz
Phoenix ICE 75 ESC	110 g	70x51x23 mm	
3300 mAh 11.1V LiPo battery	250 g	19x43x136 mm	Thunderpower G6 Pro Lite
Gumstix Overo + Summit	20 g	80x40x12 mm	
GS407 uBlox GPS	15 g	25x15x60 mm	
Digi XTend + dipole antenna	40 g	70x38x10 mm	900 MHz
IMU and pressure	15 g	75x40x15 mm	
MB7066 XL-MaxSonar-WRL1	50 g	44x44x71 mm	3 required
LSM303DLH Magnetometer	1 g	13x23x3 mm	
DV90 video camera	35 g	80x33x13 mm	Not critical

The final challenge is achieving a water resistant design. By enclosing most of the electronics in a watertight fuselage a majority of the problems are solved. There are still a number of openings that are required in the watertight fuselage to allow sensors to operate and for electrical signals to pass out to other components. Items housed outside the watertight compartment include the motor, servos and pitot probe. In addition, the sonar sensors must be mounted with unobstructed apertures pointing outside of the fuselage. Fortunately, weather resistant versions of these sensors are

available. Sealing the motor and servo wires as they pass through the waterproof enclosure is achieved through the use of waterproof grommets and silicone sealant. Individual servo cases may be sealed with the use of 3M 5200 sealant and sticky grease around the rotating output shafts. No special treatment is required for the motor, besides thorough rinsing with fresh water if it is submerged. The pitot probe is connected to the waterproof side of the selected differential pressure sensor (Freescale Semiconductor MPXV7002DP). Finally, a waterproof hatch is required on the fuselage for accessing the internal components. The primary effect of waterproofing is to add weight, which will be included in the miscellaneous markups applied during structural weight estimation.

5.3 Sizing

5.3.1 Problem Formulation

The aircraft sizing problem was posed as an optimization problem with an objective function, design variables and constraints. As discussed in the trade studies above, the objective of interest is minimizing the required reference wind speed for the log boundary layer. Here the objective is minimized by varying geometric design variables rather than individually varying the inputs to the trajectory optimization routine. The trajectory optimization inputs are computed as outputs of the aerodynamic and weight analysis methods described in the next subsection.

The selected set of design variables primarily define the shape of the wing, with the size of the fuselage and tail surfaces taken as a function of these variables for initial sizing. The selected design variables are the wing area (S), wing aspect ratio (A), wing taper ratio (λ), wing tip twist angle (θ_{tip}), the wing airfoil, and the tail airfoil. The wing root leading edge was assumed to lie at 25% of the fuselage length. A static margin of 5% was assumed, and maintained through placement of the systems in the fuselage. The wing dihedral angle was fixed at 3° and the twist was assumed to be piecewise linear with 1/3 of the total twist occurring over the inner half of the wing, and the remainder outboard. The fuselage length was set to 68% of the wing

span with a minimum length of 1 m . The fuselage diameter was fixed at 0.15 m to fit the components described in the previous subsection. The tails were initially sized based on classical volume coefficients (0.5 for horizontal, 0.05 for the vertical) with fixed aspect and taper ratios (5 and 0.6 for the horizontal tail, and 1.5 and 0.6 for the vertical tail). In the next section, the tail and control surface sizes are refined based on stability and control analyses.

In addition to the trajectory optimization constraints discussed in the trade studies above, a few other constraints were imposed on the design. First, a maximum stall speed of 8 m/s was enforced to ensure the vehicle could be hand launched. Additionally, the mass was limited to 3.0 kg and the wing span to 2.5 meters to ensure the vehicle remained a reasonable size and weight for transportability. Bounds were also placed on all of the design variables as indicated in Table 5.3.

Table 5.3: Design variable bounds for search space. The wing airfoils considered are: 1 - S7075, 2 - SD7037, 3 - SD7043, 4 - SD7062, 5 - SG6042. The tail airfoils are: 1 - NACA0008, 2 - S9027.

Design Variable	Lower Bound	Upper Bound
S	$0.2 \text{ } m^2$	$0.5 \text{ } m^2$
A	6	16
λ	0.5	1
θ_{tip}	-3°	0°
Wing Airfoil	1	5
Tail Airfoil	1	2

Due to the aerodynamic analysis methods used and the trajectory optimization “inner loop”, it was expected that the objective function would be non-smooth. Brief numerical testing indicated that this was the case. For this reason a heuristic search strategy was used to find a good design, rather than a truly optimal one. The final design was arrived at through a rational aircraft sizing routine in combination with random design space exploration and grid search.

5.3.2 Analysis Methods

A number of trajectory optimization input parameters (m , b , $C_{L_{max}}$, C_{D_0} , C_{D_1} , C_{D_2} , C_{D_3} , C_{D_4}) need to be estimated as a function of the design variables so that minimum reference wind speed of each design can be computed. The stall speed is also computed as a function of $C_{L_{max}}$.

The aircraft mass was built up as a combination of component masses. The estimated mass of the wing, fuselage, and tail surfaces were added to fixed mass of the systems described previously (931 g). The fuselage is assumed to be constructed of a 1/8 inch plywood floor, a series of 1/8 inch plywood frames spaced roughly every 12 cm, a fiberglass skin that consists of 3 layers of 1.4 oz/yd² fiberglass, plus an additional 20% to account for additional waterproofing, fasteners, and the wing carry-through structure.

The wing and tail surface masses were estimated assuming a fiberglass covered foam core structure with a carbon fiber spar caps. The foam cores are assumed to have a density of 2 lb/ft³, and the skins are assumed to be two layers of 1.4 oz/yd² fiberglass. For weight estimation the spar caps were assumed to be 1/4 inch wide and 0.030 inches thick. The final spar sizing will depend on the final weight, wing area, taper ratio and airfoil selection. As the spar weight is a minor portion of the overall wing weight, assuming a representative size was reasonable. Finally, an additional 10% is added to the total wing and tail weights to account for waterproofing, control surface mounting, and carry-through structure.

Five potential wing airfoils were selected that gave a good balance between $(L/D)_{max}$ and $C_{L_{max}}$. They are the S9075, SD7037, SD7043, SD7062, and the SG6042. Most of these were designed as low Reynolds number airfoils for use on model sailplanes. XFOIL was used to evaluate the drag and moment coefficients of each airfoil from a C_L of -0.1 up to $C_{L_{max}}$ and across a range of Reynolds numbers between 50,000 and 500,000 [61]. The transition location was left free and the N_{crit} parameter in XFOIL was set to 9. Figure 5.2 shows the computed drag polars for each of the five airfoils at a Reynolds number of 200,000.

The two tail airfoils considered were the NACA0008 and the S9027, both of which are symmetric sections. XFOIL was used to evaluate the drag and moment coefficients

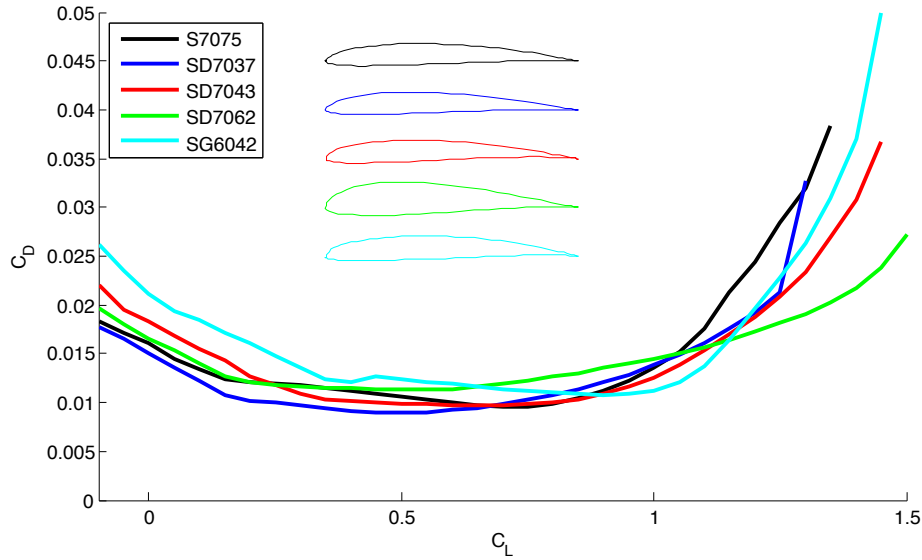


Figure 5.2: Drag polars for the five wing airfoils considered at a Reynolds number of 200,000.

of the airfoils over the C_L range of -0.7 to 0.7 and the Reynolds number range of 10,000 to 400,000. Drag polars for the two tail airfoils are shown at a Reynolds number of 100,000 in Fig. 5.3.

Each design was trimmed using AVL over a range of aircraft lift coefficients [62]. Outputs of interest included the loading of each panel and the induced drag of the airplane. With the local lift coefficient on each panel and the local chord Reynolds number, the profile drag of each wing and tail section could be interpolated from the airfoil database computed using XFOIL. The maximum aircraft lift coefficient was determined using the critical section method, where the maximum lift coefficient is achieved when any section of the wing first stalls. The profile drag of the fuselage was computed using handbook methods based on the fuselage Reynolds number, fineness ratio and wetted area. A 10% drag markup is added to the fuselage and lifting surface profile drag values to account for integration effects and other unmodeled drag sources. The resulting drag polar from adding the profile drag and induced drag over the achievable range of aircraft lift coefficients is then fit with a 4th order polynomial for use in the trajectory optimization routine. In all cases examined the 4th order polynomial provided a high quality fit over the allowable C_L range. The

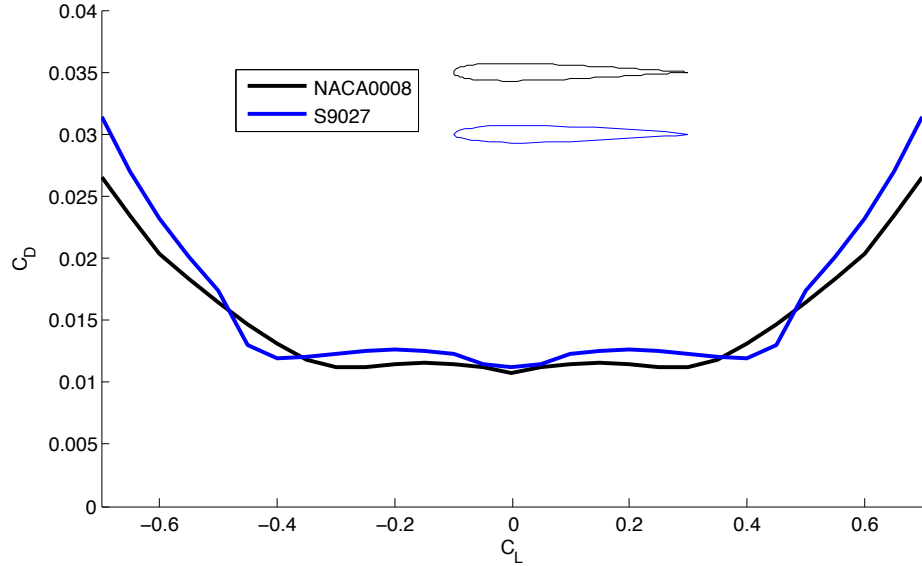


Figure 5.3: Drag polars for the two tail airfoils considered at a Reynolds number of 100,000.

computation time for one function evaluation was approximately 40 s, the majority of which was running AVL to trim the airplane across the range of allowable lift coefficients.

5.3.3 Sizing Results

As mentioned previously, the aircraft was sized using rational methods along with the help of random design space exploration and grid search. Initially, 200 random designs were evaluated to identify any trends in the resulting data. Figure 5.4 shows each of the designs plotted in the stall speed vs. required reference wind speed space. One thing to note is the relative flatness of the design space, each design has a required reference wind speed between roughly 8 and 10.5 m/s. A few trends were apparent in the data. First, all of the designs to the lower left of the plot used either the SD7037 or SD7043 airfoils. Trends of decreasing reference wind speed were observed for both higher aspect ratios and larger wing areas. The larger wing area designs were also the only ones to meet the stall speed constraint. The best performing designs overwhelmingly had taper ratios between 0.6 and 0.8.

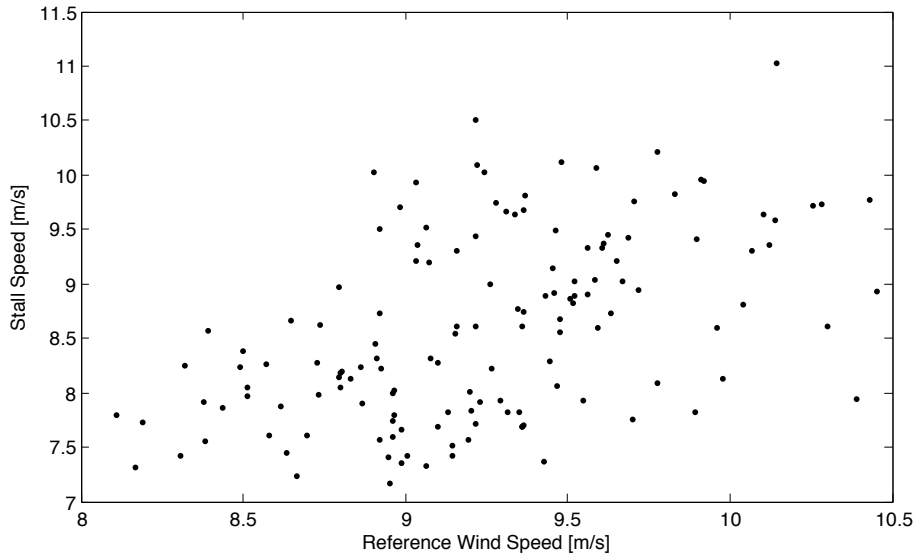


Figure 5.4: Scatterplot of the initial 200 random designs in the stall speed vs. required reference wind speed function space.

As expected, it was clear that the best performing designs were up against the wing span constraint of 2.5 m, collapsing the S and $\mathcal{A}R$ search to one dimension. Additionally, for a given taper ratio, the wing twist could be selected to give a reasonable lift distribution. Accordingly, the design variable ranges were refined as shown in Table 5.4 and another 200 random designs were evaluated. After examining the resulting performance of these designs, a two iteration grid search was conducted in the most promising region of the design space. The wing airfoil and tail airfoils were fixed as the SD7037 and NACA0008, respectively. The second grid search iteration focused around the best feasible design from the first iteration. Table 5.5 defines the grid used for each variable in the each iteration. In total, the grid search evaluated an additional 315 designs.

Figures 5.5 and 5.6 show the objective function value as a function of wing area and aspect ratio for the best performing designs that satisfied the stall and span constraints for each iteration of the grid search. Note the apparent noisiness of the objective function for relatively small changes in the design variable values, indicating why the use of a gradient based optimizer was avoided for this problem.

Table 5.4: Refined design variable bounds for the second random search of the design space. The wing airfoils considered for this search are: 2 - SD7037, 3 - SD7043. The tail airfoils are: 1 - NACA0008, 2 - S9027.

Design	Lower Bound	Upper Bound
S	0.3 m^2	0.5 m^2
\mathcal{R}	10	15
λ	0.6	0.8
θ_{tip}	-3°	-1°
Wing Airfoil	2	3
Tail Airfoil	1	2

Table 5.5: Design variable bounds and grid spacing for both steps of the grid search. The values for step one are before the / and the values for step two are after. The wing airfoil was fixed as the SD7037 and the tail airfoil as the NACA0008.

Design Variable Variable	Lower Bounds (iter 1 / iter 2)	Upper Bounds (iter 1 / iter 2)	Grid Spacing (iter 1 / iter 2)
S	$0.4 / 0.465 \text{ m}^2$	$0.5 / 0.485 \text{ m}^2$	$0.025 / 0.01 \text{ m}^2$
\mathcal{R}	$12 / 12.8$	$15 / 13.2$	$1 / 0.1$
λ	$0.65 / 0.625$	$0.75 / 0.675$	$0.05 / 0.025$
θ_{tip}	$-2^\circ / -1.6^\circ$	$-1^\circ / -1.4^\circ$	$0.5^\circ / 0.1^\circ$

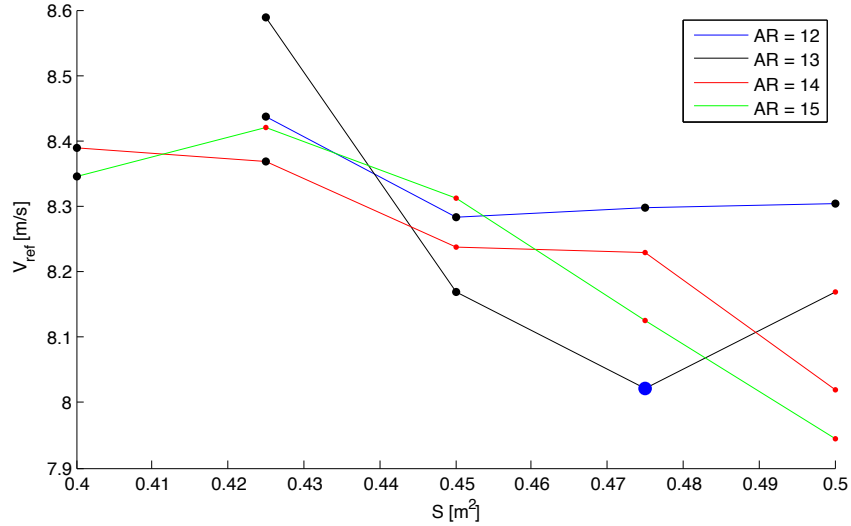


Figure 5.5: Plot showing the minimum required reference wind speed for the best designs as a function of S and $\mathcal{A}R$ for the first iteration of the grid search. Points indicate the analyzed designs, lines only used to indicate aspect ratio. Omitted points do not meet the stall speed constraint and the red dots indicate designs that exceed the span constraint. The blue dot indicates the best feasible design found.

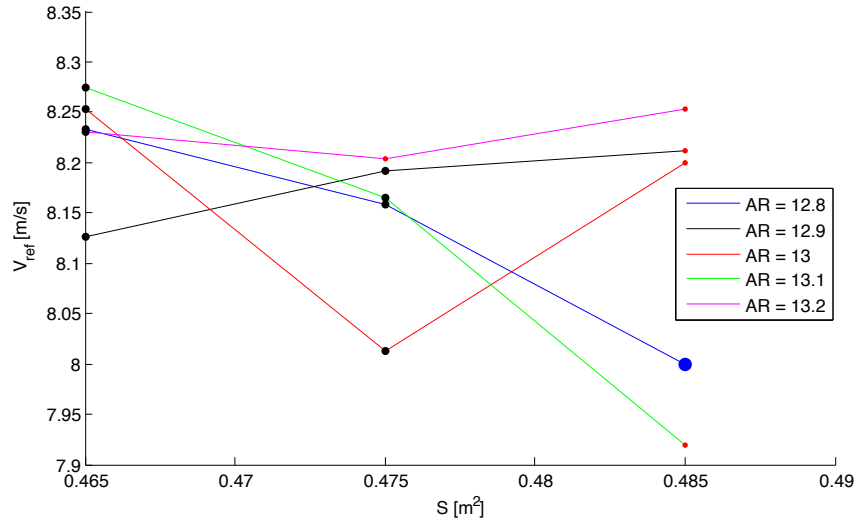


Figure 5.6: Plot showing the minimum required reference wind speed for the best designs as a function of S and $\mathcal{A}R$ for the second iteration of the grid search. Points indicate the analyzed designs, lines only used to indicate aspect ratio. The red dots indicate designs that exceed the span constraint. The blue dot indicates the best feasible design found.

The best performing design from the final grid search was selected for final control surface sizing. The best design has a wing area of 0.485 m^2 , an aspect ratio of 12.8, a taper ratio of 0.675, and a tip twist angle of -1.6° . The wing airfoil is the SD7037 and the tail airfoil is the NACA0008. The predicted mass is 1.99 kg and the wing span is 2.49 meters. The minimum required reference wind speed for the design is 8.01 m/s and the stall speed is 7.56 m/s.

5.4 Tail and Control Surface Sizing

In this section the tail surface sizes and fuselage length were varied to improve the dynamic modes throughout the design's speed range. The vehicle's moments of inertia were estimated in addition to the mass. The wing and tail surfaces were approximated as rectangular solids with dimensions equal to their span, mean chord, and average thickness. The fuselage was treated as a cylindrical shell and all electronic components were treated as point masses. The resulting inertias were $I_{xx} = 0.3782 \text{ kg} \cdot \text{m}^2$, $I_{yy} = 0.2963 \text{ kg} \cdot \text{m}^2$, $I_{zz} = 0.6552 \text{ kg} \cdot \text{m}^2$, and $I_{xz} = -0.01745 \text{ kg} \cdot \text{m}^2$.

After extensive hand tuning the fuselage length was decreased to 60% of the wingspan (1.5 m) and horizontal tail volume coefficient was increased to 0.6. These changes gave satisfactory longitudinal mode performance. The final horizontal tail has an area of 0.059 m^2 , an aspect ratio of 5, a span of 0.543 m, and a taper ratio of 0.6. The center of gravity was set to achieve a 5% static margin. The phugoid and short period modes were both stable throughout the entire C_L range. The root locus of the longitudinal modes is shown in Fig. 5.7 as a function of lift coefficient during steady gliding flight.

The vertical tail size was increased significantly above the baseline to a volume coefficient of 0.05, primarily to achieve sufficient control authority. This corresponds to an area of 0.0869 m^2 . The refined vertical tail has an aspect ratio of 1.7, a tail height of 0.384 m, and a taper ratio of 0.6. Throughout the speed range the airplane has a well damped dutch roll. The final design has a slightly unstable spiral mode. The time to double varies between about 40 s at $C_L = 0.18$ to about 5 s at $C_{L_{max}} = 1.17$. This was deemed acceptable as the closed loop control system should easily stabilize

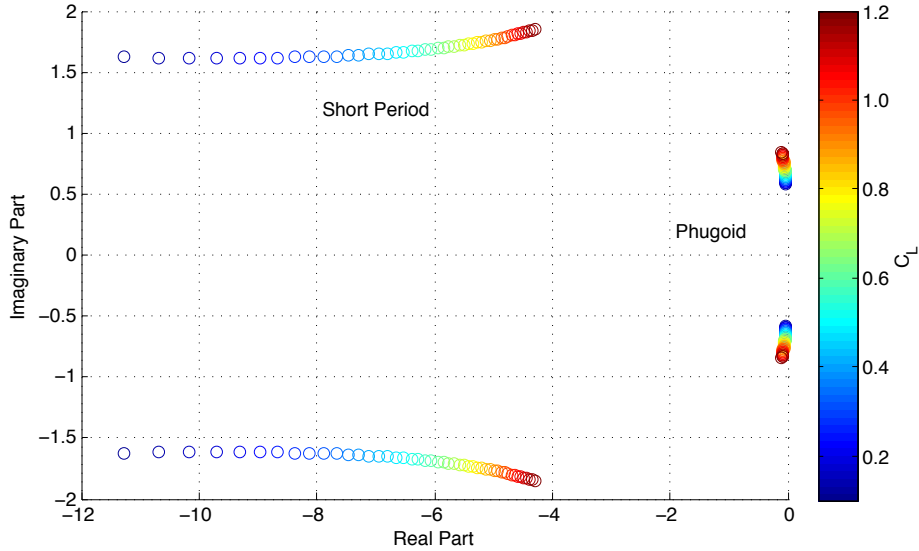


Figure 5.7: Root locus of longitudinal modes as lift coefficient varies for steady gliding flight.

this mode. The root locus of the lateral modes is shown in Fig. 5.8 as a function lift coefficient during steady gliding flight.

Next, the control surfaces were sized to ensure the aircraft can achieve the required body axis rates throughout the optimal dynamic soaring trajectory. The control surface deflections were limited to 10° for the elevator, 15° for the ailerons, and 25° for the rudder.

At each of the control points along the optimal trajectory the stability axis roll, pitch, and yaw rates were computed. For a quasi-steady controllability analysis, AVL was run at each of the corresponding flight conditions to compute the required control surface deflections to achieve the required body rates. Overall, the maximum pitch, roll, and yaw rates throughout the trajectory were all around $90^\circ/s$. Figure 5.9 shows the dimensional and non-dimensional stability axis rates required by the optimal trajectory. In order to assume quasi-steady flight the non-dimensional rates should remain below roughly 0.1, 0.03, and 0.25 for pitch, roll, and yaw, respectively. The required roll and yaw rates do exceed these bounds for a short portions of the trajectory, so further studies should look at unsteady aerodynamic effects at these times. For the selected control surface sizes, given in Table 5.6, the corresponding

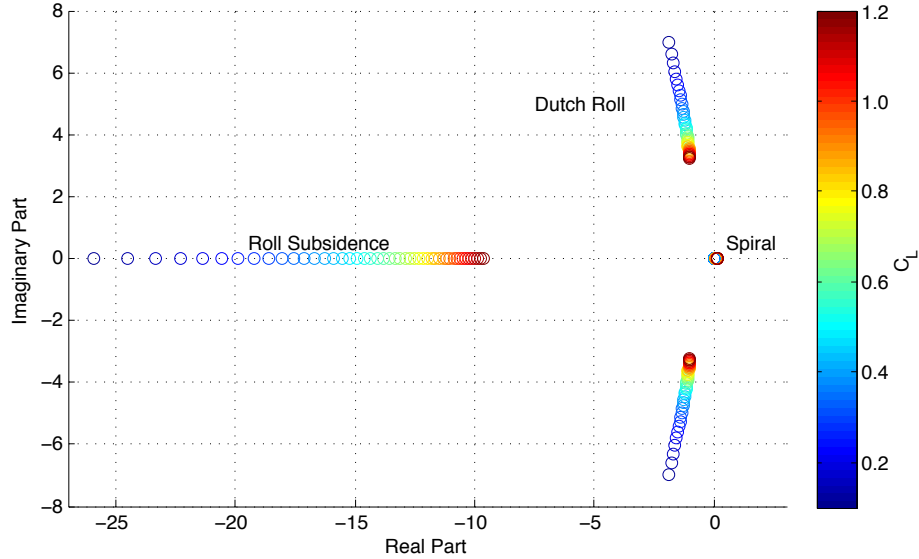


Figure 5.8: Root locus of lateral modes as lift coefficient varies for steady gliding flight.

control surface deflections are shown in Fig. 5.10. The elevator deflections required to trim in steady gliding flight across a range of lift coefficients are also shown in Fig. 5.11.

Table 5.6: Final control surface sizes.

Surface	% Span	% Chord at Root	% Chord at Tip
Elevator	100	40	40
Aileron	90	35	35
Rudder	100	50	66.6

5.5 Final Design

A rendering of the final *Mariner* design is shown in Fig. 5.12 with the location of many onboard systems indicated. A final mass breakdown is given in Table 5.7. The drag polar for the airplane in straight gliding flight is shown Fig. 5.13. The maximum lift-to-drag ratio is 20.5 at a speed of 9.34 m/s and a C_L of 0.75. The corresponding

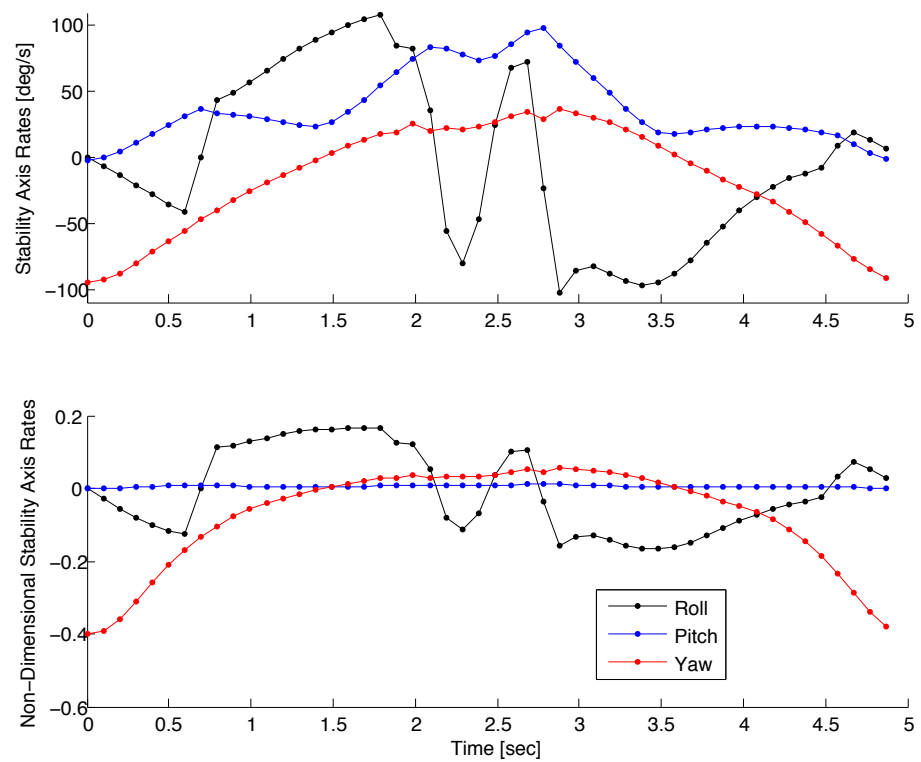


Figure 5.9: Required stability axis rates for the minimum reference wind speed trajectory.

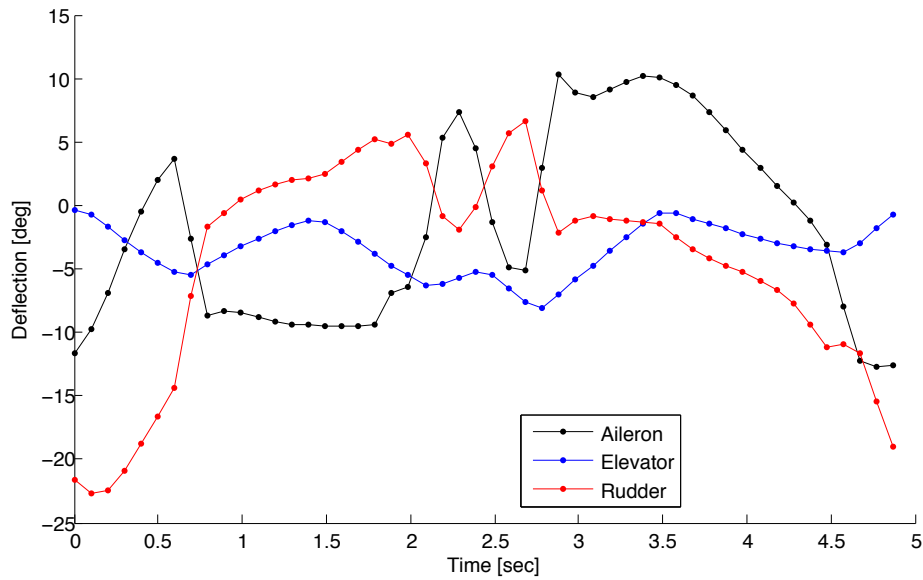


Figure 5.10: Predicted control surface deflections to achieve the required stability axis rates throughout the optimal dynamic soaring trajectory.

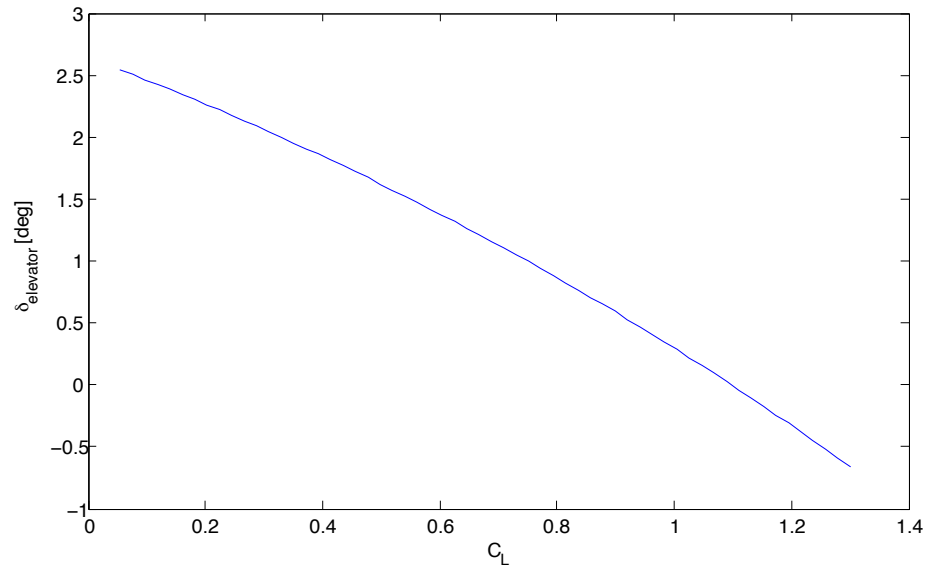


Figure 5.11: Elevator deflections to trim for steady gliding flight as a function of lift coefficient with a 5% static margin.

velocity hodograph is shown in Fig. 5.14. The minimum sink rate in still air is approximately 0.42 m/s at an airspeed of 8.03 m/s and $C_L = 1.01$. The stall speed is 7.47 m/s at $C_{L_{max}} = 1.17$.

Details of the minimum reference wind speed dynamic soaring trajectory are shown in Figs. 5.15 to 5.18. The minimum required reference wind speed is 8.01 m/s. The maximum altitude reached is 11.73 m and airspeed varies between 5.12 m/s and 15.37 m/s. As a reminder the wingtip maintains at least 0.5 m separation from the surface. In addition, the maximum roll angle is limited to 60° and the maximum roll rate to 90°/s. The maximum C_L rate is 0.5 s⁻¹. The cycle time for the optimum trajectory is 4.97 s. Each cycle covers a net distance of 48.7 m in a direction 45° off from the wind direction.

It is interesting to note how the minimum required reference wind speed changes if the mass of the vehicle were different by an order of magnitude in either direction. For this example, all other trajectory optimization inputs were kept constant except the wing area and span, which were varied to maintain a constant wing loading and aspect ratio. Other parameters would surely change with vehicle size, but these effects are ignored for this quick analysis. If the vehicle had a mass of 20 kg, the minimum required reference wind speed would be 10.33 m/s. Meanwhile if it has a mass of only 200 g, the minimum required reference wind speed would be 4.87 m/s. This indicates that a decade ago, it would have been much more difficult to build a dynamic soaring UAV, as sensors and flight computers were significantly heavier. However, in the future, further reductions in component weights will allow for smaller demonstration vehicles that can fly in even lighter winds.

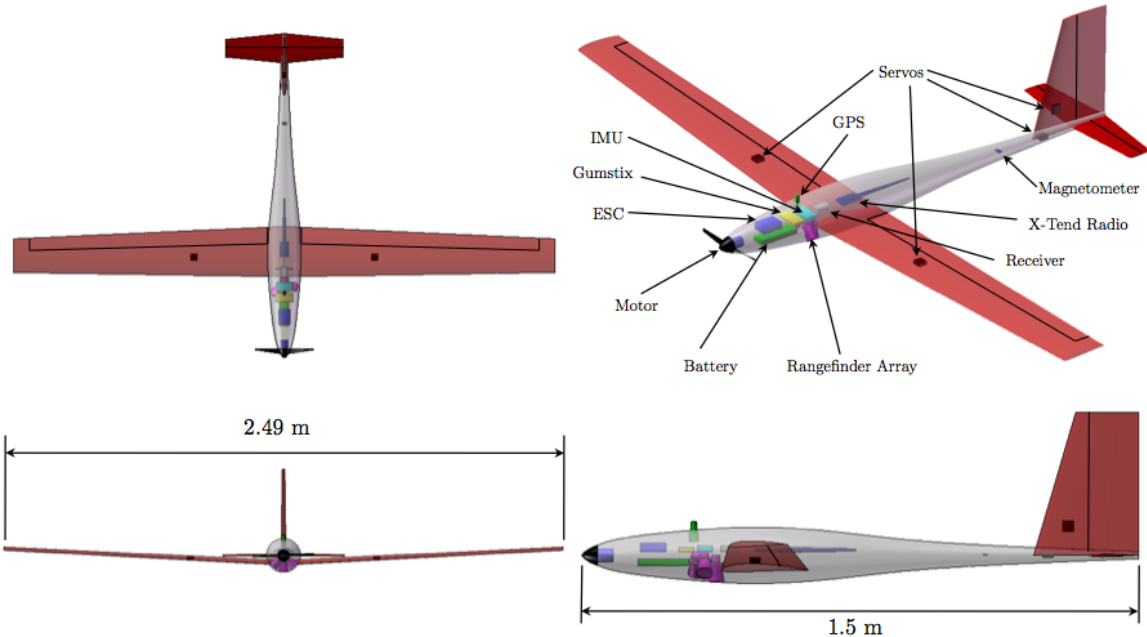


Figure 5.12: A Solidworks rendering of *Mariner* showing the critical dimensions and the location of major internal components.

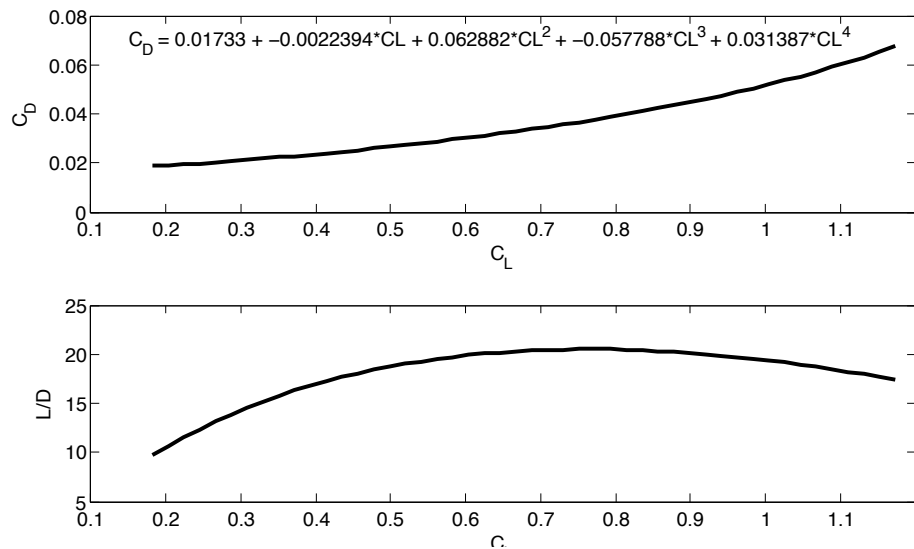


Figure 5.13: Drag polar for *Mariner* during straight gliding flight and (L/D) as a function of lift coefficient

Table 5.7: Mass breakdown of *Mariner* including the weights of each electronic component and major structural parts.

Component	Mass [g]
Motor	135
Propeller and Spinner	45
ESC	110
Battery	250
Servos (4)	100
Receiver	15
Flight computer	20
IMU and Pressure Sensors	15
Magnetometer	1
GPS	15
Telemetry Radio and antenna	40
Ultrasonic Rangefinders	150
Camera	35
Wing	451.9
Wing Core	185.2
Wing Spar	38.7
Wing Skins	186.9
Wing Miscellaneous	41.1
Horizontal Tail	34.2
Horizontal Tail Core	8.5
Horizontal Tail Skins	22.6
Horizontal Tail Miscellaneous	3.1
Vertical Tail	77.4
Vertical Tail Core	37.1
Vertical Tail Skins	33.3
Vertical Tail Miscellaneous	7
Fuselage Structure	491.8
Fuselage Skin	148.3
Fuselage Floor	84.9
Fuselage Frames	176.7
Fuselage Miscellaneous	81.9
Total	1986.3

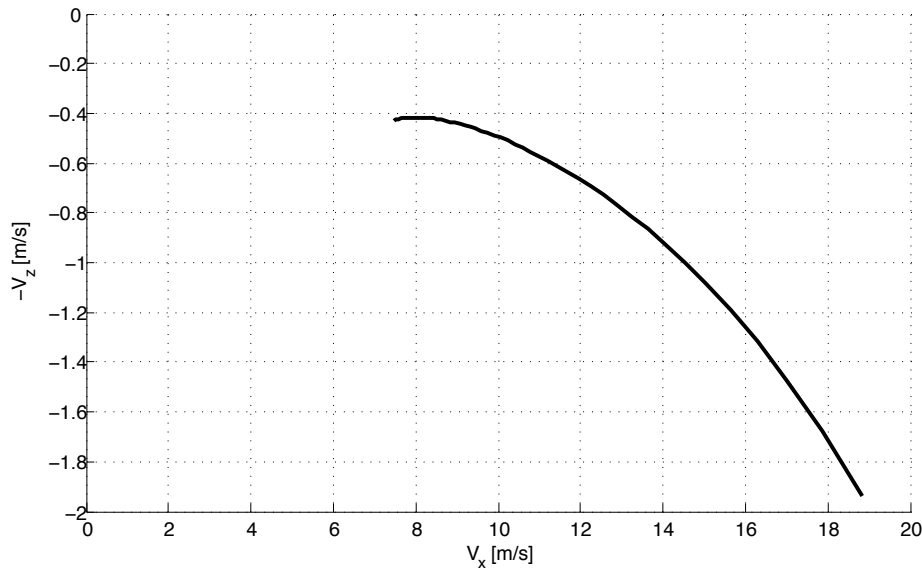


Figure 5.14: Velocity hodograph for *Mariner* in straight gliding flight.

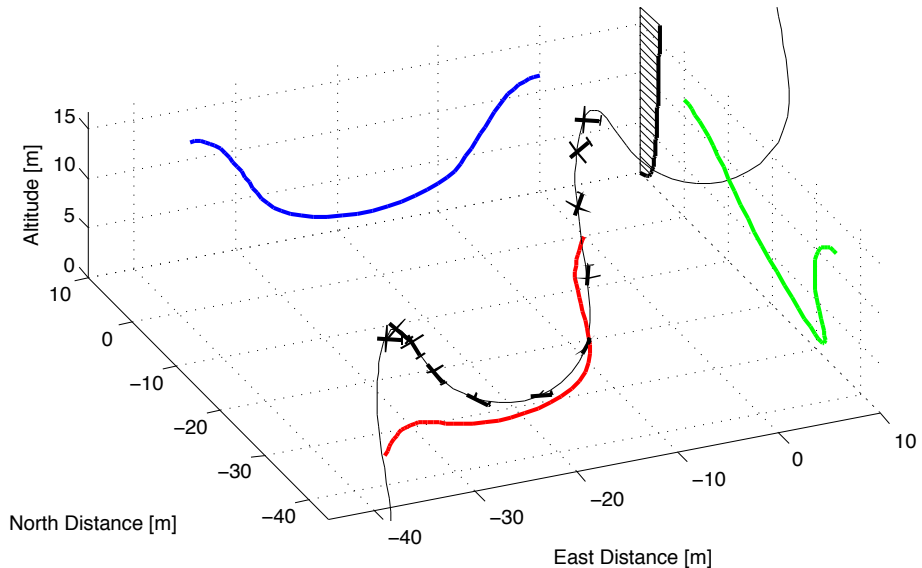


Figure 5.15: The minimum reference wind speed trajectory for *Mariner* assuming $z_{tip_{max}} = 0.5$ m, $\phi_{max} = 60^\circ$, $(\frac{\partial \phi}{\partial t})_{max} = 90^\circ/s$, $(\frac{\partial C_L}{\partial t})_{max} = 0.5$ s $^{-1}$, and $n_{max} = 3$.

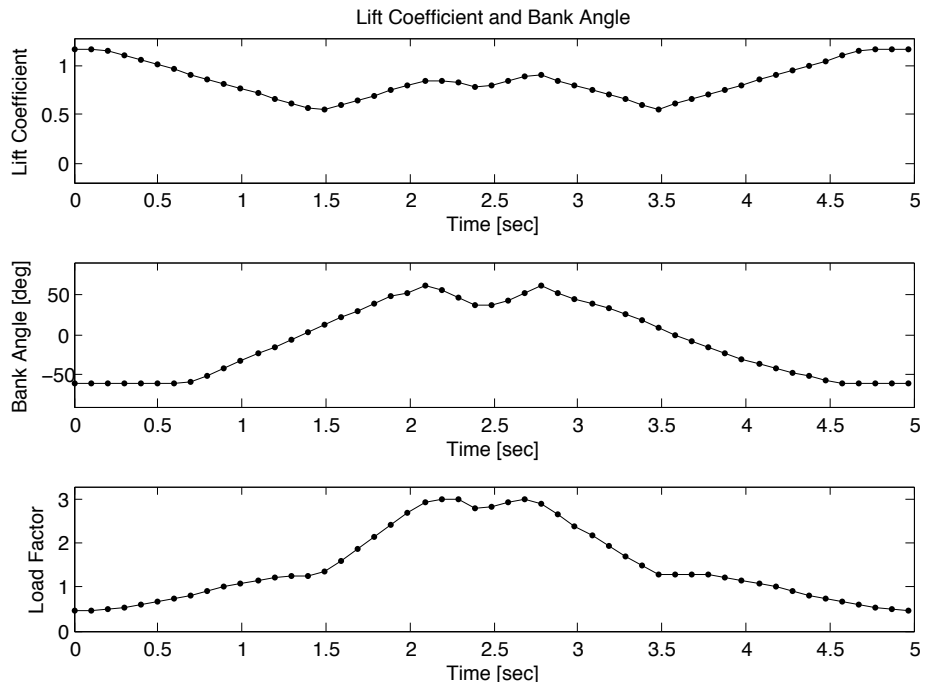


Figure 5.16: The lift coefficient, bank angle, and load factor for the minimum reference wind speed trajectory for *Mariner* assuming $z_{tip_{max}} = 0.5\text{ m}$, $\phi_{max} = 60^\circ$, $(\frac{\partial \phi}{\partial t})_{max} = 90^\circ/\text{s}$, $(\frac{\partial C_L}{\partial t})_{max} = 0.5\text{ s}^{-1}$, and $n_{max} = 3$.

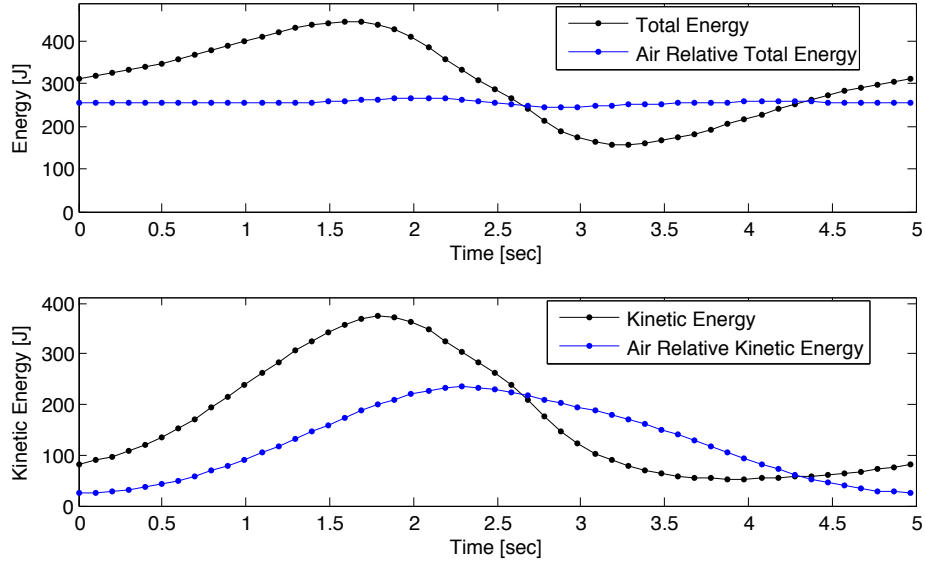


Figure 5.17: The total energy and air relative total energy for the minimum reference wind speed trajectory for *Mariner* assuming $z_{tipmax} = 0.5\text{ m}$, $\phi_{max} = 60^\circ$, $(\frac{\partial\phi}{\partial t})_{max} = 90^\circ/\text{s}$, $(\frac{\partial C_L}{\partial t})_{max} = 0.5\text{ s}^{-1}$, and $n_{max} = 3$.

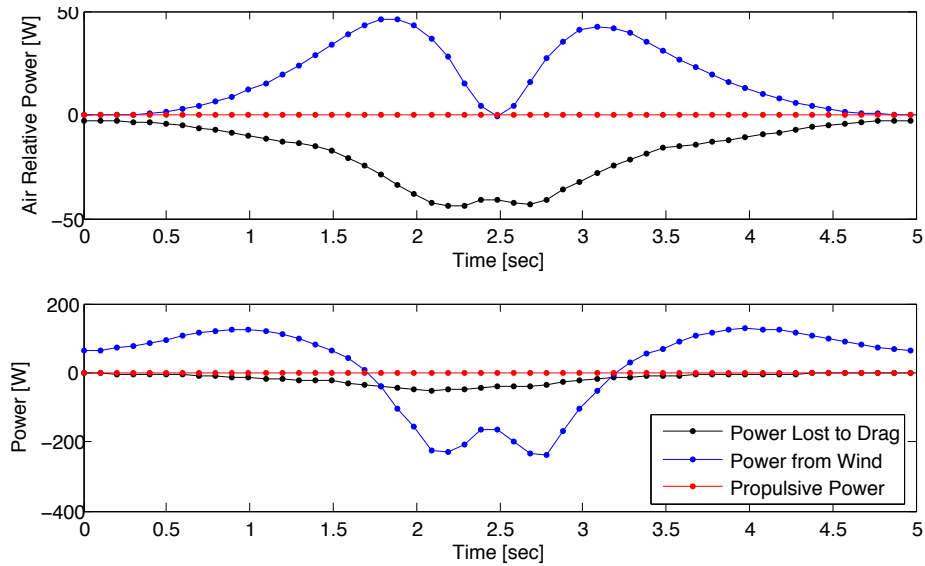


Figure 5.18: The power lost due to drag and extracted from the winds for the minimum reference wind speed trajectory for *Mariner* assuming $z_{tipmax} = 0.5\text{ m}$, $\phi_{max} = 60^\circ$, $(\frac{\partial\phi}{\partial t})_{max} = 90^\circ/\text{s}$, $(\frac{\partial C_L}{\partial t})_{max} = 0.5\text{ s}^{-1}$, and $n_{max} = 3$.

Chapter 6

Experimental Validation

This chapter describes some of the steps taken towards experimental validation of the dynamic soaring trajectory optimization analysis and the dynamic soaring UAV design. Details are given of a tracking tag designed to measure the dynamic soaring maneuvers of albatross with GPS and an inertial measurement unit for comparison to trajectory results presented previously. The sensors included on these tracking tags are similar to those specified for the *Mariner* demonstrator, with the exception of the height above ground sensors. Additionally, a small almost-ready-to-fly remote control glider was purchased and outfit with the *Mariner* flight computer and sensors to allow development of the flight control software before constructing the final design.

A common link between the albatross tracker and the UAV flight control software is a need to fuse the sensor measurements together to provide an accurate estimate of the bird or UAV's position and orientation. In this work, an extended Kalman filter (EKF) is used as the data fusion algorithm. The EKF process model and measurement models are described in detail. Selected experimental results are presented from flight tests on the development UAV where the EKF estimates of the pitch and roll orientation are compared to independent values measured by detecting the horizon in onboard video.

6.1 Albatross Tracker

When first exploring the dynamic soaring literature, it became clear that there was a lack of fine temporal measurements of the dynamic soaring trajectories flown by albatross and other large seabirds. Many tracking studies had been conducted using GPS loggers [63, 64, 65, 66, 67], ARGOS satellite transmitters [68, 69], light level loggers [12, 70, 71], and combinations of these methods [72, 73, 74, 75]. Optical measurements of dynamic soaring trajectories have also been conducted from ships [36]. At best, all of these methods only reveal the flight tracks of the birds with samples once a second (most use much lower sampling frequencies). To compare with trajectory optimization results, a much finer temporal resolution is desired along with measurements of the bird's orientation.

With modern electronics such as MEMS inertial sensors, miniature GPS modules, and flash memory in mind, it was determined that a new tracking tag that could measure the location and orientation of an albatross at a much higher rate could be designed and built at low cost. After talking to a biologist that has worked on tracking albatrosses for the last decade, a preliminary set of requirements were determined. The primary requirement was that for extended use, the tags are desired to have a mass less than 2% of the bird's mass, so as not to negatively affect their performance. Of the albatross species that our collaborating biologist works with, the smallest is the Laysan Albatross, whose lightest adults weight approximately 2.5 kg. To achieve the 2% body mass target the tracking tag needed to weigh 50 g or less. The tags are attached to the birds by taping them to the feathers between their shoulder blades. An additional requirement included waterproofing the trackers, since many albatross species may dive up to a depth of a few meters while feeding. It was also desirable that the tags operate for the duration of each bird's flight, which during the planned deployment periods may be up to one week.

After developing this tracker, the high resolution GPS tagging work by Sachs, et. al. was published [76]. This tag achieves similar relative positioning accuracy through the use of carrier phase GPS, however there is no capability to directly measure the bird's orientation or local environmental properties. The tag is also

significantly heavier at 107 g , and therefore is not suitable for tracking some of the smaller albatross species.

6.1.1 Design

With the stated goal of estimating the orientation and position of a bird throughout a dynamic soaring trajectory, the following sensors were selected: GPS, 3-axis MEMS accelerometer, 3-axis MEMS rate gyro, and 3-axis MEMS magnetometer. Additionally, by using barometric and differential pressure sensors the altitude measurement is improved and the airspeed may be estimated. With measurements of the airspeed, inertial speed (from GPS), and orientation of the bird, it is possible to estimate the wind velocities [77]. A dsPIC microcontroller (dsPIC33FJ128GP204) is used to communicate with the sensors, record the raw data to a μ SD card, and to manage the operation of the tracker.

The MediaTek MT-3229 GPS module was selected for its small size (16x16x6 mm), low mass (6 g), ability to provide position updates at up to 10 Hz, and power control features. The module communicates with the microcontroller through a UART serial port.

The selected accelerometer was the Analog Devices ADXL345 which was configured to provide 3-axis acceleration measurements at 50 Hz with 13-bit resolution over the range of ± 16 g's. The accelerometer communicates with the microcontroller over an I²C bus.

Two chips are used for the rate gyros, the STMicroelectronics LPR530AL for the roll and pitch axes and the LY530ALH for the yaw axis. Both of these gyros output analog signals proportional to the angular rates up to $\pm 300^\circ/sec$. The 12-bit analog-to-digital converter on the microcontroller is used to sample the analog gyro signal at approximately 2000 Hz. The signal is oversampled and averaged to provide a 50 Hz output signal that is saved to the μ SD card.

The Honeywell HMC5843 3-axis magnetometer is used to measure the local magnetic field direction and strength. It was configured to output 12-bit measurements of the magnetic field strengths at 50 Hz. The output range was set to ± 1.0 Gauss.

The magnetometer also communicates with the microcontroller over the I²C bus.

The final sensor was the SCP1000-D11 digital pressure and temperature sensor. Two were included, one to measure barometric pressure and one to measure the total pressure. Ideally, a single differential pressure sensor would be used for measuring the airspeed. Unfortunately, no differential pressure sensors with sufficient sensitivity that operated at 3.3V were available at the time of the design. Instead, two absolute pressure sensors were used and the difference between the total and static measurements were used as an estimate of the dynamic pressure. Both of these sensors were configured to sample at their maximum rate of approximately 10 Hz. They output a 15-bit measurement of pressure (3 Pa resolution) and a 14-bit measurement of temperature (0.2°C resolution). The pressure sensors communicate with the microcontroller over the I²C bus. Another desirable feature of these pressure sensors was the rubber gasket available for mounting the sensor. The pressure sensing die is designed to be exposed to the elements, but the side of the sensor that mounts to the PCB is not. The gasket allows PCB side of the sensor to be sealed inside the enclosure, while the pressure element remains exposed.

A lightweight 2.4 GHz XBee®-Pro radio was also included on the tracker to allow the user to change settings during initialization without a physical connection. The radio also allows the tracker to notify the operator when the bird has returned to the nest after its flight so that it may be retrieved.

A waterproof ABS plastic box was designed to house the tracker PCB board, pressure sensors and battery. The box top has a groove with a 1/16" diameter O-ring that provides a seal when it is attached to the rest of the box with four stainless steel screws. There are two ports in the sides of the box that the pressure sensor gaskets snugly fit into. The static pressure port is along one of the long sides and is designed to be under the feathers when taped to the bird. The objective was to locate it in an environment without significant flow in order to provide a consistent static pressure for measuring altitude. The total pressure port is located on the front of the box and mounts into a small plastic block with a 1/8" diameter, 2" long piece of soft nylon tubing that acts as a pitot tube. The pitot tube is easily removable if they are deemed to present a hazard to the birds.

For power the tracker uses a single cell Lithium Polymer battery with a nominal voltage of 3.7 V. An off-the-shelf Nokia cell phone battery (BL-4C) was selected for its wide availability and its internal protection circuitry. This eliminated the need for careful battery monitoring and added a degree of protection by preventing deep discharge of the battery during operation. The battery weighs about 16 g and nominally has a capacity of about 860 mAh. With all of the sensors operating at their full data rate the current draw is on the order of 170 mA, indicating a usable battery life on the order of 5 hours. With all of the sensors and peripherals in sleep mode the current draw is on the order of 2 mA, allowing a standby battery life of about 14 days. To manage the limited battery energy a state machine was developed to operate the various sensors only when desired.

State Machine

The primary objective when designing the state machine was to use as much of the battery energy as possible for recording high resolution GPS and IMU data while the bird is dynamic soaring, and not while it is sitting at its nest or on the water. It was also highly desirable to obtain occasional position fixes throughout the flight to map the overall trajectories. Finally, it was beneficial for the battery to save enough energy in reserve so that the XBee®-Pro radio could notify a ground station that the bird had returned to its nest.

The final state machine had four states that the tracker transitions between, GET-GPS, WAIT, HOME, and RECORD. There are a number of user defined parameters that dictate the specific state transition behaviors of the tracker. These parameters and their default values are given in Table 6.1. The state machine is shown schematically in Fig. 6.1. Figure 6.2 illustrates the state machine behavior after getting a GPS lock in the GETGPS state. With the default settings the tracker has a battery life of about 4 days and will obtain over 3 hours of high resolution data and location fixes once an hour.

After initialization the tracker enters the GETGPS state. In this state the GPS is set to a 1 Hz output rate and all of the other sensors are in their sleep states. If a GPS lock is obtained within the allowed time (T_{getgps}), the position is written to a

Table 6.1: User definable parameters for the tracker that govern the state machine operation along with their default values.

Parameter Name	Symbol	Default Value	Units
Home Latitude	HOMELAT	23.86849	deg
Home Longitude	HOMELON	-166.28690	deg
Transmit Distance	$D_{transmit}$	1000	m
Record Distance	D_{record}	10000	m
Velocity Threshold	$Speed_{threshold}$	2	m/s
Velocity Time Threshold	T_{speed}	0.5	min
Voltage Threshold	$V_{threshold}$	3.75	Volts
WAIT Time Threshold	T_{wait}	60	min
GETGPS Time Threshold	T_{getgps}	2	min
RECORD Time Threshold	T_{record}	5	min
HOME Time Threshold	T_{home}	1	min

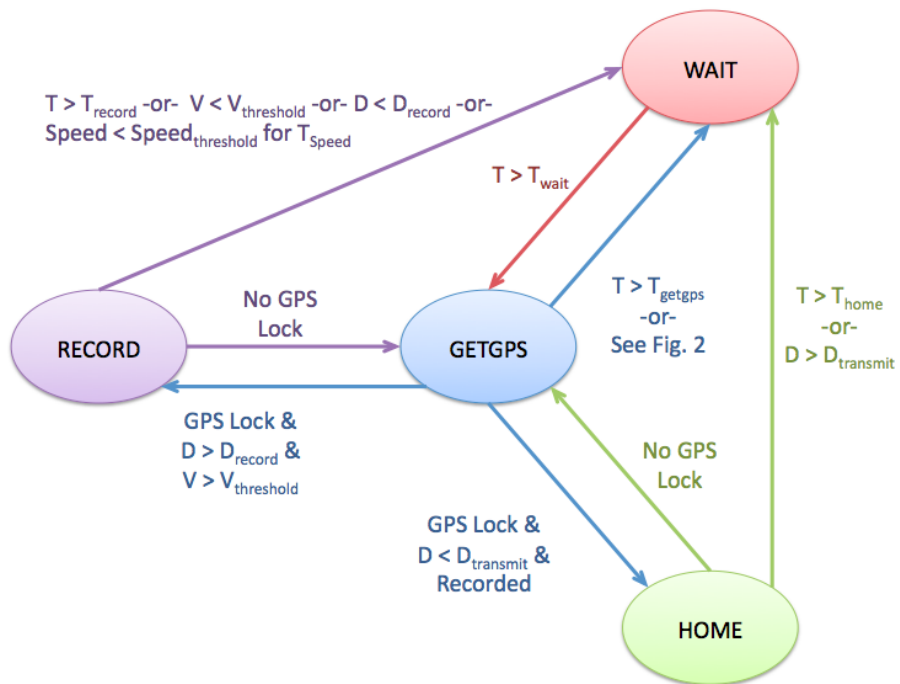


Figure 6.1: Finite state machine governing the operation of the tracker.

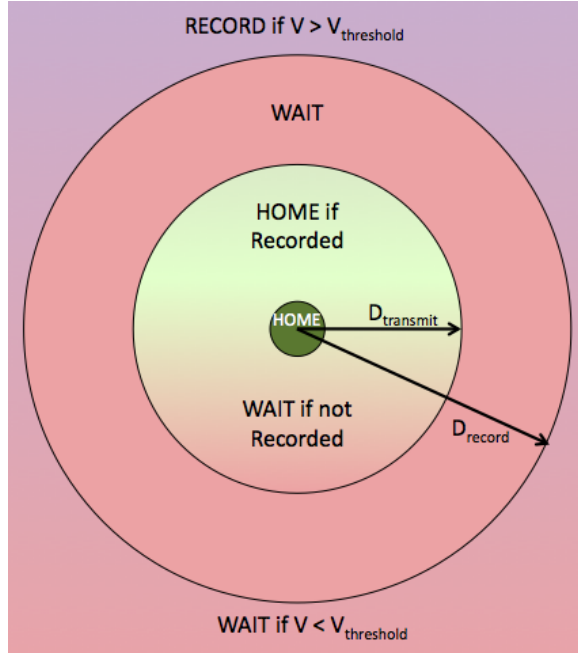


Figure 6.2: State machine logic when transitioning from the GETGPS state based on the distance from the defined home location.

file, the distance from the tracker to the home location is calculated, and the voltage is checked. If the distance from the home location is between the transmit distance threshold and the record distance threshold, then the tracker transitions to the WAIT state. If the distance is less than the transmit distance threshold, then it will enter the HOME state so long as it has previously been in the RECORD state, otherwise it transitions to the WAIT state. This was done as there is no need to inform the user that the bird is in the vicinity of the home location if it has never left. If the distance is greater than the record distance threshold, then the tracker will enter the RECORD state, so long as the battery voltage is greater than the voltage threshold, otherwise it transitions to the WAIT state.

In the WAIT state all of the sensors and peripherals are in their low power sleep mode. After waiting the specified time (T_{wait}), the microcontroller wakes up and transitions to the GETGPS state.

In the RECORD state all of the sensors are operating at their maximum data rates (10 Hz for GPS, 50 Hz for gyros, accelerometers and magnetometers, 10 Hz for

pressure sensors) and information is saved to binary files on the μ SD card. If GPS lock is lost the tracker returns to the GETGPS state. The tracker transitions from RECORD to WAIT if any of the following conditions are met:

- The voltage is less than the threshold voltage ($V_{threshold}$)
- The distance to the home location is less than the record distance threshold (D_{record})
- The velocity is less than the threshold velocity ($Speed_{threshold}$) for the velocity time threshold (T_{speed})
- The maximum recording time (T_{record}) is reached

In the HOME state the GPS operates at 1 Hz and the tracker periodically transmits position information to the ground station over the XBee®-Pro radio. If GPS lock is lost it transitions back to the GETGPS state. If the distance exceeds the transmit threshold distance or the maximum time in the HOME state (T_{home}) is reached, then the tracker transitions to the WAIT state.

Final Design

After numerous hardware and software iterations, parts for the final tracker design were ordered and the PCB boards were populated. A total of 6 trackers were completed, with spares to potentially construct two more. A CAD model of the box showing the location of the PCB, pressure sensors and battery is shown in Fig. 6.3. The final schematic and board layout are shown in Figs. 6.4 and 6.5. A picture of a fully assembled tracker is shown in Fig. 6.6. A view of the tracker with the top off is shown in Fig. 6.7, revealing the μ SD card.

6.1.2 Calibration

Low cost inertial sensors are known to have significant offset, alignment, and scale factor errors [78]. In addition to these error sources, magnetometers are also subject to hard and soft iron distortions. Hard iron distortions add or subtract from the

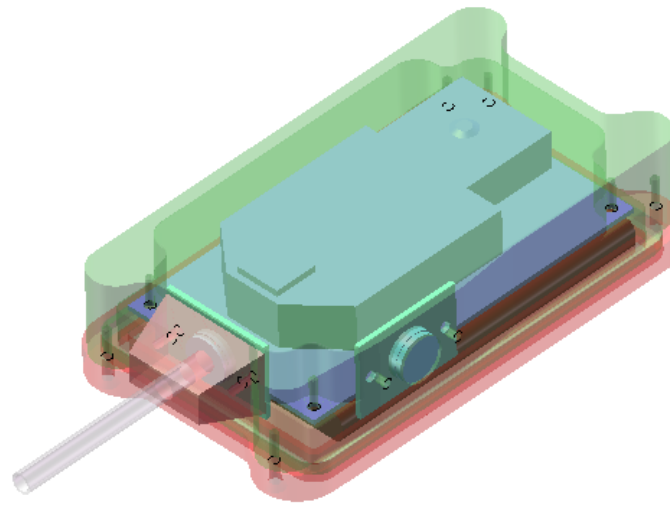


Figure 6.3: CAD model of the tracker showing the box, PCB board, pressures sensors, and battery.

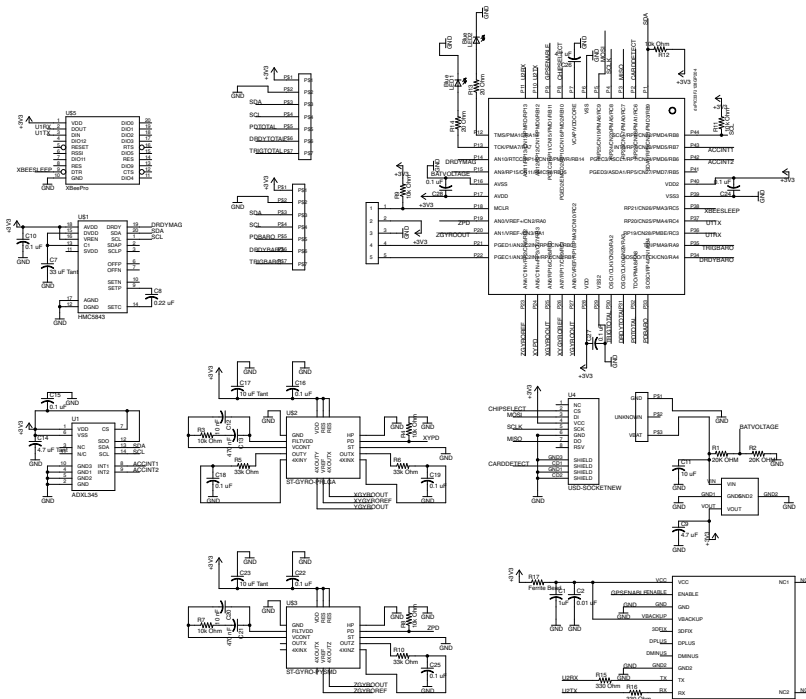
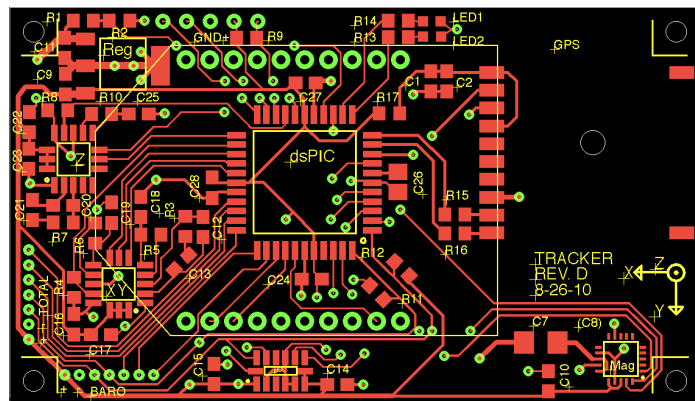
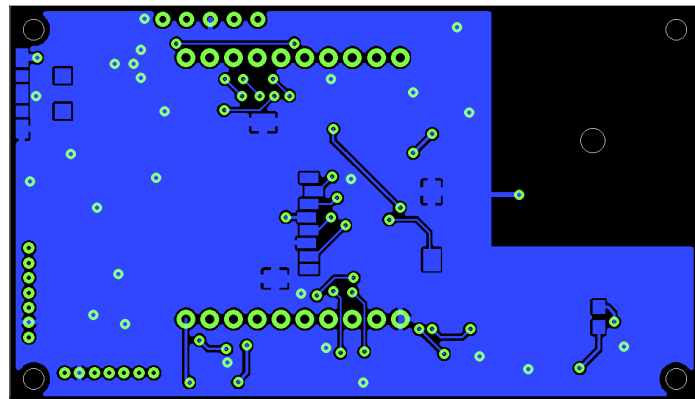


Figure 6.4: Electrical schematic of the final tracker PCB board.



(a) PCB Board Top



(b) PCB Board Bottom

Figure 6.5: Top and bottom PCB layouts for the final tracker design.



Figure 6.6: Picture of a fully assembled albatross tracker.



Figure 6.7: Picture of the final albatross track with the box top off and the battery removed, revealing the μ SD card and PCB board.

local field strength, and if fixed in the body frame of the magnetometer they are indistinguishable from the offset errors. Soft iron distorts the shape of the local magnetic field, and if fixed in the body frame they show up as alignment and scale factor errors. Fortunately, the birds do not have any significant sources of hard or soft iron, so these errors can be calibrated out of the sensors in the lab. During initial testing it was noted that the batteries do contribute significant hard and soft iron distortions and that they vary from one battery to the next. For this reason each tracker was assigned matching battery that was used for calibration and all later operations. MEMS rate gyros are known to have fairly significant time varying offset biases, which are particularly susceptible to temperature variations. Even without significant temperature variations the gyros have exhibited drift rates up to 1° per minute.

The magnetometer, accelerometer and rate gyros were calibrated using the method outlined in Ref. [79]. The basic method is to identify a known reference vector for the sensor (gravity for accelerometer, the true magnetic field for the magnetometers, a constant rate turntable for the rate gyros), and to rotate the sensor to many different orientations with respect to the reference vector. Assuming the only errors are offset, alignment and scale factors, the resulting measurements will map out the surface of an ellipsoid in the measurement space. If properly calibrated, the sensors should

map out the surface of sphere centered at the origin. The calibration procedure determines the scale factors, offsets and rotations required to map the surface of the raw measurement ellipsoid to the true measurement sphere. There is a remaining ambiguity in the orientation of the sensor axes with respect to the body frame that is resolved by placing the tracker in at least three orthogonal positions where the components of the true field strength are accurately known.

Once calibrated, the magnetometer biases, rotations, and scale factors are assumed to be constant and were programmed onto the trackers for later use. The accelerometer and gyro alignment errors and scale factors were assumed to be constant, however, the biases were assumed to slowly drift. As detailed in the next section, the EKF has additional states to track the accelerometer and gyro offset biases.

Details of the calibration equations are not presented in the interest of brevity, see Ref. [79] for the details. However, as an example, the steps in the magnetometer calibration are shown graphically for one of the trackers. Figure 6.8 shows the 3-axis magnetic field strengths measured as the orientation of the tracker is varied. Note the eccentricity of the ellipsoid and the large offset from the origin. Figure 6.9 shows the same sensor measurements after calibration when transformed into the body frame. In this case the final calibration equations are given by Eq. 6.1 which change the raw measurements in terms of analog-to-digital bits to μT . Once the calibration is complete, it is also possible to characterize the sensor noise. A histogram of the sensor error from the sphere is plotted in Fig. 6.10. Note the Gaussian shape to the histogram, making our assumption of Gaussian sensor noise discussed in the next section reasonable for the MEMS sensors.

$$\begin{bmatrix} M_{x_{true}} \\ M_{y_{true}} \\ M_{z_{true}} \end{bmatrix} = \begin{bmatrix} 0.0754 & 0.0046 & -0.0003 \\ -0.0040 & -0.0691 & -0.0006 \\ 0.0001 & -0.0009 & -0.0774 \end{bmatrix} \times \left(\begin{bmatrix} M_{x_{meas}} \\ M_{y_{meas}} \\ M_{z_{meas}} \end{bmatrix} - \begin{bmatrix} -70.07 \\ 121.45 \\ -198.90 \end{bmatrix} \right) \quad (6.1)$$

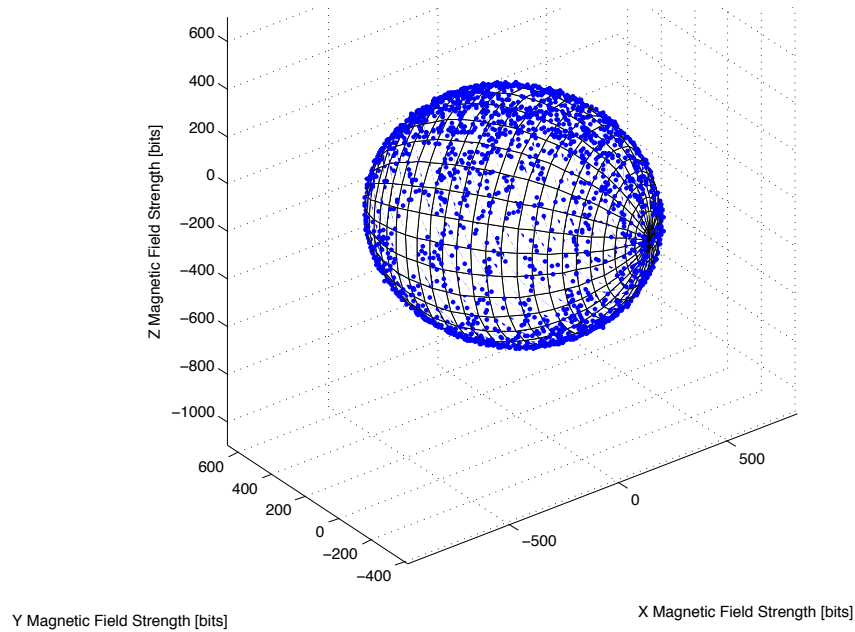


Figure 6.8: Raw magnetometer measurements as the tracker is rotated through many different orientations during calibration. The best fit ellipsoid is also shown.

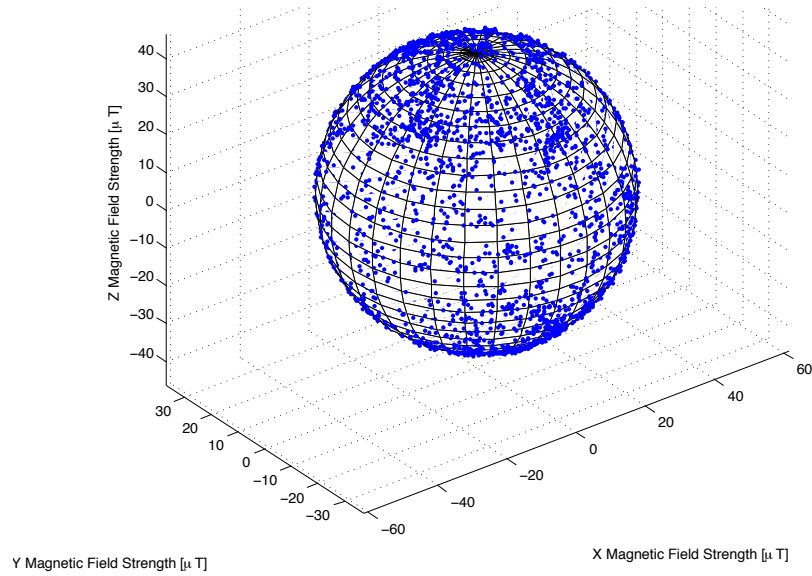


Figure 6.9: The raw magnetometer measurements after transformation to the calibration frame. Note how the mean measurement ellipsoid is now a sphere centered at the origin.

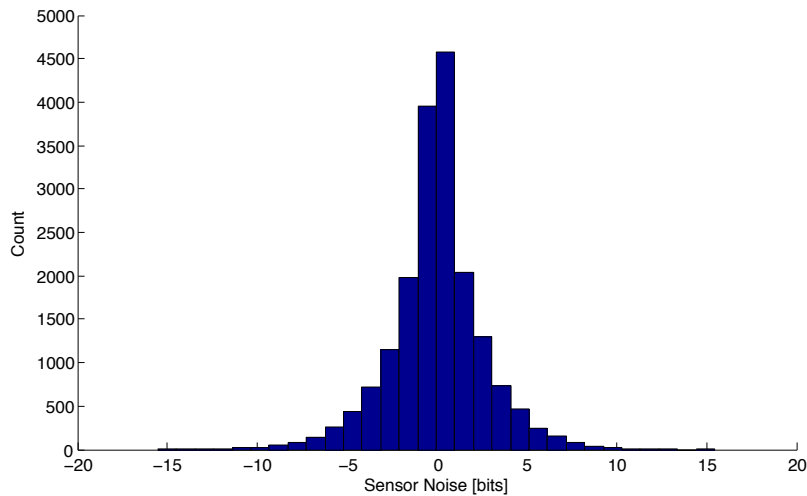


Figure 6.10: Histogram of magnetometer errors. Note the Gaussian shape of the distribution with a standard deviation of 2.5 bits.

6.1.3 Deployment

Six trackers were assembled in late 2010. All six were deployed to Tern Island in the French Frigate Shoals in Northwestern Hawaiian Islands in early 2011. The plan was to track Laysan and Black-footed Albatross during one to five day long foraging flights in the early winter. Unfortunately, unrelated permitting issues were encountered and no flight data was obtained before the publication of this thesis.

The plan going forward is to deploy three trackers to the Mozambique channel in order to track Great Frigatebirds. These large seabirds travel long distances by thermalling over the ocean throughout the tropics. They have the lowest wing loading of all known bird species. At the end of 2011 and early in 2012 the trackers will be deployed for tagging albatross. All six of the trackers will be deployed to the Southern Ocean for placement on Black-Browed and Wandering Albatrosses.

These loggers are expected to return a significant amount of data that can be used by both biologists and engineers to examine the energetics of dynamic soaring. Some of the interesting questions that may be answered include:

- How do the measured dynamic soaring trajectories compare to the numerical trajectory optimization results?

- How many g's do albatross experience during dynamic soaring maneuvers, how does this vary between species, and how does it compare to theoretical calculations based on their bone structure?
- How often do the albatross flap, if at all?
- How does the net speed of the birds vary with flight direction with respect to the wind?
- How does the net speed of the birds vary with respect to the direction of wave travel?
- What is the airspeed variation throughout the dynamic soaring trajectories of different albatross species?
- What do typical ocean boundary layer profiles look like?

The first question should be answered solely by the positions output by the GPS and the EKF. The second question should also be straightforward to answer by examining the magnitude of the accelerations throughout the dynamic soaring maneuvers. Flapping may also be detectable by the accelerometers as the body of the bird moves up and down opposite the movement of the wings.

The next two questions can be answered by comparing the net speed of the birds over cycles flown in different directions and correlating them to the wind and wave measurements available from NOAA's Wave Watch III models, and to wind speed estimates from the trackers.

Answering the final two questions depends on the quality of the airspeed measurements provided by the tracker, which are the most suspect of the measurements available. With sufficient airspeed measurement accuracy it should be possible to derive estimates of the local winds and potentially the shape of the boundary layer.

6.2 EKF

For post-processing the albatross tracker data and for real-time state estimation on-board *Mariner* an EKF was implemented. The EKF fuses the GPS, IMU, and pressure measurements to estimate the position and orientation of the UAV or bird. The standard EKF equations presented in Ref. [80] were used (Algorithm 6.1). The inputs are the mean and covariance of the state estimate at the previous time step, μ_{t-1} and Σ_{t-1} , the control inputs over the time interval, u_t , and the measurements observed at the current time, z_t . Other quantities and functions that are required include the possibly non-linear process model g and its Jacobian G , the possibly non-linear measurement model h and its Jacobian H , the process noise covariance matrix R and the measurement noise covariance matrix Q . The outputs of the algorithm are the mean and covariance estimates of the state at the current time, μ_t and Σ_t .

Algorithm 6.1 Extended Kalman Filter (μ_{t-1} , Σ_{t-1} , u_t , z_t)

- 1: $\bar{\mu}_t = g(\mu_{t-1}, u_t)$
 - 2: $\bar{\Sigma}_t = G_t \Sigma_{t-1} G_t^T + R_t$
 - 3: $K_t = \bar{\Sigma}_t H_t^T (H_t \bar{\Sigma}_t H_t^T - Q_t)^{-1}$
 - 4: $\mu_t = \bar{\mu}_t + K_t(z_t - h(\bar{\mu}_t))$
 - 5: $\Sigma_t = (I - K_t H_t) \bar{\Sigma}_t$
 - 6: **return** μ_t , Σ_t
-

An unscented Kalman filter (UKF) was also considered. The UKF has been shown to have a higher order of accuracy than an EKF [81]. One of the touted benefits of the UKF is the lack of a need to evaluate the process and measurement model Jacobians. However, with the process and measurement models used in this work, it is much more computationally efficient to evaluate analytic expressions for the Jacobians than to evaluate the process model at all of the sigma points, which is essentially equivalent to central differencing to numerically approximate the Jacobians.

The process and measurement models used in this work are based on those presented by Van Der Mewre in Refs. [82, 83]. Since the sensor suites on the UAV and the albatross tracker are similar, the same models may be used for both, only the update rates and some of the covariances differ. The measurement model for the

UAV will also include additional height above ground measurements from either an ultrasonic rangefinder or a laser rangefinder.

The primary vehicle states to be estimated include the North, East, and Down positions, the North, East, and Down inertial velocities and the orientation of the vehicle, in this case described with four attitude quaternions. In addition, the filter is setup to estimate and track a number of slowly varying parameters that are unknown, but are important to the process and measurement models. After testing many variations of the filter on flight test data, the following additional parameter states were selected: the North and East wind velocities (defined positive when blowing to the North and East, respectively), the three rate gyro biases, the three accelerometer biases, and a barometric pressure bias. The state vector, μ , has a total of 19 states. The process model and measurement models are described in the following subsections.

6.2.1 Process Model

The process model estimates the future state of the system, given the previous state and control inputs. In this work we use a kinematic process model that treats the vehicle as a point mass with an orientation. The accelerometer and gyro measurements are treated as the control inputs, u , and drive the system dynamics. The equations presented here assume that the accelerometer and gyro are mounted at the aircraft or bird center of gravity. Without measurement updates the kinematic process model performs dead reckoning by integrating the accelerations and angular rates to update the position and orientation of the vehicle. In the discrete model used here, the accelerations and angular rates are assumed to be constant over each time step. All of the states are assumed to have uncorrelated zero mean additive Gaussian process noise. The process noise terms are not shown in the equations that follow for clarity. The final covariance values used in the development UAV will be given in the testing section.

A dynamic process model of the complete UAV or bird that models the aerodynamic forces and moments is also possible, but was quickly discarded in this work due to its comparative computational complexity, and in the case of the albatross tracker

a lack of knowledge of the bird's control inputs. Computationally, the kinematic process model is simple enough to run at 100 Hz onboard the development UAV while using less than 10% of the system instruction cycles, leaving plenty of resources for the controllers. Computational speed is less important for the albatross tracker as the sensor measurements are post-processed on the ground after retrieval.

The kinematic process model equations are discretized and integrated using forward Euler. The position and velocity update equations are shown in Eqs. 6.2 and 6.3.

$$\begin{bmatrix} N_{t+1} \\ E_{t+1} \\ D_{t+1} \end{bmatrix} = \begin{bmatrix} N_t \\ E_t \\ D_t \end{bmatrix} + \begin{bmatrix} V_{N_t} \\ V_{E_t} \\ V_{D_t} \end{bmatrix} dt \quad (6.2)$$

$$\begin{bmatrix} V_{N_{t+1}} \\ V_{E_{t+1}} \\ V_{D_{t+1}} \end{bmatrix} = \begin{bmatrix} V_{N_t} \\ V_{E_t} \\ V_{D_t} \end{bmatrix} - R_b^i \left(\begin{bmatrix} a_{x_{meas}} \\ a_{y_{meas}} \\ a_{z_{meas}} \end{bmatrix} - \begin{bmatrix} a_{x_{bias}} \\ a_{y_{bias}} \\ a_{z_{bias}} \end{bmatrix} \right) dt + \begin{bmatrix} 0 \\ 0 \\ g \end{bmatrix} dt \quad (6.3)$$

where R_b^i is the body frame to inertial frame rotation matrix given in terms of the four attitude quaternions in Eq. 6.4.

$$R_b^i = \begin{bmatrix} 1 - 2q_{2t}^2 - 2q_{3t}^2 & 2q_{1t}q_{2t} - 2q_{0t}q_{3t} & 2q_{1t}q_{3t} + 2q_{0t}q_{2t} \\ 2q_{1t}q_{2t} + 2q_{0t}q_{3t} & 1 - 2q_{1t}^2 - 2q_{3t}^2 & 2q_{2t}q_{3t} - 2q_{0t}q_{1t} \\ 2q_{1t}q_{3t} - 2q_{0t}q_{2t} & 2q_{2t}q_{3t} + 2q_{0t}q_{1t} & 1 - 2q_{1t}^2 - 2q_{2t}^2 \end{bmatrix} \quad (6.4)$$

The quaternion update is performed using Eq. 6.5.

$$\begin{bmatrix} \Delta\phi \\ \Delta\theta \\ \Delta\psi \end{bmatrix} = \left(\begin{bmatrix} \omega_x \\ \omega_y \\ \omega_z \end{bmatrix} - \begin{bmatrix} \omega_{x_{bias}} \\ \omega_{y_{bias}} \\ \omega_{z_{bias}} \end{bmatrix} \right) dt \quad (6.5a)$$

$$s = 0.5\sqrt{\Delta\phi^2 + \Delta\theta^2 + \Delta\psi^2} \quad (6.5b)$$

$$\begin{bmatrix} q_{0_{t+1}} \\ q_{1_{t+1}} \\ q_{2_{t+1}} \\ q_{3_{t+1}} \end{bmatrix} = \cos(s) \begin{bmatrix} q_{0_t} \\ q_{1_t} \\ q_{2_t} \\ q_{3_t} \end{bmatrix} + \frac{\sin s}{2s} \begin{bmatrix} \Delta\phi q_{1_t} + \Delta\theta q_{2_t} + \Delta\psi q_{3_t} \\ \Delta\phi q_{0_t} - \Delta\psi q_{2_t} + \Delta\theta q_{3_t} \\ -\Delta\theta q_{0_t} + \Delta\psi q_{1_t} - \Delta\phi q_{3_t} \\ -\Delta\psi q_{1_t} - \Delta\theta q_{1_t} + \Delta\phi q_{2_t} \end{bmatrix} \quad (6.5c)$$

By definition the attitude quaternion is supposed to be unit norm, however, due to discretization and numerical errors the quaternion magnitude may drift as the filter progresses. A number of techniques are discussed in the literature to perform this renormalization [83, 84, 85, 86, 87]. In this work, the barycentric mean is taken to renormalize the quaternion after every process update and every measurement update, as given in Eq. 6.6 where $\mathbf{q} = [q_0 \ q_1 \ q_2 \ q_3]^T$.

$$\mathbf{q}_{t+1} = \frac{\mathbf{q}_{t+1}}{\|\mathbf{q}_{t+1}\|} \quad (6.6)$$

The update equations for the 9 additional parameters are trivial, as they are assumed to vary slowly via random walk (Eq. 6.7).

$$\begin{bmatrix} W_{Nt+1} \\ W_{E_{t+1}} \\ \omega_{x_{bias_{t+1}}} \\ \omega_{y_{bias_{t+1}}} \\ \omega_{z_{bias_{t+1}}} \\ a_{x_{bias_{t+1}}} \\ a_{y_{bias_{t+1}}} \\ a_{z_{bias_{t+1}}} \\ p_{baro_{bias_{t+1}}} \end{bmatrix} = \begin{bmatrix} W_{Nt} \\ W_{E_t} \\ \omega_{x_{bias_t}} \\ \omega_{y_{bias_t}} \\ \omega_{z_{bias_t}} \\ a_{x_{bias_t}} \\ a_{y_{bias_t}} \\ a_{z_{bias_t}} \\ p_{baro_{bias_t}} \end{bmatrix} \quad (6.7)$$

The process model Jacobian, G , at each time is also required by the EKF algorithm. The resulting Jacobian matrix for the kinematic process model presented here is mostly sparse. The analytic derivatives are not shown in the interest of space, but they are simple to derive, with the exception of the quaternion derivatives, which are more complicated due to the renormalization. In fact, it is computationally faster to perform the finite differencing steps for the quaternion states than to evaluate the analytic expressions.

6.2.2 Measurement Model

All of the sensors onboard the trackers or UAV, with the exception of the accelerometers and rate gyros, are used to correct the process model predictions during the measurement update. The measurement model takes the state estimate as an input and predicts what the corresponding measurements would be, then compares the predicted measurements to the actual measurements. In practice, the measurement updates may be applied asynchronously as they become available, or applied in parallel if they arrive at a similar times.

In our implementation onboard the development UAV, the GPS measurements arrive at 4 Hz, while the magnetometer and pressure measurements update at 100 Hz. We therefore have two separate measurement updates that are used depending on the GPS measurement availability. One involves all of the sensors and runs at 4

Hz, and the other only involves the magnetometer and pressure sensors and runs at 100 Hz. Additional aircraft pseudo-measurements are applied only during the GPS measurement updates.

In the current post-processing algorithm for the albatross tracker, different measurement updates are used asynchronously for each sensor, corresponding to the magnetometer (50 Hz), the GPS (10 Hz), and each pressure sensor (10Hz). Details of the measurement model equations for each of the sensors are detailed below. The Jacobian of each of these measurements is required by the EKF algorithm as well, but again the derivations are straight forward and left to the reader. Again, it should be noted that after the measurement model update the quaternions are renormalized.

GPS Measurement Model

The GPS measurement model is very straight forward. The predicted position and velocity measurements correspond to the inertial position and velocity states (Eq. 6.8). Many GPS modules have a latency associated with their internal processing before outputting the position fix to the host. There are a number of techniques to account for these latencies, however, none of them have been implemented [88, 83].

$$h_{GPS}(\bar{\mu}) = \begin{bmatrix} N & E & D & V_N & V_E & V_D \end{bmatrix}^T \quad (6.8)$$

It should be noted that the GPS coordinates for a given flight are converted to a local North-East-Down coordinate frame using a local flat Earth assumption. This is a valid assumption for short range flights conducted by the *Mariner* development UAV. For the Albatross tracker, the high resolution data segments will only be on the order of 5 minutes long, so the assumption is also reasonable for the duration of each data segment. For long range flights the position coordinates could be modified to latitude and longitude, with increased process model complexity.

Magnetometer Measurement Model

The magnetometer measurement model predicts the fraction of the total magnetic field strength in the each of the body axes as given by Eq. 6.9, where $R_i^b = R_b^{iT}$ and

the MAG_i are the three components of the normalized true magnetic field strength in the NED coordinate frame. The true magnetic field strength is computed using the World Magnetic Model based on the latitude, longitude, altitude, and date [89]. Similar to the flat Earth assumption, it is valid to assume the direction of the Earth's magnetic field lines are constant over short distances. Since only the direction of the field lines matter for determining orientation, the true field value and the onboard measurements are normalized to unit vectors.

$$h_{mag}(\bar{\mu}) = R_i^b \begin{bmatrix} MAG_N \\ MAG_E \\ MAG_D \end{bmatrix} \quad (6.9)$$

Barometric Pressure Measurement Model

The barometric pressure measurement model uses the 1976 U.S. Standard Atmosphere to predict the barometric pressure at a given altitude. For a down position in units of meters and pressure in units of Pascals the predicted pressure is given by Eq. 6.10. The barometric pressure bias state acts to correct the barometric altitude to match the GPS altitude over long time scales.

$$h_{baro}(\bar{\mu}) = 101325 \left(1 + 2.2572 \times 10^{-5} D\right)^{5.256} - p_{barobias} \quad (6.10)$$

Differential Pressure Measurement Model

The differential pressure measurement model predicts the pressure difference between the pitot and static ports, which is proportional to the square of the airspeed. The airspeed is calculated as a function of the inertial velocities and the wind estimates to give the final measurement model equation (Eq. 6.11).

$$h_{diff}(\bar{\mu}) = \frac{\rho}{2} ((V_N - W_N)^2 + (V_E - W_E)^2 + V_D^2) \quad (6.11)$$

Aircraft Pseudo Measurement Model

The kinematic process model used in this work estimates the position and orientation of the inertial measurement unit, however, it has no knowledge that it is located in an airplane or on a bird. The process model will not complain if the airplane is flying sideways or backwards. By including some knowledge of the vehicle dynamics it should be possible to improve the state estimates. For an airplane, a reasonable assumption is that the airspeed vector is pointed primarily in the direction of the body x-axis, in other words the angle of attack and sideslip angles are small [90]. The aircraft pseudo measurement assumes that there is no component of airspeed along the body y-axis (sideslip = 0), there is a small component in the body z-axis due to the aircraft flying at a small angle of attack, and the largest component is aligned with the body x-axis. The pseudo measurement equations in terms of the state variables are given in Eq. 6.12, where the measurements should be zero if the aircraft is flying at zero side slip and an angle of attack, α .

$$h_{pseudo}(\bar{\mu}) = R_i^b \begin{bmatrix} V_N - W_N \\ V_E - W_E \\ V_D \end{bmatrix} - \sqrt{(V_N - W_N)^2 + (V_E - W_E)^2 + V_D^2} \begin{bmatrix} \cos \alpha \\ 0 \\ \sin \alpha \end{bmatrix} \quad (6.12)$$

6.3 Flight Test Results

The EKF was validated on the *Mariner* hardware and software development airframe shown in Fig. 6.11. The EKF algorithm described above was implemented in C and run in realtime on the Gumstix flight computer. The accelerometers, rate gyros, magnetometer, and pressure sensors update at 100 Hz. A uBlox LEA-5H GPS module was configured to update at its maximum rate of 4 Hz. The EKF was run at 100 Hz, providing state estimates for the inner loop control laws which were run at 50 Hz. At 100 Hz, the EKF requires less than 9% of the total CPU instruction cycles. This leaves plenty of computational resources to run the low and mid-level controllers discussed in Chapter 4.



Figure 6.11: Picture of the hardware and software development UAV (Multiplex Easy Glider Pro) for the *Mariner* flight control system.

6.3.1 EKF Validation

Obtaining truth data for validating the EKF position and orientation estimates is difficult to achieve when flying outdoors. Motion capture systems enable very accurate estimates indoors, but this is not an option for vehicles of this size. Other methods were used to give independent measurements of some of the states for comparison to the EKF.

The bank and pitch angle estimates were compared to horizon measurements from an onboard camera. The wind speed and direction estimates were qualitatively compared to ground observations and inferred by plotting the inertial GPS velocity as a function of heading angle when flying circular paths at nearly constant altitude and airspeed. The amplitude of the resulting sinusoid corresponds to the wind speed, the mean value corresponds to the airspeed, and the peak location indicates the wind direction.

For the flight tests the filter initial conditions were set to the values shown in Eq. 6.13, where the units are meters, seconds, and radians where appropriate. The state

variables are in the following order: N , E , D , V_N , V_E , V_D , q_0 , q_1 , q_2 , q_3 , W_N , W_E , $\omega_{x_{bias}}$, $\omega_{y_{bias}}$, $\omega_{z_{bias}}$, $a_{x_{bias}}$, $a_{y_{bias}}$, $a_{z_{bias}}$, and $p_{barobias}$.

$$\mu_0 = \begin{bmatrix} 0 & 0 & z_{D_0} & z_{V_{N_0}} & z_{V_{E_0}} & 0 & \cos \frac{\psi_0}{2} & 0 & 0 & \sin \frac{\psi_0}{2} & 0 & 0 \end{bmatrix} \quad (6.13a)$$

$$\omega_{x_0} \quad \omega_{y_0} \quad \omega_{z_0} \quad 0 \quad 0 \quad 0 \quad (101325(1 + 2.2572 \times 10^{-5}z_{D_0})^{5.256} - z_{baro}) \quad]$$

$$\Sigma_0 = diag \left(\begin{bmatrix} 100 & 100 & 100 & 10 & 10 & 10 & 0.01 & 0.01 & 0.01 & 0.01 & 4 & 4 \\ 0.0001 & 0.0001 & 0.0001 & 0.001 & 0.001 & 0.001 & 400 \end{bmatrix} \right) \quad (6.13b)$$

where $\psi_0 = \arctan(z_{mag_{y_0}}/z_{mag_{x_0}}) - \arctan(MAG_E/MAG_N)$. After tuning parameters over many flights, the final process and measurement noise values were set as shown in Eqs. 6.14 and 6.15. For the aircraft pseudo measurements the angle of attack is assumed to be 5° . The measurement noise is assumed to capture any deviations from this angle of attack and zero sideslip.

$$R = diag \left(\begin{bmatrix} 0.1 & 0.1 & 0.1 & 0.1 & 0.1 & 0.1 & 10^{-8} & 10^{-8} & 10^{-8} & 10^{-8} & 10^{-5} \\ 10^{-5} & 10^{-8} & 10^{-8} & 10^{-8} & 10^{-8} & 10^{-6} & 10^{-6} & 10^{-6} & 10^{-6} & 50 \end{bmatrix} \right) \quad (6.14a)$$

$$Q_{GPS} = diag \left(\begin{bmatrix} 25 & 25 & 36 & 0.5 & 0.5 & 1 \end{bmatrix} \right) \quad (6.15a)$$

$$Q_{mag} = diag \left(\begin{bmatrix} 1 & 1 & 1 \end{bmatrix} \right) \quad (6.15b)$$

$$Q_{baro} = 50 \quad (6.15c)$$

$$Q_{diff} = 4 \quad (6.15d)$$

$$Q_{pseudo} = diag \left(\begin{bmatrix} 0.3 & 0.3 & 0.3 \end{bmatrix} \right) \quad (6.15e)$$

As an example of filter verification, video from a few flights were recorded onboard the aircraft by an inexpensive digital video recorder than has a resolution of 640 x 480 and a 72° field of view. After the flight, stills were extracted from the video at 4 Hz and a horizon detection algorithm was run to generate independent pitch and

roll measurements to compare with the filter outputs. The following algorithm was implemented in Matlab to identify the horizon in the images (Alg. 6.2).

Algorithm 6.2 Horizon Detection

- 1: Convert image to grayscale
 - 2: Smooth image with Gaussian filter
 - 3: Identify edge pixels with Sobel edge detection algorithm
 - 4: Compute Hough transform on edge pixels
 - 5: Plot the lines corresponding to the 5 largest peaks on the original image
 - 6: Manually identify the line that corresponds to the horizon
 - 7: **return** ϕ, θ
-

In the flight test area there were a number of prominent lines due to roads and buildings that were often identified as significant. Nonetheless, the algorithm worked quite well, typically identifying the horizon as the most significant line in the image, and never lower than the 5th most prominent line. Manual identification of which significant line was the horizon was used on the set of flight test data rather than spending significant time refining the horizon detection algorithm. A sample frame from the flight test video is shown in Fig. 6.12 along with the various steps applied to it by the algorithm. The bank angle is calculated from the slope of the horizon line. The pitch angle is taken as the perpendicular distance from the line to the center of the image converted from units of pixels to an angle by the scaling it by the camera field of view.

Figure 6.13 shows a comparison of the bank angle and pitch angle estimates derived from video and by the EKF for a portion of a test flight. It is obvious that the filter tracks the orientation of the vehicle as estimated by the camera quite well, although there are occasionally brief deviations. The root mean squared (RMS) error between the EKF and the horizon estimates is about 1.7° for the pitch angle and 2.1° for the bank angle.

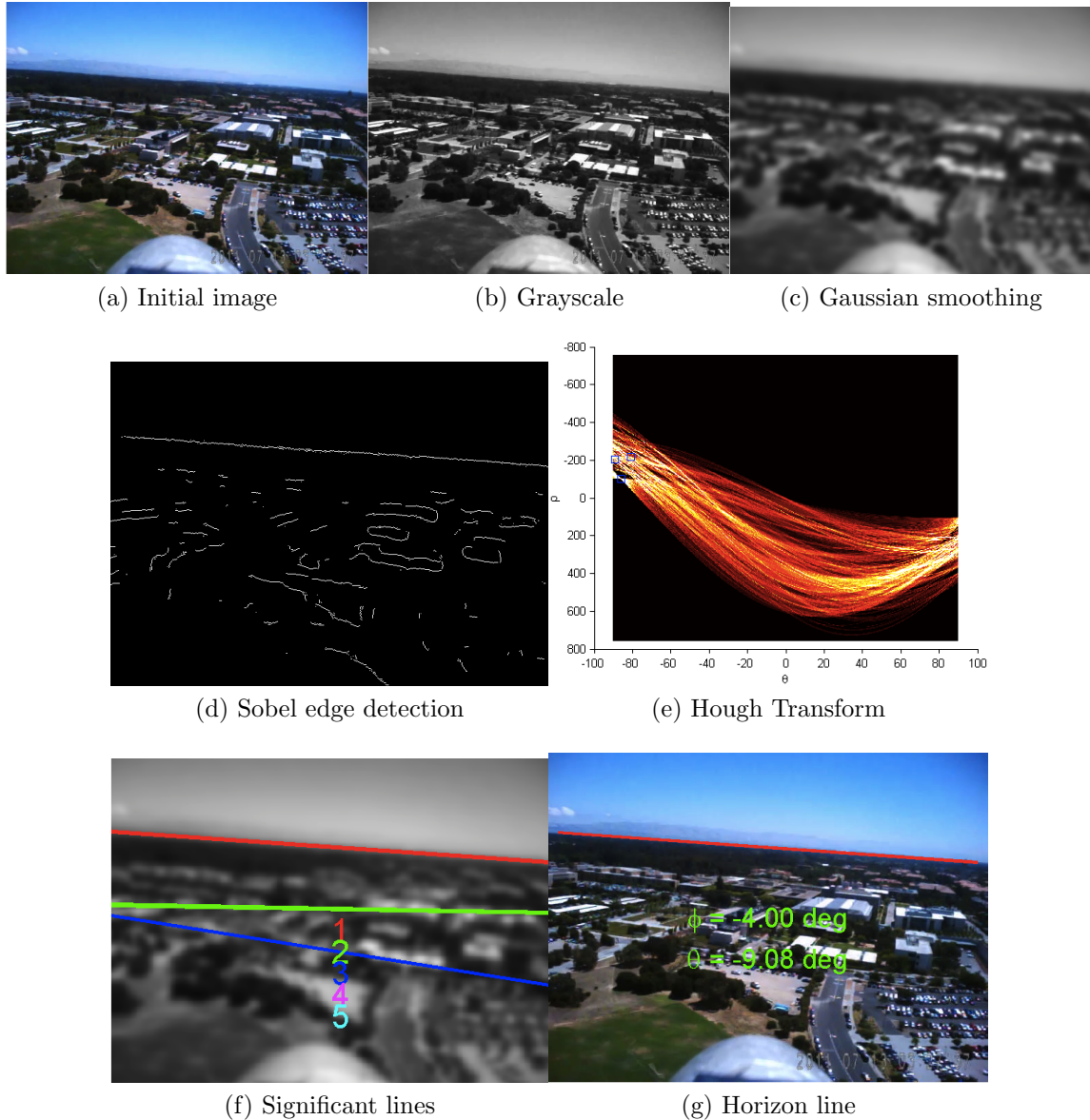


Figure 6.12: Images illustrating the steps in the horizon detection algorithm.

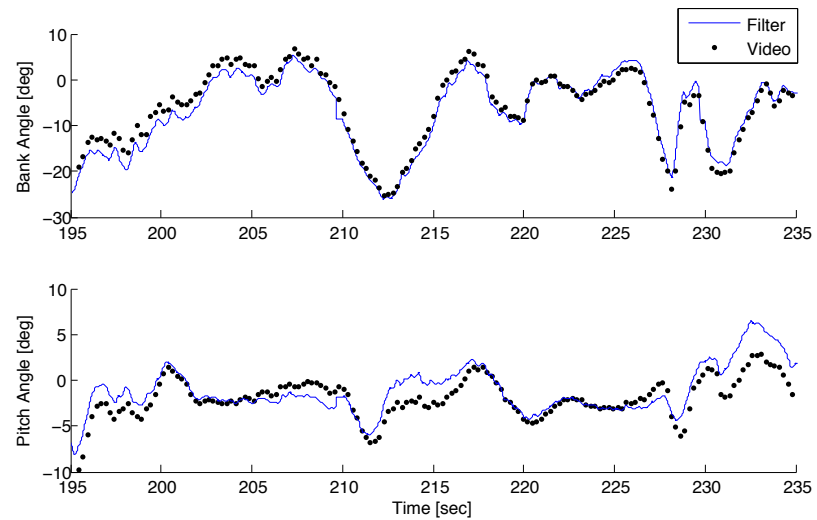


Figure 6.13: Comparison of bank angle and pitch angle estimates between the EKF and the horizon estimated from onboard video.

Chapter 7

Conclusions and Future Work

Past studies of dynamic soaring have focused on understanding the performance of albatrosses and other large seabirds that use dynamic soaring for propulsion through trajectory optimization. Recently, other researchers have begun to consider using dynamic soaring as a propulsive energy source for small UAVs. This work extends those studies in a number of directions, bringing the demonstration of a dynamic soaring UAV closer to reality.

7.1 Summary of Findings

In Chapter 2, the equations of motion are derived for a point mass model of a UAV flying through a spatially and temporally varying wind field. An additional equation of motion was added to represent changes in the energy state of the onboard battery due to the inclusion of an electric motor/generator, solar panels, and onboard processing and sensor systems. An energy analysis of the equations of motion is performed to illustrate how energy is added to the system by winds. Numerous numerical approaches to solving the trajectory optimization problem are detailed and compared. The collocation method was shown to return the best results in terms of computational speed and robustness.

In Chapter 3, the trajectory optimization routine is used to solve a number of

interesting problems. First, polar results are presented showing the minimum required wind speed to fly in different directions with respect to the winds for a model Wandering Albatross. Additionally, speed polars are generated showing the maximum net speed attainable at a given wind speed for net movement in each direction with respect to the wind. In general, the greatest speed is achievable at roughly 45° off of the wind direction. The resulting speed polars are similar in appearance to the performance polars of sailboats, highlighting the similarities between these two propulsion methods that take advantage of the winds. A simple wind-wave boundary layer model is presented along with optimal periodic trajectories for the model Wandering Albatross flying through it. The results at least partially explain observations of albatross flying near the surface on the lee side of waves.

Next, the impact of varying the battery energy charge/discharge rate was examined. It was shown that if solar power is available, it should be used to power the onboard electrical systems and to charge the batteries for later use when solar power is unavailable. The potential speed gains due to solar power are small, however by charging the battery it is possible to delay or offset the speed penalty incurred if a generator has to be used.

Chapter 4 describes the three-level control strategy proposed for a dynamic soaring UAV as it flies over the oceans. A summary is presented of the low- and mid-level controllers under development by a colleague. The majority of the chapter focuses on the development and implementation of a long range route planner for flights across the oceans. The method of isochrones is used in a receding horizon like control scheme to plan trajectories through wind fields predicted by NOAA's Wavewatch III product. The resulting control trajectory is used until new wind predictions are available, at which point the trajectory planning is repeated. An algorithm is presented to identify the outer boundary of a non-convex point cloud, while retaining boundary features down to a user specified length scale.

High-level controller results are presented for an example dynamic soaring mission from San Francisco to Hawaii for a number different planning horizons. With perfect knowledge of the winds the minimum time flight takes 60 hours for the given wind field. The controller is able to make the journey in 65 hours with a planning horizon

of 12 hours. The computational cost is shown to increase roughly quadratically with the length of the planning horizon.

Chapter 5 examines the role that the design of the aircraft plays in dynamic soaring performance. Trade studies are conducted on the various trajectory optimization inputs to gain insight into the most important design parameters. The lift-to-drag ratio is shown to be the dominant parameter in identifying the minimum required wind speed. A set of sensors and control electronics are specified for an aircraft designed to demonstrate autonomous dynamic soaring over the ocean. In addition to being able to accurately estimate the aircraft's orientation, the need for an accurate and reliable height above surface sensor highlighted. Ultrasonic rangefinders and laser rangefinders are the best candidates for these sensors.

The sizing of the *Mariner* demonstration UAV is carried out to minimize the required reference wind speed with conservative values for trajectory optimization constraints such as control bounds and height above the surface. The control surfaces on the resulting design are refined to ensure adequate dynamic mode damping and controllability throughout the dynamic soaring trajectory. The final *Mariner* design has a wingspan of 2.49 m, a mass of just under 2 kg, and a wing area of 0.485 m². The required reference wind speed is 8.01 m/s assuming the wingtip is constrained to be at least 0.5 m above the surface and that the maximum bank angle is constrained to 60°.

Chapter 6 details experimental steps taken throughout this work to increase the understanding of dynamic soaring in nature, and to move towards a dynamic soaring demonstration UAV. A lightweight albatross tracking tag was designed and built to record GPS and IMU data during dynamic soaring maneuvers. Six tags are set to deploy in early 2012 to gain valuable data on the dynamic soaring trajectories of different albatross species.

A small off-the-shelf model airplane was outfitted with *Mariner*'s proposed flight control hardware and used as a software development testbed. Details of an extended Kalman filter that fuses GPS, IMU, and pressure measurements to estimate the aircraft's state are provided. Flight tests were performed to tune the filter covariance matrices and to verify the filter measurements against independent measurement

sources. A simple horizon detection algorithm was detailed to estimate the pitch and roll angles. The algorithm was applied to frames pulled from onboard video for comparison to the EKF estimates. The RMS error between the filter and horizon measurements was on the order of 2° for both pitch and roll.

7.2 Suggestions for Future Work

There are many avenues to follow to extend the work presented in this thesis. Ultimately the goal would be to design an autonomous dynamic soaring UAV that is capable of circumnavigating the world. Such a vehicle could also be used to deliver science data on the interaction between the ocean and atmosphere, or to monitor shipping lanes and commercial fisheries. In the shorter term, some of the tasks that present interesting research opportunities include the following:

- Implement a higher-fidelity six-degree of freedom trajectory optimization routine for comparison to the point mass model used in this work. It would also be interesting to model the wind speed variation across the span and the effect it has on the aircraft forces and moments. This may be important when flying in stronger gradients or with bigger vehicles, but likely has a small effect on the *Mariner*.
- Generate full aircraft performance polars as a function of reference wind speed, flight direction with respect to the wind, and the battery energy charge/discharge rate. These polars could be used in an expanded high-level routing algorithm to control the aircraft heading and manage the battery energy to reach the destination as quickly as possible.
- Look at additional example missions with the high-level controller and develop a reasonable heuristic to guide selection of the planning horizon.
- Improve the performance of the high-level controller by accounting for uncertainty in the wind predictions. The goal would be to incorporate the knowledge that wind predictions are increasingly uncertain farther into the future.

- Extend the high-level controller to include control decisions on the battery energy charge rate in addition to the heading. The isochrones will have an additional dimension of the battery charge state.
- Verify the wind-wave boundary layer model with additional experimental data, especially close to the surface. Expand the model to handle cases where the wind and waves are not aligned.
- Analyze the data returned by the albatross trackers to answer many of the questions posed in Section 6.1.3.
- Construct the *Mariner* design and work towards demonstrating autonomous dynamic soaring over the ocean. This includes testing the height above ground sensors when flying near the ocean surface. There are questions as to the maximum range, repeatability, and robustness of the ultrasonic rangefinders and the laser range finders when operating over water.

Appendix A

Trajectory Optimization Validation Results

The table of state and control values was generated using the collocation method described in chapter 2 with $N = 51$ collocation points and convergence tolerances of $1e - 8$. Vehicle parameters are given in Table 2.3 and a log boundary layer is used with $h_{ref} = 10$ m and $h_0 = 0.03$ m. Results are given to eight significant digits for the six state variables (x, y, z, V, γ, ψ) and the two control variables (C_L and ϕ).

Table A.1: State and control values for the trajectory optimization validation case. Note that $V_{ref} = 8.560115$ m/s and $t_{cycle} = 7.002516$ s.

t [s]	x [m]	y [m]	z [m]	V [m/s]	γ [rad]	ψ [rad]	C_L	ϕ [rad]
0.00000000	0.00000000	0.00000000	-1.50000000	20.81773602	0.00000000	1.79589895	1.44984890	-1.19795842
0.14005032	-1.18905294	2.87147420	-1.50293435	20.60955530	-0.00004506	1.60868708	1.47204934	-1.26254686
0.28010063	-1.83601705	5.73483777	-1.50000000	20.40536499	0.00015552	1.42128014	1.49052092	-1.19099412
0.42015095	-1.95987754	8.49056898	-1.50000000	20.20171166	-0.00366239	1.23274944	1.50000000	-1.29754734
0.56020127	-1.59741495	11.04744062	-1.50000000	20.00212116	0.01403398	1.05584504	1.50000000	-0.93809348
0.70025158	-0.85704812	13.35543337	-1.61586347	19.81128446	0.07280443	0.90310077	1.50000000	-0.77857997
0.84030190	0.14995613	15.38451597	-1.91663850	19.63801588	0.14725769	0.76360408	1.50000000	-0.67981242
0.98035222	1.32542372	17.11315275	-2.42854181	19.45420649	0.23032277	0.63563262	1.50000000	-0.59247373
1.12040254	2.57319691	18.54308931	-3.15358189	19.22461688	0.30920712	0.52927795	1.29475119	-0.49094379
1.26045285	3.80815625	19.72422656	-4.05037839	18.92484078	0.37318832	0.45208489	1.12762621	-0.37337167
1.40050317	4.97453528	20.71942204	-5.07236188	18.54126140	0.42549033	0.40016541	1.02840911	-0.246777841
1.54055349	6.03866241	21.58375478	-6.18362980	18.07547515	0.46985001	0.36933597	0.97641502	-0.11669363
1.68060380	6.97959653	22.36277921	-7.35644950	17.53491914	0.50862370	0.35691447	0.96460063	0.01336413
1.82065412	7.78310640	23.09376900	-8.56888145	16.92744861	0.54351563	0.36150885	0.98746317	0.14146317
1.96070444	8.43802771	23.80731836	-9.80294509	16.25976532	0.57555980	0.38285621	1.04256456	0.26659970
2.10075475	8.93399317	24.52858405	-11.04322587	15.53688071	0.60565707	0.42175479	1.13611215	0.38873368
2.24080507	9.26000322	25.27790826	-12.27571688	14.76294424	0.63334877	0.47951686	1.25287632	0.50766803
2.38085539	9.40349219	26.07096754	-13.48678843	13.93925534	0.66003892	0.56006896	1.47560504	0.62645246
2.52090571	9.35022107	26.91790140	-14.66216405	13.07521210	0.67781224	0.65969428	1.50000000	0.74242622
2.66095602	9.10684572	27.81767896	-15.77318595	12.19697537	0.67614699	0.76650769	1.50000000	0.84847058
2.80100634	8.69002866	28.76357486	-16.79169352	11.32846314	0.65331880	0.87407621	1.50000000	0.94302733
2.94105666	8.11839679	29.74735648	-17.69542833	10.49445029	0.60863816	0.97784513	1.50000000	1.02467093
3.08110697	7.41043058	30.76101791	-18.46753428	9.72187868	0.54154501	1.07488751	1.50000000	1.09296524
3.22115729	6.58320010	31.79765619	-19.09556000	9.04052194	0.45177949	1.16409110	1.50000000	1.14860451
3.36120761	5.651138306	32.85181383	-19.57051944	8.48279003	0.33995555	1.24597820	1.50000000	1.19327158
3.50125792	4.62652935	33.91944322	-19.88609383	8.08163799	0.20853463	1.32233952	1.50000000	1.22895882
3.64130824	3.51653896	34.99761492	-20.03802409	7.86580739	0.06278595	1.39584073	1.50000000	1.25695352
3.78135856	2.32532586	36.08406091	-20.02372254	7.85318647	-0.08913465	1.46968006	1.50000000	1.27683486
3.92140888	1.05265133	37.17662214	-19.84212220	8.04543166	-0.23761296	1.54730018	1.50000000	1.28613328
4.06145919	-0.30587629	38.27266015	-19.49377378	8.42742598	-0.37389294	1.63211010	1.50000000	1.28100879
4.20150951	-1.75862543	39.36849253	-18.98118710	8.97198182	-0.49173620	1.72714212	1.50000000	1.25748653
4.34155983	-3.31756800	40.45891535	-18.30939901	9.64657803	-0.58755804	1.83455665	1.50000000	1.21252337
4.48161014	-4.99767992	41.53688775	-17.48674176	10.41867284	-0.65972821	1.95494792	1.50000000	1.14469032
4.62166046	-6.81608160	42.59347900	-16.52577869	11.25834816	-0.70740352	2.08656158	1.50000000	1.05462810
4.76171078	-8.79088506	43.61822095	-15.4443596	12.13881758	-0.73034903	2.22479755	1.50000000	0.94499900
4.90176109	-10.93971676	44.60006728	-14.26672681	13.03575583	-0.72880461	2.36251365	1.50000000	0.81991587
5.04181141	-13.27740062	45.52938110	-13.02415174	13.92715583	-0.70440351	2.49037382	1.477119293	0.68262226
5.18186173	-15.80714618	46.40306433	-11.74876748	14.80430770	-0.66926018	2.59252600	1.21657898	0.54209913
5.32191205	-18.50815348	47.23185164	-10.45527153	15.66838117	-0.63294571	2.66492247	1.07874109	0.39908426
5.46196236	-21.36170960	48.03358140	-9.15777670	16.51355451	-0.59410966	2.71344119	0.96958964	0.24702986
5.60201268	-24.35091344	48.83235536	-7.87133390	17.33754939	-0.55298617	2.74035526	0.90951466	0.08580299
5.74206300	-27.45931018	49.65909061	-6.61378630	18.13740037	-0.50818167	2.74707985	0.89461462	-0.08151359
5.88211331	-30.66861937	50.55279102	-5.40812544	18.90821259	-0.45772806	2.73356086	0.93033621	-0.24699219
6.02216363	-33.95472393	51.56268941	-4.28567755	19.63903085	-0.39855098	2.69820385	1.02776369	-0.39956161
6.16221395	-37.28058594	52.75032573	-3.29036683	20.30474127	-0.32702876	2.63783938	1.18760667	-0.53015255
6.30226426	-40.58399573	54.18856907	-2.48278398	20.84647873	-0.23770143	2.54686872	1.44585361	-0.63103609
6.44231458	-43.76738160	55.94017287	-1.92571741	21.19220547	-0.14563917	2.43324644	1.39906350	-0.71493184
6.58236490	-46.73112467	58.00114408	-1.61168310	21.31863397	-0.06799269	2.30762810	1.38251863	-0.80166245
6.72241522	-49.38157728	60.34266800	-1.50000000	21.23028958	-0.01188141	2.15982935	1.39404856	-0.99656666
6.86246553	-51.61275140	62.93229020	-1.50000000	21.02444176	0.00306372	1.98261546	1.42148012	-1.29673870
7.00251585	-53.33555933	65.71106617	-1.50000000	20.81773602	0.00000000	1.79589895	1.44984890	-1.19795842

Bibliography

- [1] R. Spaar and B. Bruderer. Soaring migration of steppe eagles *Aquila nipalensis* in southern Israel: flight behaviour under various wind and thermal conditions. *Journal of Avian Biology*, pages 289–301, 1996.
- [2] C.J. Pennycuick. Thermal soaring compared in three dissimilar tropical bird species, *Fregata magnificens*, *Pelecanus occidentalis* and *Coragyps atratus*. *Journal of Experimental Biology*, 102(1):307, 1983.
- [3] M.J. Allen. Autonomous soaring for improved endurance of a small uninhabited air vehicle. In *43rd AIAA Aerospace Sciences Meeting and Exhibit, Reno, NV*, AIAA 2005-1025, 2005.
- [4] M. Allen. Updraft model for development of autonomous soaring uninhabited air vehicles. In *44th AIAA Aerospace Sciences Meeting and Exhibit, Reno, NV*, AIAA 2006-1510, 2006.
- [5] M.J. Allen and V. Lin. Guidance and control of an autonomous soaring vehicle with flight test results. In *45 th AIAA Aerospace Sciences Meeting and Exhibit, Reno, NV*, AIAA 2007-867, 2007.
- [6] D.J. Edwards. Implementation Details and Flight Test Results of an Autonomous Soaring Controller. In *Proceedings of the AIAA Guidance, Navigation and Control Conference*, AIAA 2008-7244, 2008.
- [7] G. Bower and A. Naiman. Just Keep Flying: Machine Learning for UAV Thermal Soaring. *Stanford University - CS 229 Final Project*, 2006.

- [8] G. Bower, T. Flanzer, and A. Naiman. Dynamic Environment Mapping for Autonomous Thermal Soaring . In *Proceedings of the AIAA Guidance, Navigation, and Control Conference*, AIAA 2010-8031, 2010.
- [9] CJ Pennycuick. Soaring behavior and performance of some East African birds, observed from a motor-glider. *Ibis*, 114(2):178–218, 1972.
- [10] J.W. Langelaan. Tree-based trajectory planning to exploit atmospheric energy. In *American Control Conference, 2008*, pages 2328–2333. IEEE, 2008.
- [11] C.K. Patel. *Energy extraction from atmospheric turbulence to improve flight vehicle performance*. PhD thesis, Stanford University, 2007.
- [12] J.P. Croxall, J.R.D. Silk, R.A. Phillips, V. Afanasyev, and D.R. Briggs. Global circumnavigations: tracking year-round ranges of nonbreeding albatrosses. *Science*, 307(5707):249, 2005.
- [13] G. Sachs. Minimum shear wind strength required for dynamic soaring of albatrosses. *Ibis*, 147(1):1–10, 2004.
- [14] J. Parle. Preliminary dynamic soaring research using a radio control glider. In *AIAA Aerospace Sciences Meeting*, AIAA 2004-132, 2004.
- [15] A. Ellison. Tyldesley model flying club - dynamic soaring website, <http://www.tmfcc.org.uk/ds/darkside.html>, Aug 2011.
- [16] K.E. Hanley and S.E. Belcher. Wave-driven wind jets in the marine atmospheric boundary layer. *Journal of the Atmospheric Sciences*, 65(8):2646–2660, 2008.
- [17] M. Latif and T.P. Barnett. Decadal climate variability over the North Pacific and North America: Dynamics and predictability. *Journal of Climate*, 9(10):2407–2423, 1996.
- [18] M.B.E. Boslough. Autonomous dynamic soaring platform for distributed mobile sensor arrays. *SAND 2002-1896, Sandia National Laboratories*, 2002.

- [19] T. Flanzer. *Robust Control of a Dynamic Soaring UAV (work in progress)*. PhD thesis, Stanford University, 2012.
- [20] M.R. Jackson, Y.J. Zhao, and R.A. Slattery. Sensitivity of trajectory prediction in air traffic management. *Journal of guidance, control, and dynamics*, 22(2):219–228, 1999.
- [21] Y.J. Zhao and Y.C. Qi. Minimum fuel powered dynamic soaring of unmanned aerial vehicles utilizing wind gradients. *Optimal control applications and methods*, 25(5):211–233, 2004.
- [22] Y.J. Zhao. Optimal patterns of glider dynamic soaring. *Optimal control applications and methods*, 25(2):67–89, 2004.
- [23] J.A. Duffie and W.A. Beckman. *Solar engineering of thermal processes*. New York, 1991.
- [24] R.B. Stull. *An introduction to boundary layer meteorology*. Springer, 1988.
- [25] J.W. Miles. On the generation of surface waves by shear flows. *Journal of Fluid Mechanics*, 3(02):185–204, 1957.
- [26] D.J.T. Carter. Prediction of wave height and period for a constant wind velocity using the JONSWAP results. *Ocean Engineering*, 9(1):17–33, 1982.
- [27] S.D. Smith. Coefficients for sea surface wind stress, heat flux, and wind profiles as a function of wind speed and temperature. *Journal of Geophysical Research*, 93(C12):15467–15, 1988.
- [28] S.E. Belcher and J.C.R. Hunt. Turbulent shear flow over slowly moving waves. *Journal of Fluid Mechanics*, 251(1):109–148, 1993.
- [29] S.D. Miller, C. Friehe, T. Hristov, and J. Edson. Wind and turbulence profiles in the surface layer over the ocean. In *12th Symp. on Boundary Layers and Turbulence*, pages 308–309. American Meteorological Society, 1997.

- [30] S.D. Miller, C. Friehe, T. Hristov, and J. Edson. The Wave-induced wind field above deep ocean waves. In *The 13th Symposium on Boundary Layers and Turbulence*, page 5B.4. American Meteorological Society, 1999.
- [31] P.P. Sullivan, J.C. McWillimas, and C.H. Moeng. Simulation of turbulent flow over idealized water waves. *Journal of Fluid Mechanics*, 404:47–85, 2000.
- [32] T.S. Hristov, S.D. Miller, and C.A. Friehe. Dynamical coupling of wind and ocean waves through wave-induced air flow. *Nature*, 422(6927):55–58, 2003.
- [33] F.M. Naderi, M.H. Freilich, and D.G. Long. Spaceborne radar measurement of wind velocity over the ocean—an overview of the NSCAT scatterometer system. *Proceedings of the IEEE*, 79(6):850–866, 1991.
- [34] C.J. Pennycuick. Gust soaring as a basis for the flight of petrels and albatrosses (Procellariiformes). *Avian Science*, 2(1):1–12, 2002.
- [35] P. Lissaman. Fundamentals of Wind Energy Extraction by Flight Vehicles. Draft, June 2010.
- [36] C.J. Pennycuick. The flight of petrels and albatrosses (Procellariiformes), observed in South Georgia and its vicinity. *Philosophical Transactions of the Royal Society of London. Series B, Biological Sciences*, 300(1098):75–106, 1982.
- [37] J. Lawrence, R. Nicholas, and S. Sukkarieh. A guidance and control strategy for dynamic soaring with a gliding UAV. In *Proceedings of the 2009 IEEE international conference on Robotics and Automation*, pages 1649–1654. IEEE, 2009.
- [38] H. Yang and Y.J. Zhao. A practical strategy of autonomous dynamic soaring for unmanned aerial vehicles in loiter missions. In *Infotech@ Aerospace*, AIAA 2005-6958, 2005.
- [39] N. Akhtar, J. Whidborne, and A. Cooke. Real-time trajectory generation technique for dynamic soaring UAVs. In *International Conference on Control*, Manchester, UK, 2008.

- [40] F. Hendriks. *Dynamic soaring*. PhD thesis, University of California, 1973.
- [41] C.J. Wood. The flight of albatrosses (a computer simulation). *Ibis*, 115(2):244–256, 1973.
- [42] P. Lissaman. Wind energy extraction by birds and flight vehicles. In *43rd AIAA Aerospace Sciences Meeting and Exhibit*, AIAA 2005–241, 2005.
- [43] J. Wharington. *Autonomous control of soaring aircraft by reinforcement learning*. PhD thesis, Royal Melbourne Institute of Technology, 1998.
- [44] G. Sachs and O. da Costa. Optimization of Dynamic Soaring at Ridges. In *AIAA Atmospheric Flight Mechanics Conference and Exhibit*, AIAA 2003-5303, Austin, Texas, 2003.
- [45] G. Sachs and P. Bussotti. Application of optimal control theory to dynamic soaring of seabirds. *Variational Analysis and Applications*, pages 975–994, 2005.
- [46] A.L. Herman and B.A. Conway. Direct optimization using collocation based on high-order Gauss-Lobatto quadrature rules. *Journal of Guidance Control and Dynamics*, 19(3):592–599, 1996.
- [47] P.E. Gill, W. Murray, and M.A. Saunders. SNOPT: An SQP algorithm for large-scale constrained optimization. *SIAM Journal on Optimization*, 12(4):979–1006, 2002.
- [48] Q. Gong, F. Fahroo, and I.M. Ross. Spectral algorithm for pseudospectral methods in optimal control. *Journal of guidance, control, and dynamics*, 31(3):460–471, 2008.
- [49] A.V. Rao, D. Benson, G.T. Huntington, B. Origin, W.A.C. Francolin, C.L. Darby, and M. Patterson. *Users Manual for GPOPS Version 2.1: A MATLAB R Package for Dynamic Optimization Using the Gauss Pseudospectral Method*, 2009.

- [50] M. Deittert, A. Richards, C.A. Toomer, and A. Pipe. Engineless Unmanned Aerial Vehicle Propulsion by Dynamic Soaring. *Journal of guidance, control, and dynamics*, 32(5), 2009.
- [51] H.L. Tolman. The 2002 release of WAVEWATCH III. In *7th International Workshop on Wave Hindcasting and Forecasting*, pages 188–197, 2002.
- [52] M. Deittert, S. Richards, C.A. Toomer, and A. Pipe. Dynamic Soaring Flight in Turbulence. In *AIAA Guidance, Navigation, and Control Conference*, AIAA 2009-6012, 2009.
- [53] D. Xiu and J.S. Hesthaven. High-order collocation methods for differential equations with random inputs. *SIAM Journal on Scientific Computing*, 27(3):1118, 2006.
- [54] H. Hagiwara. Weather routing of (sail-assisted) motor vessels. *Delft University of Technology, Delft*, 1989.
- [55] F.D. Faulkner. Determining optimum ship routes. *Operations Research*, pages 799–807, 1962.
- [56] R. Motte, R.S. Burns, and S. Calvert. Overview of current methods used in weather routing. *Journal of Navigation*, 41:101–14, 1988.
- [57] M.B. Klompstra, G.J. Olsder, and P.K.G.M. Brunschot. The isopone method in optimal control. *Dynamics and Control*, 2(3):281–301, 1992.
- [58] T. Thornton. A review of weather routing of sailboats. *Journal of Navigation*, 46(01):113–129, 1993.
- [59] J. Zhang and L. Huang. Optimal ship weather routing using isochrone method on the basis of weather changes. In *International Conference on Transportation Engineering*. ASCE, 2007.
- [60] P.C. Harper. Colour vision in the Procellariiformes (Note). *Mauri Ora*, 7:151–155, 1979.

- [61] M. Drela. *XFOIL- An analysis and design system for low Reynolds number airfoils*, 1989. Low Reynolds Number Aerodynamics.
- [62] M. Drela and H. Youngren. *AVL (Athena Vortex Lattice)*, 2007. 2007-09-01, <http://web.mit.edu/drela/Public/web/avl>.
- [63] H. Weimerskirch, F. Bonadonna, F. Bailleul, G. Mabille, G. Dell’Omo, and H.P. Lipp. GPS tracking of foraging albatrosses. *Science*, 295(5558):1259, 2002.
- [64] A. Fukuda, K. Miwa, E. Hirano, M. Suzuki, H. Higuchi, E. Morishita, D.J. Anderson, S.M. Waugh, and R.A. Phillips. BGDL-II, a GPS data logger for birds. *Memoirs of the National Institute of Polar Research Special*, pages 234–245, 2004.
- [65] J.A. Awkerman, A. Fukuda, H. Higuchi, and D.J. Anderson. Foraging activity and submesoscale habitat use of waved albatrosses, *Phoebastria irrorata*, during chick-brooding period. *Marine Ecology Progress Series*, 291:289–300, 2005.
- [66] S. Waugh, D. Filippi, A. Fukuda, M. Suzuki, H. Higuchi, A. Setiawan, and L. Davis. Foraging of royal albatrosses, *Diomedea epomophora*, from the Otago Peninsula and its relationships to fisheries. *Canadian Journal of Fisheries and Aquatic Sciences*, 62(6):1410–1421, 2005.
- [67] H. Weimerskirch, D. Pinaud, F. Pawlowski, and C.A. Bost. Does prey capture induce area-restricted search? a fine-scale study using GPS in a marine predator, the wandering albatross. *American Naturalist*, pages 734–743, 2007.
- [68] P. Jouventin and H. Weimerskirch. Satellite tracking of wandering albatrosses. *Nature*, 1990.
- [69] P.A. Prince, A.G. Wood, T. Barton, and J.P. Croxall. Satellite tracking of wandering albatrosses (*Diomedea exulans*) in the South Atlantic. *Antarctic Science*, 4(01):31–36, 1992.

- [70] E.K. Mackley, R.A. Phillips, J.R.D. Silk, E.D. Wakefield, V. Afanasyev, J.W. Fox, and R.W. Furness. Free as a bird? Activity patterns of albatrosses during the nonbreeding period. *Marine Ecology Progress Series*, 406:291–303, 2010.
- [71] S.A. Shaffer, Y. Tremblay, J.A. Awkerman, R.W. Henry, S.L.H. Teo, D.J. Anderson, D.A. Croll, B.A. Block, and D.P. Costa. Comparison of light-and SST-based geolocation with satellite telemetry in free-ranging albatrosses. *Marine Biology*, 147(4):833–843, 2005.
- [72] R.P. Wilson, D. Gremillet, J. Syder, M.A.M. Kierspel, S. Garthe, H. Weimerskirch, C. Schafer-Neth, J.A. Scolaro, C. Bost, J. Plotz, and D. Nel. Remote-sensing systems and seabirds: their use, abuse and potential for measuring marine environmental variables. *Marine Ecology Progress Series*, 228:241–261, 2002.
- [73] R.A. Phillips, J.P. Croxall, J.R.D. Silk, and D.R. Briggs. Foraging ecology of albatrosses and petrels from South Georgia: two decades of insights from tracking technologies. *Aquatic Conservation: Marine and Freshwater Ecosystems*, 17(S1):S6–S21, 2007.
- [74] R.A. Phillips, J.R.D. Silk, J.P. Croxall, V. Afanasyev, and D.R. Briggs. Accuracy of geolocation estimates for flying seabirds. *Marine Ecology Progress Series*, 266:265–272, 2004.
- [75] A.E. Burger and S.A. Shaffer. Application of tracking and data-logging technology in research and conservation of seabirds. *The Auk*, pages 253–264, 2008.
- [76] G. Sachs, J. Traugott, and F. Holzapfel. In-Flight Measurement of Dynamic Soaring in Albatrosses. In *Proceedings of AIAA GNC Conference*, AIAA 2010-8035, 2010.
- [77] J.W. Langelaan, N. Alley, and J. Neidhoefer. Wind Field Estimation for Small Unmanned Aerial Vehicles. In *Proceedings of the AIAA Guidance, Navigation and Control Conference*, AIAA 2010-8177, 2010.

- [78] Z.F. Syed, P. Aggarwal, C. Goodall, X. Niu, and N. El-Sheimy. A new multi-position calibration method for MEMS inertial navigation systems. *Measurement Science and Technology*, 18:1897, 2007.
- [79] J.F. Vasconcelos, G. Elkaim, C. Silvestre, P. Oliveira, and B. Cardeira. Geometric approach to strapdown magnetometer calibration in sensor frame. *IEEE Transactions on Aerospace and Electronic Systems*, 47(2):1293–1306, 2011.
- [80] S. Thrun, W. Burgard, and D. Fox. *Probabilistic Robotics (Intelligent Robotics and Autonomous Agents)*. The MIT Press, 2005.
- [81] R. Van Der Merwe. *Sigma-point Kalman filters for probabilistic inference in dynamic state-space models*. PhD thesis, Oregon Health and Science University, 2004.
- [82] R. van der Merwe and E. Wan. Sigma-point kalman filters for integrated navigation. In *Proceedings of the 60th Annual Meeting of the Institute of Navigation (ION)*, pages 641–654, 2004.
- [83] R. Van Der Merwe, E.A. Wan, and S. Julier. Sigma-point Kalman filters for nonlinear estimation and sensor-fusion: Applications to integrated navigation. In *Proceedings of the AIAA Guidance, Navigation & Control Conference*, AIAA 2004-5120, 2004.
- [84] N.S. Kumar and T. Jann. Estimation of attitudes from a low-cost miniaturized inertial platform using Kalman Filter-based sensor fusion algorithm. *Sadhana*, 29(2):217–235, 2004.
- [85] W. Khoder, B. Fassinut-Mombot, and M. Benjelloun. Quaternion unscented Kalman filtering for integrated inertial navigation and GPS. In *Information Fusion, 2008 11th International Conference on*, pages 1–8. IEEE, 2008.
- [86] J.L. Crassidis. Sigma-point Kalman filtering for integrated GPS and inertial navigation. *IEEE Transactions on Aerospace and Electronic Systems*, 42(2):750–756, 2006.

- [87] Y.J. Cheon and J.H. Kim. Unscented filtering in a unit quaternion space for spacecraft attitude estimation. In *Industrial Electronics, 2007. ISIE 2007. IEEE International Symposium on*, pages 66–71. IEEE, 2005.
- [88] D. Jung and P. Tsiotras. Inertial attitude and position reference system development for a small UAV. *AIAA Infotech at aerospace*, 2007.
- [89] S. Maus, S. Macmillan, S. McLean, National Geophysical Data Center, and British Geological Survey. *The US/UK World Magnetic Model for 2010-2015*. NOAA National Geophysical Data Center, 2010.
- [90] T.H. Paulsen. *Low Cost/high Precision Flight Dynamics Estimation Using the Square-root Unscented Kalman Filter*. PhD thesis, Brigham Young University, 2010.